Simulation of Moving Trailing Edge Flaps on a Wind Turbine Blade using a Navier-Stokes based Immersed Boundary Method

Behrens, Tim; Shen, Wen Zhong; Zhu, Wei Jun; Sørensen, Jens Nørkær; Sørensen, Niels N.

Publication date:
2011

Citation (APA):
Behrens, T., Shen, W. Z., Zhu, W. J., Sørensen, J. N., & Sørensen, N. N. (2011). Simulation of Moving Trailing Edge Flaps on a Wind Turbine Blade using a Navier-Stokes based Immersed Boundary Method. DTU Mechanical Engineering.

Technical University of Denmark (DTU)
Department of Mechanical Engineering, Fluid Mechanics

Dissertation submitted to the Technical University of Denmark in partial fulfillment of
the requirements for the degree of Doctor of Philosophy in Mechanical Engineering

Simulation of Moving Trailing Edge Flaps on a Wind Turbine Blade using a Navier-Stokes based Immersed Boundary Method

Tim Behrens

Preface

This dissertation covers work I carried out between July 2008 and July 2011, while I was employed as an industrial PhD student at Vestas Wind Systems A/S. The studies have taken place at the Fluid Mechanics section of Technical University of Denmark (DTU) - Mechanical Engineering and Vestas' Global Research office at the Risø DTU campus.
Part of the funding was obtained by the Danish National Advanced Technology Foundation (Højteknologifonden) through the ATEF project (grant 028-2007-3). All calculations were performed using the Alfheim computational cluster operated at DTU. The cluster was financed by grant HDW-0107–02 from the Danish Center for Scientific Computing.

Acknowledgments

For their academic guidance, I want to thank my supervisors Associate Professor Wen Zhong Shen, Senior Researcher Wei Jun Zhu and Professor Jens N. Sørensen from the Fluid Mechanics section, as well as Professor Niels N. Sørensen from the Wind Energy Department at Risø DTU.
I thank all my great colleagues at Vestas - in particular every one at the Roskilde office - for making every day at work a brilliant experience. I would like to especially thank my boss Jens Jakob Wedel-Heinen for his support and his unbreakable good spirit. My thanks go to Niels Anker Olsen for always taking some time to help me out and for translating the abstract into Danish. My fellow PhD partner in crime Damien Castaignet is acknowledged for sharing the amount of good office Karma. Malene Ford was my appreciated advisor for all questions concerning the proper use of the English language.
I want to thank my family back in Germany and I apologize for not having been around enough in the last years.
Finally, I would have not been able to finish this dissertation without the loving support of my girlfriend Manuela Charlotte Will.

Thank you.

Tim Behrens

Abstract

As the rotor diameter of wind turbines increases, turbine blades with distributed aerodynamic control surfaces promise significant load reductions. Therefore, they are coming into focus in relation to research in academia and industry. Trailing edge flaps are of particular interest in terms of control surfaces. The unsteady flow around such flaps is usually investigated by applying linearized unsteady aerodynamic models or by solving the two dimensional unsteady Reynolds averaged Navier-Stokes equations. The latter method is usually applied in combination with moving or interpolated body conforming meshes. A more flexible method would open up an opportunity to investigate the flow features of complex moving flap geometries in great detail.

The immersed boundary method offers this flexibility, as the geometry is represented through the introduction of additional forcing terms in the governing equations. This approach allows for simulation of arbitrary geometries in fixed meshes that do not need to conform to the body geometry.

The flow solver EllipSys has previously been extended with a base implementation of an immersed boundary method. The present work developed the necessary tools to handle trailing edge flap geometries in two and three dimensions. Validation cases were presented for the circular cylinder in a Cartesian mesh topology as well as in a topology similar to a standard body fitted mesh. To simulate trailing edge flaps, a hybrid approach was developed that modeled only the moving flap as an immersed boundary, while the rest of the airfoil was represented by a conventional body-fitted mesh. The results from the hybrid approach were validated against published wind tunnel measurements and improvement over a thin-airfoil based flow model was proven.

A load alleviation control in a changing inflow was presented for a divided flap action, i.e. a segmented flap with independent actuation rates. It has been demonstrated that the total flap deflection can be divided into two separate deflections without deteriorating control authority. The results suggested that the combined use of two independent flap actuators was beneficial when dealing with complex inflows. Full scale turbine measurements were presented and indicated that the flap hinge moment provided suitable input for load control. A novel way of using the hinge moment of a moving flap for load alleviation control was presented. Simulations demonstrated the feasibility and robustness of the approach.

The hybrid immersed boundary approach proved to be able to handle 3D airfoil sections with span-wise flap gaps. The flow around and in the wake of a deflected flap at a Reynolds number of 1.63mio was investigated for steady inflow conditions. A control for two span-wise independent flaps was implemented and first load reductions could be achieved.

The hybrid method has demonstrated to be a versatile tool in the research of moving trailing edge flaps. The results shall serve as the basis for future investigations of the unsteady flow field around trailing edge flaps.

Synopsis (Danish)

Efterhånden som vindmøller fremstilles med større og større rotordiameter, giver distribuerede aerodynamiske kontrolflader lovende resultater i forbindelse med reducering af laster. Der bliver derfor fokuseret på sådanne flader i forskning både fra industriel og akademisk hold.

Af særlig interesse er bagkantsflapper. Den instationære strømning omkring sådanne flapper bliver typisk undersøgt ved hjælp af lineariserede instationære aerodynamiske modeller eller ved at løse de todimensionelle RANS (Reynolds Averaged Navier-Stokes) ligninger. Den sidstnævnte metode bliver typisk anvendt i forbindelse med bevægelige, eller interpolerede geometrikonforme beregningsnet. En mere fleksibel metode vil give mulighed for at undersøge strømningsforholdene omkring komplekse bevægelige flap geometrier i større omfang.

Omsvøbte randbetingelser giver denne fleksibilitet, da geometrien kan repræsenteres ved hjælp af ekstra kildeled i de styrende ligninger. Denne metode giver mulighed for at simulere arbitrære geometrier i stationære beregningsnet, der ikke nødvendigvis er tilpasset geometrien. En elementær implementering af omsvøbte randbetingelser er tidligere blevet indføjet i CFD løseren Ellipsys. I nærværende arbejde er de nødvendige værktøjer til håndtering af bagkantsflapper i to og tre dimensioner blevet frembragt i nævnte kode. Validering af metoden er foretaget på en cirkulær geometri i en kartesisk beregningsnettopologi, såvel som i en geometrikonform topologi.

En kombineret metode er blevet udviklet, hvori selve flappen modelleres ved hjælp af omsvøbte randbetingelser, hvorimod resten af vingeprofilet modelleres ved hjælp af geometrikonforme beregningsnet. Denne metode er valideret ved sammenligning med vindtunnelforsøg og en forbedring i forhold til en kordelline (Thin airfoil) vingeprofil metode er eftervist.

En metode til kontrol af laster i en varierende anstrømning bliver præsenteret for en leddelt flap med uafhængige aktueringsniveauer. Det bliver demonstreret at den totale flap udbøjning kan opdeles i to uafhængige regimer uden at evnen til at kontrollere lasterne reduceres. Resultaterne indikerer at brug af to forskellige flap aktuatorer er fordelagtig i situationer med en kompleks anstrømning.

Fuld skala vindmølle målinger præsenteres, og det indikeres at flap rod momentet kan bruges som input til en kontrolmetode. En ny metode, hvor dette moment benyttes som sensorinput til en last reducerende kontrolmetode bliver præsenteret. Beregninger påviser metodens anvendelighed og robusthed. Metoden påvises at kunne anvendes for 3D vingeprofiler med flere bagkantsflapper, adskilt af mellemrum.

Strømningen i og omkring slipstrømmen af en udbøjet flap ved et Reynoldstal på 1.63 MIO er undersøgt under instationære forhold. En kontrol metode for to uafhængie flapper i en vinges længderetning er implementeret og præliminære last reduktioner er påvist.

Det er påvist at omsvøbte randbetingelser er en anvendelig og alsidig metode til undersøgelse af bevægelige bagkantsflapper. Resultaterne af nærværende arbejde vil indgå i fremtidige undersøgelser af de instationære strømningsforhold omkring sådanne indretninger.

Contents

Symbols

Latin

$a_{1/3,1}$	strain gage measurement	
a_c	geometric influence coefficient	
$\boldsymbol{a}$	acceleration vector	
A_i	cell area	
c_p	pressure coefficient	$c_p = \frac{p-p_\infty}{\rho_\infty/2\cdot U^2}$
C	chord length	
C_d	drag coefficient	$C_d = \frac{F_d}{\rho/2\cdot U^2\cdot C}$
C_{dp}	drag coefficient, pressure contribution	
C_{dv}	drag coefficient, viscous contribution	
C_f	flap chord	
C_h	hinge moment coefficient	$C_h = \frac{M_h}{\rho/2\cdot U^2\cdot C^2}$
C_l	lift coefficient	$C_l = \frac{F_l}{\rho/2\cdot U^2\cdot C}$
$C(i,j)$	covariance matrix	
$CD_{k\omega}$	positive part of cross-diffusion term	
d	distance	
d_p	Pitot tube length	
D	controller constant	
D	diameter	
e	error	
E	relative flap length	$E = C_f/C$
f	forcing term	
f	frequency	
F	blending function	
F_l	lift force	
F_d	drag force	
$\boldsymbol{F}$	force vector	
h	representative mesh size	
I	controller constant	
J	Jacobian	
k	reduced frequency	$k = \frac{\pi f C}{U}$
k	turbulent kinetic energy	
M_x	flap-wise blade root bending moment	
M_y	edge-wise blade root bending moment	
M_h	hinge moment	
n	time step	
n	normal distance	
N	number of cells	
p	pressure	
p_t	total pressure	$p_t = (p - p_r) + \frac{\rho}{2}\lvert V\rvert^2$
p_r	reference pressure	
P	controller constant	
$\boldsymbol{P}$	pressure forces	
$\boldsymbol{r}$	position vector	
r	radius	
r	relaxation parameter	

r_{21}/r_{32}	grid refinement ratios	
R	radial position	
$R(i,j)$	correlation	
$\boldsymbol{R}$	displacement vector	
Re	Reynolds number	$\mathrm{Re} = UC/\nu$
s	distance coefficient	
S	triangle area	
$\boldsymbol{S}$	body forces	
T_g	gain constant	
t	time	
t	relative thickness	
t	distance coefficient	
t^*	non-dimensional time	
Ti	turbulence intensity	
u	velocity component in x-direction	
U	inflow velocity	
$\boldsymbol{U}$	velocity vector	
$\widetilde{\boldsymbol{U}}$	predicted velocity vector	
v	velocity component in y-direction	
$\boldsymbol{v}$	forcing velocity vector	
$\boldsymbol{v_{ib}}$	immersed boundary velocity vector	
V	local velocity	
w	velocity component in z-direction	
W	wind speed	
x	coordiante	
y	coordiante	
y	wall distance	
z	coordiante	

Greek

α	angle of attack	
β	constant in turbulence model	
δ	flap deflection	
ϵ	flap efficiency factor	
η	curvilinear coordinate	
κ	von Kármán constant	
ν	kinematic viscosity	
ν_t	turbulent eddy-viscosity	
Ω	absolute vorticity	
$\boldsymbol{\Omega}$	angular velocity vector	
$\boldsymbol{\Omega}$	vorticity vector	$\boldsymbol{\Omega} = \boldsymbol{\nabla} \times \boldsymbol{U}$
ω	specific dissipation	
ϕ	variable placeholder	
ϕ	pitch angle	
φ	variable placeholder	
Φ	phase difference	
ρ	density	
ρ	reduction	
σ	standard deviation	
σ	constant in turbulence model	
σ^2	variance	
τ	time constant	

ξ	curvilinear coordinate

Abbreviations

ATEF	Adaptive Trailing Edge Flap
BEM	Blade Element Momentum
CFD	Computational Fluid Dynamics
DTEG	Deformable Trailing Edge Geometry
FFT	Fast Fourier Transform
GCI	Grid Convergence Index
IB	immersed boundary
IBM	immersed boundary method
LES	Large Eddy Simulation
LIDAR	Light Detection And Ranging
MPI	Message Passing Interface
NACA	National Advisory Committee for Aeronautics
NCAR	National Center for Atmospheric Research
RHS	Right Hand Side
SIMPLE	Semi-Implicit Method for Pressure-Linked Equations
SNR	Signal-to-Noise Ratio
TEF	Trailing Edge Flap
URANSE	Unsteady Reynolds Averaged Navier-Stokes Equations

Part I.

Introduction

1. Outline of dissertation

This dissertation is divided into four parts: Introduction, Numerical Methods, Applications and Conclusion & Perspectives. The first part will give a general introduction to the two fields of research that were brought together in the present work, namely the 'smart wind turbine rotor' and the immersed boundary method.

The second part will describe the latest implementation of the immersed boundary method inside the EllipSys flow solver and it will present validation test cases. It will be described how the immersed boundary can be applied alongside with standard body fitted meshes. This hybrid approach will be applied to airfoils with moving trailing edge flaps, as they appear in smart rotor designs.

The third part of the dissertation will present applications of the hybrid approach to load alleviation problems with two dimensional flow and it will present the abilities of the hybrid approach to model complex three-dimensional trailing edge flap geometries.

In the last part, a conclusion will be drawn and perspectives on the hybrid immersed boundary will be discussed.

2. Smart rotor research

At utility scale, the three-bladed upwind turbine concept is the de facto standard in generating electricity from wind. For newer wind turbine design, one main driver in reducing the cost of energy is increasing the rotor diameter. Rotor diameters currently exceed 120m, and some planned offshore turbines use rotor diameters of up to 164m. Sites with lower average wind speeds and sites in complex terrain with high turbulence levels become more and more important for already matured onshore markets.

Wind turbine blades experience a broad variety of aerodynamically induced fatigue loads from yaw error, wind shear and wind turbulence. Extreme operating conditions - e.g. strong gusts, emergency shutdown, parked conditions in high wind - further generate large extreme loads on their structure. Both fatigue and extreme loads are also transfered to all major wind turbine components, causing damage and thereby influencing or driving the component's design.

Different systems, such as passive bend-twist coupling or active individual pitch controls, can be used to alleviate loads. In [42], individual pitch controls have demonstrated a large potential for load reduction. Nevertheless, those systems also lead to greater wear and tear on the pitch bearings and in general have a slower reaction time due to large masses being rotated. Since the blade also acts as a low-pass filter, the bandwidth of full-blade actuators is limited to low frequencies. Furthermore, it is not possible to have different actuations for different radial positions. For larger turbines, this becomes increasingly problematic as the blades might experience a large difference in aerodynamic conditions along their span.

For future generations of wind turbines, the use of smart rotor systems is perceived as a promising way to decrease the cost of wind energy [11]. Those systems use distributed sensing and span-wise distributed aerodynamic control surfaces to reduce changes in the aerodynamic loads. This reduction then enables e.g. larger rotor diameters, reduction in the tower bill of material or placement in complex terrain with extreme turbulence levels (including wake conditions). The research in the area has amongst others been surveyed in [11, 36].

In general, the smart rotor concept can be divided into three different levels (illustrated in Fig. 2.1): full turbine, full blade and two dimensional airfoil. Both load reductions and cost savings have to be demonstrated at the end of the design process on the top turbine level. A top level controller has to be implemented here, which takes into account the full turbine state. The full blade with the distributed aerodynamic devices is mainly a challenge for the system integration and the aerodynamics. Usually, the three dimensional aerodynamic effects are not taken into

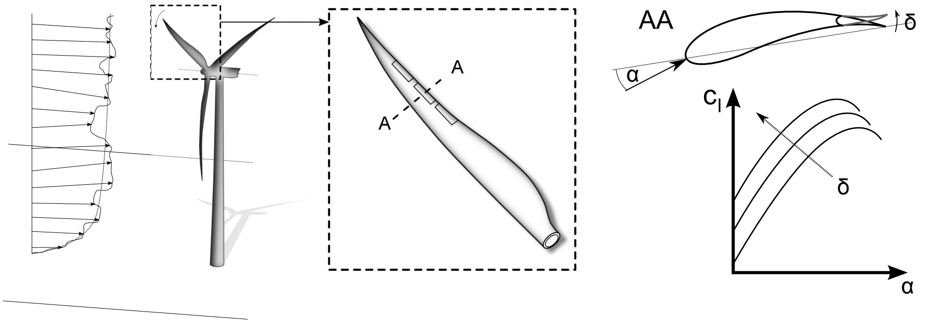

Figure 2.1.: *Smart rotor concept levels: turbine, blade, airfoil*

account. At the moment, blade element momentum (BEM) codes only apply various unsteady aerodynamic models to the span-wise sections, while there are some models which take into account the unsteady aerodynamics and span-wise effects through wake coupling (see e.g. [7]).

For research on control surfaces and control algorithms, one generally uses 2D airfoil computations due to the relatively low resource requirements. Wind tunnel experiments are mostly found to investigate extruded 2D sections. While there are a lot of interactions between all the different fields, those interactions are rarely the topic of published research (some exceptions are the experiments conducted at TU Delft [80, 81]).

In addition to the reviews mentioned above, the following sections shall give an introduction to some of the topics with special relevance to this dissertation: control surfaces, sensors and actuators.

2.1. Sensors

Before one can alleviate loads actively, a sensor input is required. For smart rotor application, this input can be highly integral, as for example the tower root bending moment. However, it can also be a local flow state, as for example a sectional angle of attack at a single span-wise position.

Here, we focus on the sensors that could be applied to a blade, while the sensing of the rest of the turbine shall be neglected. The most integral values of the blade are normally the blade root bending moments, which can be measured by strain gages. An application of blade bending moments as control input is presented in [9]. The author of [5] used blade root bending moments as well as local accelerations to derive total blade loads and tip deflections in simulations. The strain gage is limited through its life time, signal drift and temperature dependency. Another way to gain knowledge of the full blade's state can be optical deflection measurements, though those have not been demonstrated in the context of smart rotors, yet.

Information about the flow field in front of the rotor can for example be obtained through LIDAR[1] measurements from the nacelle, the hub [56, 33] or from the blade's leading edge[2].

The wind tunnel test [9] and the full scale tests [19, 46] applied Pitot tubes to obtain the local angle of attack and flow velocity with a high accuracy. Problems with these probes are for instance their lightning protection, their costly production and calibration as well as the need for an additional purge system to clean the pressure holes. The differential pressure of two single pressure tabs provided a sensor input to load control in [30]. That method can also be seen as being similar to using a Pitot tube.

Finally, to get the best estimate of the local airfoil aerodynamic coefficients, a number of pressure tabs distributed on both the pressure and the suction side of a section can be used to obtain the local flow state [46].

2.2. Control surfaces

Of the broad variety of active aerodynamic control surfaces that have been investigated, Fig. 2.2 shows four popular concepts. These concepts all change the effective camber of the airfoil by directly modifying the airfoil geometry. The trailing edge

---

[1] Light Detection And Ranging: In wind turbine a context this refers esp. to laser based measurements of flow properties like wind speed and wind direction

[2] e.g. in a project sponsored by the Danish National Advanced Technology Foundation (Højteknologifonden) between LM Wind Power, NKT Photonics and Risø-DTU

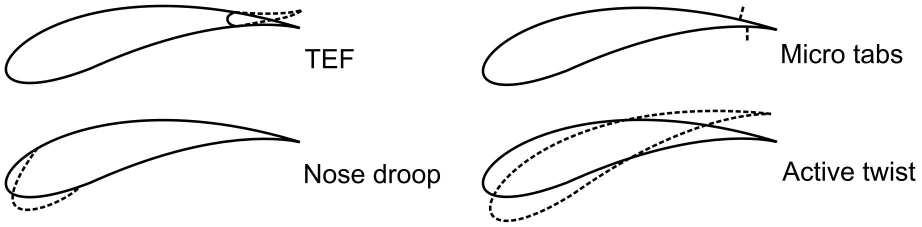

Figure 2.2.: *Control surface concepts*

flap (TEF) and the nose droop are considered to be the most common ones, with a wide area of applications in aerospace technology. The devices used to provide higher maximum lift for take-off and approach of aircraft are commonly called flaps. The use of flaps on wind turbines is more similar to aircraft ailerons, which control the aircraft's roll state. Nevertheless, the use of the word 'flap' for load alleviation devices has been widely adapted and this thesis does not deviate. Morphing trailing edge geometries or deformable trailing edge geometries (DTEG) are still grouped here as flaps, since they follow the same basic idea of moving the trailing edge as a whole to alter the aerodynamic lift. Fig. 2.3 shows some estimates for the flap efficiency in terms of equivalent angle of attack change. Numerous research has been conducted on flaps for wind turbines - proving their potential to achieve significant load reductiosn. In [18] the authors investigated the aeroelastic response of an elastically mounted airfoil with a deflectable trailing edge. They used a potential flow solver [29] and a linear spring/damper model, concluding significant potential for load reduction. In [76], the author showed that smoothly curved (flexible) flap geometries are beneficial for reductions in airfoil noise and drag compared to hinged flaps. An experiment on a small-scale non-rotating blade in a wind tunnel [80] validated the concept of trailing edge flaps for load alleviation under small pitch oscillations. The controller used measurements of the flap-wise bending load. The authors showed load variance reductions of up to 90% for feed forward cases. In a following wind tunnel experiment [81], the authors demonstrated load variance reductions in the order of 90% on a rotating two bladed scale model with a 1.8m diameter. At full-scale, a system demonstrator test on a Vestas V27 turbine [19] delivered first results.

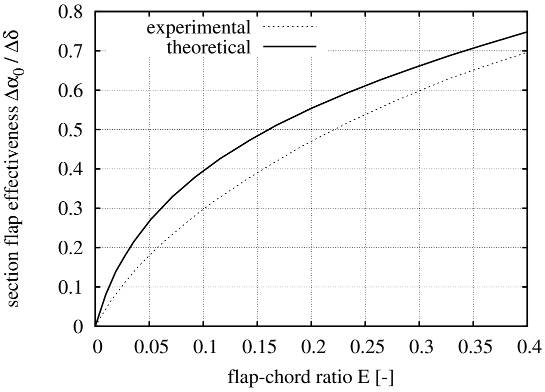

Figure 2.3.: *Flap efficiencies, data taken from [4]*

Further, micro-flaps have seen some interest recently [27, 79]. Those devices can be seen as movable (or rotating) variants of the fixed gurney flap [78].

Micro tabs act as retractable gurney flaps [79], directly influencing the circulation at the trailing edge. Due to their height, they can not be placed directly at the trailing edge (though possible for flat back airfoils). Therefore, these devices are usually placed at a position between 90-95% chord. They are characterized by being small and lightweight and thereby allowing for fast response times. The additional power consumption is supposed to be low due to a very little hinge moment that the actuator has to overcome. Changes in blade surface and structural design are supposed to be minor. Micro tabs have been investigated for example by [79, 86] who give them preference over trailing edge flaps and morphing blade structures, stating that these "must still overcome many other technological hurdles and potentially impractical large energy requirements". Comparing the micro tab concept with an equivalent flap (in terms of lift change) [10] found that "with respect to dynamic response, the flap concept is more well behaved, as the micro tab suffers from a reversed lift response during the initial phase of the movement. [...] the micro tab thus experiences longer time delays for obtaining the desired load changes, which might be critical for obtaining maximum load alleviation."

In active twist applications, the wing or blade structure itself twists and thereby changes the angle of attack along the span. [61] presents a Mach-scaled helicopter rotor of 1.54m that achieved active twist peak-to-peak deflection of 2.1° per meter of blade. In addition to the above mentioned geometry changing actuators, also suction/blowing devices both active and passive are gaining popularity lately.

2.3. Actuators

The choice of any aerodynamic control surface directly leads to strict requirements for the choice of actuation. A fundamental distinction arises for nearly all actuator types. Slow actuators can apply large forces and strokes, while fast actuators are limited to small strokes or small forces. A trade-off is usually possible between stroke and force by for instance mechanical levers.

Actuators based on pneumatics/hydraulic systems have been applied to wind tunnel experiments in a smart rotor context. Examples are Risø's full rubber structure in [3], or the linear pneumatic artificial muscle (PAM) actuators presented in [39].

Shape memory alloy (SMA) actuators consist of alloy wires that contract when being heated, mostly by an electrical current. They are attributed with being light weight, using less space and operating quietly. The larger the wire diameter the longer it takes the wire to cool down again, before the next motion cycle can be started. This restricts the actuators to low frequencies at reasonable forces. Magnetostrictively actuated flaps for vibration reduction in helicopter rotors are presented in [28]. These actuators produce strain when a magnetic field is applied (e.g. by a surrounding wire coil).

Piezo electric benders as actuators have been presented in wind tunnel tests of airfoil sections [7] and rotating turbine models [81].

2.4. ATEF project and contribution of the present work

The Adaptive Trailing Edge Flap (ATEF) project is a collaboration between the Technical University of Denmark (DTU), Risø DTU National Laboratory for Sustainable Energy and Vestas Wind Systems A/S. It was partially funded by the Danish National Advanced Technology Foundation (Højteknologifonden). The project's aim was bringing together knowledge from the different fields (control, aerodynamics, aero-elasticity, system integration) to investigate the use of trailing edge flaps on smart wind turbine rotors. The project consisted of wind tunnel experiments, development of computational tools and demonstration of the concept on a wind turbine at small utility scale [19].

So far, the effect of the unsteady turbine aerodynamics are mainly covered by unsteady aerodynamic models within aero-elastic design codes with a strong focus on engineering application of dynamic stall models. Dynamic stall should be clearly separated from the unsteady aerodynamics in attached airfoil operation. As Leishman points out in his review on unsteady aerodynamics in wind turbine research [44]: *"dynamic stall is certainly a significant unsteady flow problem on many types of wind turbine, [but] it is important to recognize that unsteady airloads will be produced even in the absence of dynamic stall"*. This statement is especially valid for the flow around trailing edge flaps, which might alter the aerodynamic properties of the blade, without leading to large scale flow separation.

To improve the treatment of trailing edge flaps and to decrease uncertainty in the tools, both the development of an unsteady panel code and wind tunnel experiments were conducted. For a better understanding of the prevailing aerodynamic phenomena, the three-dimensional flow field of blades equipped with trailing edge flaps is of particular interest. The gap between the panel codes and the experiments can be bridged by Unsteady Reynolds-Averaged Navier-Stokes (URANS) simulations. In such codes, moving configurations are usually treated with moving or overlapping/overset grids [53] or by a grid interpolations method [76, 34]. Latter method applies an interpolation between two meshes to generate a new mesh for the specified flap deflection at each time step. The method has the drawback, that the flap geometry might shorten when large maximum deflections are used for the base meshes. Moving, overset as well as interpolated meshes require mapping the obtained flow solution on the new mesh geometry.

This work will develop an advanced tool for simulation of the steady/unsteady aerodynamics of trailing edge flap geometries. First, an existing immersed boundary method implemented in the flow solver EllipSys will be revisited and the method will be extended with tools to simulate flows around trailing edge flaps in fixed computational grids.

This dissertation will present a novel way of using the movings flap's hinge moment as control input for load alleviation. Additionally, a control that uses two different actuators in a single flap structure will be investigated. Finally, the feasibility of using the three dimensional code implementation to analyze configurations with multiple flaps will be demonstrated.

3. Immersed boundary methods

3.1. Background

In traditional computational fluid dynamics (CFD), a flow domain is first discretized into a mesh and then boundary conditions are applied to the domain boundaries. These boundary conditions might for instance be inflow/outflow conditions or a wall boundary condition. Therefore, it is advantageous that the computational domain is adjusted to the body geometries that are to be studied. Another option to introduce wall boundaries, is to use an immersed boundary (IB) method. Here, computational meshes are generated such that the mesh does not have to conform to the body boundaries. The body boundary conditions are only later introduced into the governing equations via forcing terms. Fig. 3.1 shows an example for a standard body conformal mesh and an IB representation of a circular cylinder on a Cartesian mesh. The approach to decouple the mesh generation from the actual body geometry makes the method particularly interesting for complex and moving geometries .

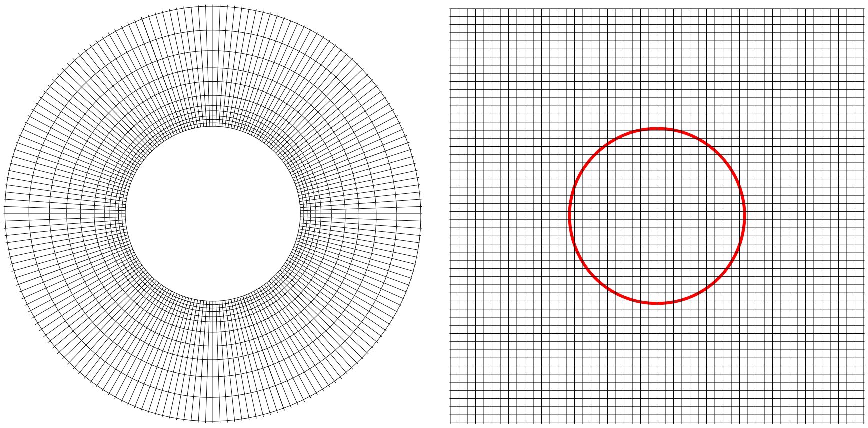

(a) Body-fitted mesh

(b) Non-body fitted Cartesian mesh with immersed boundary (–)

Figure 3.1.: *Different meshing approaches*

Peskin [58] is usually credited with introducing the IB method, when he simulated the flow inside the beating human heart in 1972. A review on immersed boundary methods for solid surfaces can be found in [57]. To give the reader an overview, the basic points of the review will be summarized in the following and the variations of the method will be discussed. Afterwards, current applications of the method to a variety of problems will be presented and areas with special relevance to wind energy are pointed out.

Depending on when the forcing terms to represent the body are introduced into the governing equations, the immersed boundary methods can be divided into two types. The *continuous forcing* methods directly introduce the forcing terms into the governing equations before they are discretized. Accordingly, in the *discrete forcing* methods the effects are introduced after the discretization took place. The continuous approach is particular suited for highly elastic boundaries, while it directly leads to a stiffening[1] of the governing equations for rigid boundaries.

---

[1] Stiff differential equations might experience instabilities where small changes for some terms can quickly change the solution unless very small step sizes are used in the discretization.

The discrete approaches can be divided further into two types of methods, depending on the imposition of the boundary condition. Indirect methods use a distribution function, which extends the forcing into the region outside the solid body. Direct methods are popular for high Reynolds number flows, because they do not spread out the influence of the forcing term but allow for a sharp representation of the boundary.

Open issues with the immersed boundary method are the use of wall functions and applications with higher order of accuracy.

3.2. Immersed boundaries for turbulent flows

While the majority of applications of the IB method are for very low Reynolds numbers and laminar flows, a variety of turbulence models has been applied to medium and high Reynolds regimes. Both the Spalart-Allmaras one-equation [71] and the Wilcox [84] two-equation model have been applied by [37, 38] with first examples for gas turbine blade passages.

Large eddy simulations (LES) were presented by Tessicini et al. [74] with different near wall models, studying the flow past a hydrofoil trailing edge. In [26] the IB method was applied together with a dynamic Smagorinsky model [67, 50] to airfoils at high angles of attack and a Reynolds number of $\mathrm{Re} = 50.000$.

In this work, a modified k-ω SST model [51] is introduced.

3.3. Advantages and drawbacks

The immersed boundary methods have some inherit advantages compared to classical CFD. Even for seemingly simple geometries generating a body-fitted structured grid is not always straightforward. With an immersed boundary method, the grid generation process is greatly simplified and for moving geometries, there is no need to re-generate the grid at every time step. Projecting the old solution onto the new grid, as it is done in moving grid methods, can affect accuracy, robustness and stability of the solution (especially for large body motions). When using a purely uniform Cartesian grid, the solver's operations per grid point can be considerably reduced while the structured grid allows for line iterative methods and geometric multi grid methods.

Of course the IB method also has some drawbacks. The imposition of the boundary conditions is not straightforward and accuracy as well as the convergence behavior are not obvious. One of the most important problems is the mesh resolution close to the wall. In a Cartesian grid, the user has less control over the grid resolution in the wall regions. Cells have to be distributed in such a way as to make sure the walls are sufficiently resolved at any time. This poses a challenge when moving geometries are involved or if the flow is investigated at high Reynolds numbers. Following [57], the grid size ratio between a classical body-fitted boundary layer grid and an uniform Cartesian grid scales with (Re^{1}) in 2D, but ($\mathrm{Re}^{1.5}$) in 3D. This means at high Reynolds number the grid size might be a limiting factor when comparing with standard body-fitted grids. One way to mitigate this effect is to use underlying curvilinear meshes. In [62] combinations of an immersed boundary method with curvilinear meshes are demonstrated. The same level of accuracy as for Cartesian meshes was demonstrated while considerably reducing computational cost. For geometries esp. suited for curvilinear meshes (e.g. circular cylinders), the accuracy was even increased. [31] simulated the internal flows around a mechanical bileaflet heart valve in a curvilinear mesh. Here, the main benefit was that the curvilinear grid could be used to efficiently represent the outer shape of the flow domain.

3.4. Applications

A broad range of applications for the immersed boundary method has been published. The method is especially gaining popularity for problems concerning fluids-structure-interaction. Recent examples of the wealth of research can be found in the proceedings of the 2009 Euromech colloquium on the topic [2]. Some examples in biological flows are swimming fish, flying insects, cardiovascular flow, thrombocytes flow and multi cellular growth. The applications range further to car aerodynamics (external and underhood flow), nuclear application (flow in nuclear fuel elements, buoyancy driven gas bubbles) to inflating parachutes and flow around buildings. In [20] the authors calculate the flow around a walking person.

Apart from the above applications, there are other studies with a special relevance to wind energy. In the field of flow control, [59] and [63] presented work in which they model vortex generators (passive and active respectively) on airfoil sections by introducing them as immersed boundaries. For flows in complex terrain the IB method also shows potential as demonstrated in [35], presenting large eddy simulations (LES) of Risø's Bolund experiment [12]. [45] presented an IB method to model complex terrain coupled with the Weather Research and Forecasting (WRF) model of NCAR [66]. Finally, first simulations of the flow around a coarse representation of a three-bladed wind turbine using a combined IB-LES approach for wake studies are presented in [73].

This work will concentrate on applying an immersed boundary method to solve problems regarding airfoils with moving trailing edge flaps.

Part II.

Numerical methods

4. Implementation of the immersed boundary method

4.1. The EllipSys platform

The flow solver EllipSys was developed at Technical University of Denmark (DTU) [54] and Risø National Laboratory for Sustainable Energy [69]. It solves the incompressible governing equations in curvilinear coordinates applying domain decomposition and multi-grid methods [55]. The code uses a cell-centered finite volume discretization of the incompressible Navier-Stokes equations in primitive variables (pressure-velocity). A predictor-corrector method is used. In the predictor step, the momentum equations are time discretized using a second-order backward differentiation scheme. For the discretization in space, a second-order central differences scheme is applied, except for the convective terms which are discretized by the QUICK upwind scheme. In the corrector step, an improved Rhie-Chow interpolation [65] is used, which helps avoiding numerical oscillations from pressure decoupling. An improved SIMPLEC scheme for collocated grids [64] is used to make the unsteady solution independent of the applied relaxation parameters. A five-level multi-grid technique solves the Poisson equation for the pressure. The code is parallelized by using the Message Passing Interface (MPI).

This work focuses on the unsteady Reynolds Averaged Navier-Stokes (URANS) equations together with a k-ω SST turbulence model [69].

When implementing an immersed boundary method as an addition to the existing solver, the high desired Reynolds number together with rigid boundaries without structural feedback directly led to the choice of a direct forcing method. A first version of the EllipSys code for handling vortex generators as immersed boundaries can be found in [59]. A reviewed scheme using the direct one-point forcing approach is used in the present work.

The implementation of the method in the 2D code will be discussed in the following sections. First, the turbulence model will be presented and the boundary conditions for the turbulence model at the immersed boundary will be defined. Then, the calculation of the forcing term will be derived, followed by a presentation of the necessary geometry description, cell tagging and interpolation methods as well as the calculation of the pressure forces and the viscous forces. Finally, the differences between the 2D and 3D implementation will be pointed out.

4.2. Calculation of the forcing term

The incompressible Reynolds averaged Navier-Stokes equations[1] and the continuity equation read:

$$\begin{aligned}\frac{\partial U_i}{\partial t}+\frac{\partial\left(U_iU_j\right)}{\partial x_j} &= \frac{1}{\rho}\frac{\partial\left(p+\frac{2}{3}\rho k\right)}{\partial x_i}+\frac{\partial}{\partial x_j}\left(\left(\nu+\nu_t\right)\left(\frac{\partial U_i}{\partial x_j}+\frac{\partial U_j}{\partial x_i}\right)\right)+f_i\\ \frac{\partial U_i}{\partial x_i} &= 0 \qquad (4.1)\end{aligned}$$

with ρ, $U_{i/j}$, p, ν, f_i, being the density, the velocity components, the pressure, the kinematic viscosity and the forcing term, respectively. The turbulence model[2] supplies the turbulent eddy viscosity ν_t and the turbulent kinetic energy k.

---

[1] in compact tensor notation

[2] see section 4.4 later

Time discretization of the above equations yields

$$\frac{U_i^{n+1}-U_i^n}{\Delta t}=\mathrm{RHS}^{n+1/2}+f_i^{n+1/2} \tag{4.2}$$

The right hand side RHS stands for the convective, viscous and pressure-gradient terms. The notation $n+1/2$ means that the forcing terms are computed before the velocity, but at the same time step[3].
If one wants to obtain a desired velocity v_i in the forcing cells, the forcing term becomes

$$f_i^{n+1/2}=-\mathrm{RHS}^{n+1/2}+\frac{v_i^{n+1}-U_i^n}{\Delta t} \tag{4.3}$$

The desired velocity v_i^{n+1} has to be found by an interpolation with the surrounding cells, so that the boundary condition is fulfilled on the immersed body (e.g. static no-slip condition $\mathbf{v}_{ib}=0$). The interpolation method will be presented in section 4.3.
When transforming the flow equations to curvilinear coordinates

$$(x,y)\Rightarrow(\xi,\eta)$$

one obtains the partial differentials in 2D as:

$$\begin{aligned}\frac{\partial}{\partial x}&=\frac{1}{J}\left(\frac{\partial}{\partial\xi}\alpha_{\xi x}+\frac{\partial}{\partial\eta}\alpha_{\eta x}\right)\\ \frac{\partial}{\partial y}&=\frac{1}{J}\left(\frac{\partial}{\partial\xi}\alpha_{\xi y}+\frac{\partial}{\partial\eta}\alpha_{\eta y}\right)\end{aligned} \tag{4.4}$$

with J being the Jacobian and $\alpha_{\xi x}=J\xi_x$, $\alpha_{\xi y}=J\xi_y$, $\alpha_{\eta x}=J\eta_x$, $\alpha_{\eta y}=J\eta_y$.
The coordinate transformation leads in the strong conservative form to:

$$\begin{aligned}&\frac{\partial JU}{\partial t}+\frac{\partial C_1U}{\partial\xi}+\frac{\partial C_2U}{\partial\eta}\\ &-\frac{\partial}{\partial\xi}\left(\frac{\widetilde{\nu}}{J}\beta_{11}U_\xi\right)-\frac{\partial}{\partial\eta}\left(\frac{\widetilde{\nu}}{J}\beta_{22}U_\eta\right)\\ &-\frac{\partial}{\partial\xi}\left(\frac{\widetilde{\nu}}{J}\left(\beta_{12}U_\eta+\omega_{11}\alpha_{\xi x}+\omega_{21}\alpha_{\xi y}\right)\right)\\ &-\frac{\partial}{\partial\eta}\left(\frac{\widetilde{\nu}}{J}\left(\beta_{21}U_\xi+\omega_{11}\alpha_{\eta x}+\omega_{21}\alpha_{\eta y}\right)\right)\\ &+\frac{1}{\rho}\left(\frac{\partial P\alpha_{\xi x}}{\partial\xi}+\frac{\partial P\alpha_{\eta x}}{\partial\eta}\right)=\frac{1}{\rho}J(S_U+f_U)\end{aligned} \tag{4.5}$$

---

[3] It can be argued, that the RHS should be noted as RHS^n, but for consistency with the literature, $\mathrm{RHS}^{n+1/2}$ is kept

$$\begin{aligned}
&\frac{\partial JV}{\partial t}+\frac{\partial C_1 V}{\partial \xi}+\frac{\partial C_2 V}{\partial \eta}\\
&-\frac{\partial}{\partial \xi}\left(\frac{\widetilde{\nu}}{J}\beta_{11}V_\xi\right)-\frac{\partial}{\partial \eta}\left(\frac{\widetilde{\nu}}{J}\beta_{22}V_\eta\right)\\
&-\frac{\partial}{\partial \xi}\left(\frac{\widetilde{\nu}}{J}\left(\beta_{12}V_\eta+\omega_{12}\alpha_{\xi x}+\omega_{22}\alpha_{\xi y}\right)\right)\\
&-\frac{\partial}{\partial \eta}\left(\frac{\widetilde{\nu}}{J}\left(\beta_{21}V_\xi+\omega_{12}\alpha_{\eta x}+\omega_{22}\alpha_{\eta y}\right)\right)\\
&+\frac{1}{\rho}\left(\frac{\partial P\alpha_{\xi y}}{\partial \xi}+\frac{\partial P\alpha_{\eta y}}{\partial \eta}\right) = \frac{1}{\rho}J(S_V+f_V)
\end{aligned}\tag{4.6}$$

here, U/V are the velocities in x- and y-direction, $S_{U/V}$ are the body forces and $f_{U/V}$ are the forcing terms from the immersed boundary method. The forcing terms are treated like any other additional force. The coefficients in eqn. 4.5 and 4.6 are

$$\begin{aligned}
C_1 &= U\alpha_{\xi x}+V\alpha_{\xi y}\\
C_2 &= U\alpha_{\eta x}+V\alpha_{\eta y}\\
\beta_{11} &= \alpha_{\xi x}\alpha_{\xi x}+\alpha_{\xi y}\alpha_{\xi y}\\
\beta_{12} &= \alpha_{\xi x}\alpha_{\eta x}+\alpha_{\xi y}\alpha_{\eta y}\\
\beta_{21} &= \alpha_{\eta x}\alpha_{\xi x}+\alpha_{\eta y}\alpha_{\xi y}=\beta_{12}\\
\beta_{22} &= \alpha_{\eta x}\alpha_{\eta x}+\alpha_{\eta y}\alpha_{\eta y}\\
\omega_{11} &= \alpha_{\xi x}U_\xi+\alpha_{\eta x}U_\eta\\
\omega_{21} &= \alpha_{\xi x}V_\xi+\alpha_{\eta x}V_\eta\\
\omega_{12} &= \alpha_{\xi y}U_\xi+\alpha_{\eta y}U_\eta\\
\omega_{22} &= \alpha_{\xi y}V_\xi+\alpha_{\eta y}V_\eta
\end{aligned}\tag{4.7}$$

In the finite-volume discretized equations the forcing term becomes in vector notation, dropping the time step labels:

$$\mathbf{f}=-\mathbf{S}+\sum_{c=e,w,s,n}a_c\mathbf{U}_c+\mathbf{v}\mathbf{a}_p \tag{4.8}$$

where a_c are the influence coefficients of the bordering cells with compass summation notation, while a_p is the center node influence coefficient[4]. With the obtained values for f, we can update the predicted velocity field $\tilde{\mathbf{U}}_p$ in the forcing cells at every sub-step as

$$\tilde{\mathbf{U}}_p=\left(\mathbf{f}+\mathbf{S}-\sum_{c=e,w,s,n}a_c\mathbf{U}_i\right)/\mathbf{a}_p \tag{4.9}$$

where S denotes the pressure and body forces, the subscript P indicates the evaluation at the present cell and i is the index of the neighboring cells.
The desired velocity $\mathbf{v}$ in eqn. 4.8 can be set directly to the velocity of the moving boundary, only if it is passing exactly through the cell center. In general the immersed boundary does not coincide with the cell center. Therefore, an interpolation procedure to the present cell center becomes necessary. The following section describes the applied interpolation for the desired velocity in the forcing cells.

---

[4] see [69] for details

4.3. Geometry description and velocity Interpolation

The immersed boundary is described through an input file containing a closed polygonal line consisting of a fixed number of marker points IB(i). This polygon is used when evaluating the inside/outside cells and when calculating the appropriate forcing velocity in the forcing cells.

4.3.1. Cell tagging

The first step when applying the immersed boundary method is to identify and tag the cell-centers inside the fictive body. A simple ray tracing method is one of the easiest ways to distinguish between inside and outside cells. A virtual ray is emitted at a cell center and one counts the number of times that the ray crosses the immersed boundary. Fig. 4.1 shows that each ray leaving from inside the body has to cross the immersed boundary an odd number of times. Rays from the outside will cross the boundary an even number of times. One can apply this concept to all cell centers and tag them accordingly as inside/outside. After the inside cells (or body cells) are identified, the layer of neighboring outside cells can be tagged so that the inner cells are completely surrounded (Fig. 4.2). In these neighboring cells, the forcing terms are applied to the momentum equations in such way as to fulfill the no-slip and impermeable wall condition at the stationary or moving fictive body surface. Therefore, the cells are called 'forcing cells'.

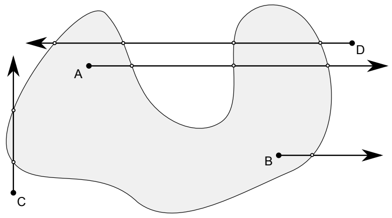

Figure 4.1.: *Raytracing*
○ intersection points, ● starting point, → ray, ◡ boundary

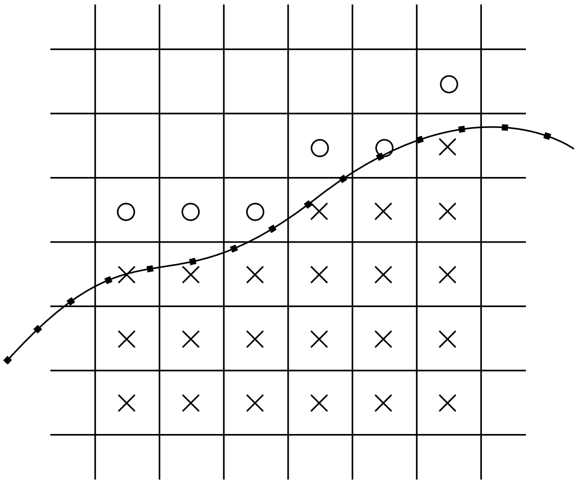

Figure 4.2.: *Sketch, forcing/inside points, ○ forcing cells, × body cells, ■ marker points*

The flow equations are solved in the whole computational domain including all cells inside the fictive body boundaries, which qualifies as a drawback of this method, since it means possibly calculating a large overhead[5]. The flow inside the immersed boundary may grow as time increases. In the current approach, the influence coefficients of the bordering cells (see eqn. 4.8 and 4.9) are set to zero, such that flow is blocked from the outside of the immersed boundary and the velocity components are kept zero.

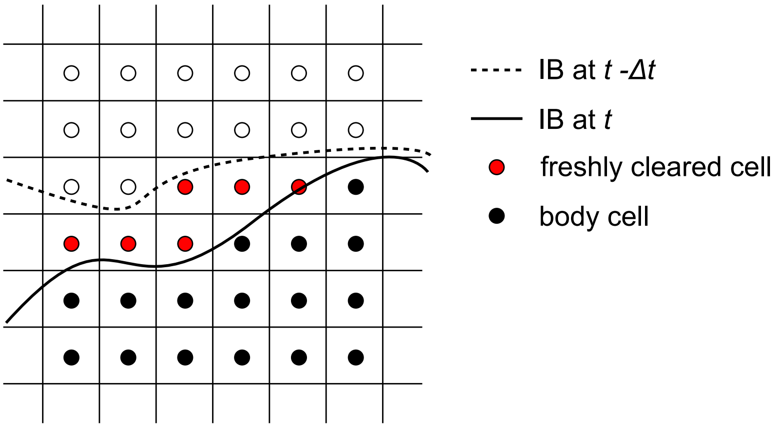

Figure 4.3.: *Freshly cleared body cells*

---

[5] It might be considered a plus for moving boundaries where fresh forcing cells can have appropriate initial values assigned (Fig. 4.3), see also field extension method of [85].

4.3.2. Interpolation

The necessary velocity interpolation for each forcing point might be handled by one or two linear interpolations depending on the number of neighbor points inside the body. Fig. 4.4 shows an example within a simple Cartesian grid. For two linear interpolations, the resulting value is an average of both interpolations. Fig. 4.5 shows an example of the linear interpolation. Firstly, the polygonal segment (blue) that intersects with the line between the neighboring inner cell and the forcing cell is identified. To find the cross-point of two line segments $[(x_1, y_1), (x_2, y_2)]$ and $[(x_3, y_3), (x_4, y_4)]$ one might use the following equations:

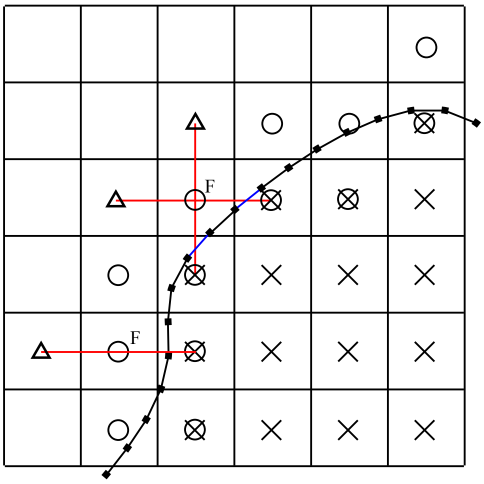

Figure 4.4.: *Sketch, forcing/inside points* ○ *forcing cells,* × *body cells,* ⊗ *inner cell,* ■ *IB marker points,* △ *outer cell*

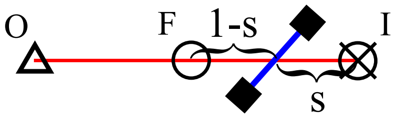

Figure 4.5.: *Sketch, forcing/inside points* ○ *forcing cells,* × *body cells,* ⊗ *inner cell,* ■ *IB marker points,* △ *outer cell*

$$t = \frac{(y_4 - y_3)(x_3 - x_1) + (x_4 - x_3)(y_1 - y_3)}{(x_2 - x_1)(y_4 - y_3) - (y_2 - y_1)(x_4 - x_3)}$$

$$s = \frac{(y_2 - y_1)(x_3 - x_1) + (x_2 - x_1)(y_1 - y_3)}{(x_2 - x_1)(y_4 - y_3) - (y_2 - y_1)(x_4 - x_3)}$$

The cross-point exists only when $0 \leq t \leq 1$ and $0 \leq s \leq 1$. If it does exist, the cross-point can be found by the ratio t or s:

$$x_c = (1 - t)x_1 + tx_2 = (1 - s)x_3 + sx_4$$

$$y_c = (1 - t)y_1 + ty_2 = (1 - s)y_3 + sy_4$$

Accordingly, one can obtain the forcing velocity $\mathbf{v}$ by interpolating between the boundary velocity of the segment $\mathbf{U}_{\text{seg}}$ and that of the outer cell $\mathbf{U}_{\triangle}$. We define $\tilde{s}$ under the assumption that the forcing point lies in the exact middle of a line connecting the outer cell and the inner cell.

$$\tilde{s} = \frac{1-s}{2-s}$$

$$\mathbf{v} = (1-\tilde{s})\mathbf{U}_{\mathrm{seg}} + \tilde{s}\mathbf{U}_{\triangle}$$

The identified line segment of the immersed boundary is then used to calculate the normal distance d between the forcing point and the segment (Fig. 4.7). This is done by calculating the three sides a, b, c of the triangle $\overline{IB(i+1), F, IB(i)}$ and applying Heron's formula[6]

$$a = \sqrt{\left(x_{IB}(i) - x_{ib}(i+1)\right)^2 + \left(y_{ib}(i) - y_{ib}(i+1)\right)^2}$$

$$b = \sqrt{\left(x_F - x_{ib}(i)\right)^2 + \left(y_F - y_{ib}(i)\right)^2}$$

$$c = \sqrt{\left(x_F - x_{ib}(i+1)\right)^2 + \left(y_F - y_{ib}(i+1)\right)^2}$$

$$l = \frac{a+b+c}{2}$$

giving the area S and consequently the distance d:

$$S = \sqrt{l(l-a)(l-b)(l-c)}$$

$$d = \frac{2S}{a}$$

To calculate the normal distance n_{ib} of every cell-center (CC) to the immersed boundary, first the marker point with minimum distance d is found. The minimum of the normal distances n_1, n_2 to the two line segments attached to the marker point is then stored in n_{ib} (see Fig. 4.7).

$$n_{ib} = \min(n_1, n_2)$$

The resulting values of the normal distance are interpolated from the cell center to the cell vertices. Afterwards, they are interpolated back to cell-centered values resulting in a smoothed distribution of the normal distances. The normal distances are required for the turbulence model shown in the following section.

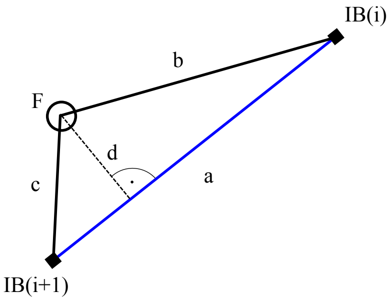

Figure 4.6.: *Distance between forcing point and IB line segment; ○ forcing cells, ■ marker points*

---

[6] see e.g. Weisstein, Eric W. "Heron's Formula." From MathWorld–A Wolfram Web Resource. http://mathworld.wolfram.com/HeronsFormula.html

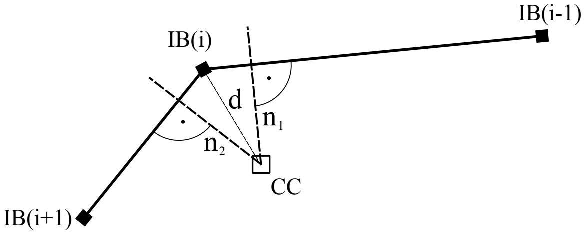

Figure 4.7.: *Distance between forcing point and two IB line segments;* ■ *marker points*

4.4. Turbulence model

The simulations presented in this thesis have been carried out using the k-ω shear-stress transport (SST) model of Menter, in the version presented in [51][7]. The model is a two equation turbulence closure of the turbulent kinetic energy k and the specific dissipation ω. The model combines the k-ϵ model of [43] and the standard k-ω model of [84]. The approach blends between the k-ω model close to the walls and the k-ϵ model in the region outside the boundary layer, thereby benefiting from the advantages of both models for these two flow regions.

The equations and coefficients from [51] will be repeated below, before introducing the additional wall conditions for the immersed boundary method.

The two transport equations for the turbulent kinetic energy k and for the specific dissipation ω are

$$\frac{\mathrm{D}k}{\mathrm{D}t} = \frac{\tau_{ij}}{\rho}\frac{\partial U_i}{\partial x_j} + \frac{\partial}{\partial x_j}\left[(\nu + \sigma_k \nu_t)\frac{\partial k}{\partial x_j}\right] - \beta^* \omega k \tag{4.10}$$

$$\frac{\mathrm{D}\omega}{\mathrm{D}t} = \frac{\gamma}{\rho \nu_t}\tau_{ij}\frac{\partial U_i}{\partial x_j} + \frac{\partial}{\partial x_j}\left[(\nu + \sigma_\omega \nu_t)\frac{\partial \omega}{\partial x_j}\right] + 2(1-F)\sigma_{\omega 2}\frac{1}{\omega}\frac{\partial k}{\partial x_j}\frac{\partial \omega}{\partial x_j} \tag{4.11}$$

Here, τ_{ij} is the turbulent stress tensor. For the constants in the two transport equations two different sets of constants are used. In the inner domain, close to the wall (1):

$$\sigma_{k1} = 0.85,\ \sigma_{\omega 1} = 0.5,\ \beta_1 = 0.075,\ \beta^* = 0.09,\ \kappa = 0.41,\ \gamma_1 = \frac{\beta_1}{\beta^*} - \sigma_{\omega 1}\frac{\kappa^2}{\sqrt{\beta^*}}$$

and in the outer domain (2):

$$\sigma_{k2} = 1.0,\ \sigma_{\omega 2} = 0.856,\ \beta_2 = 0.0828,\ \beta^* = 0.09,\ \kappa = 0.41,\ \gamma_2 = \frac{\beta_2}{\beta^*} - \sigma_{\omega 2}\frac{\kappa^2}{\sqrt{\beta^*}}$$

The blending between the two sets is done via the blending function F, where φ denotes any of the constants

$$\varphi = F\varphi_1 + (1-F)\varphi_2 \tag{4.12}$$

$$F = \tanh\left(\arg^4\right) \tag{4.13}$$

---

[7] [70] describes the implementation of the baseline (BSL) version in EllipSys and presents validation test cases

$$\arg = \min\left(\max\left(\frac{\sqrt{k}}{0.09\omega y}, \frac{500\nu}{y^2\omega}\right), \frac{4\sigma_{\omega 2}k}{\mathrm{CD}_{k\omega}y^2}\right) \tag{4.14}$$

where $\mathrm{CD}_{k\omega}$ is the positive portion of the cross-diffusion term

$$\mathrm{CD}_{k\omega} = \max\left(2\sigma_{\omega 2}\frac{1}{\omega}\frac{\partial k}{\partial x_j}\frac{\partial \omega}{\partial x_j}, 10^{-20}\right) \tag{4.15}$$

The eddy viscosity is limited (in accordance with Bradshaw [17]) and defined as follows, where Ω is the absolute vorticity:

$$\nu_t = \frac{a_1 k}{\max\left(a_1\omega; \Omega F_2\right)} \quad \text{with } a_1 = 0.31 \tag{4.16}$$

$$F_2 = \tanh\left(\arg_2^2\right) \tag{4.17}$$

The boundary conditions for the k-ω SST model are the wall values of the specific dissipation ω_{wall} and the turbulent kinetic energy k_{wall}. These are also applied in context of the immersed boundary method as follows:

$$\omega_{ib} = \frac{60}{\rho \cdot \beta_1 \cdot (y)^2} \tag{4.18}$$

$$k_{ib} = 0 \tag{4.19}$$

Since there can be both regular wall boundary conditions and immersed boundaries together, the minimum distance to any of them is used in the above equations above.

$$y = \min\left(y, y_{ib}\right) \tag{4.20}$$

Here, y_{ib} is the calculated normal distance from the forcing cell center to the immersed boundary (see section 4.3). Equations 4.18 and 4.19 are also applied inside the IB to ensure smooth transition.

4.5. Integral coefficients

This section describes how the contributions of the immersed boundary to the total force acting on a body can be calculated. The integral forces on the immersed boundaries can be obtained using different methods [41]. We will split the total force, and calculate viscous and pressure contributions separately.

4.5.1. Viscous force

The simple summation over all forcing terms f in the domain

$$\mathbf{f} = -\mathbf{S} + \sum_{c=e,w,s,n} a_c \mathbf{U}_c + \mathbf{v} a_p \tag{4.21}$$

yields the viscous force $\mathbf{F}_v$ on the immersed boundary.

$$\mathbf{F}_v = -\sum \mathbf{f} \tag{4.22}$$

4.5.2. Pressure force

To reduce calculation time or to obtain a smoother distribution of the points for pressure evaluation, a new set of marker points is generated for integration (Fig. 4.8). The points are redistributed evenly along the original geometry[8]. To calculate the pressure forces F_p acting on the new line segment, we need to evaluate the pressure in the nearest forcing point. The point can be found by calculating the distance from every forcing point to the boundary[9]. Afterwards, all found distances are gathered from the processors and compared to each other. The pressure in the closest cell is chosen for evaluation. The overall pressure force on the boundary is the sum of the pressure times the projected segment lengths $\Delta y, \Delta x$, which have to include the appropriate signs. Here, we assume a clockwise orientation of the segment points.

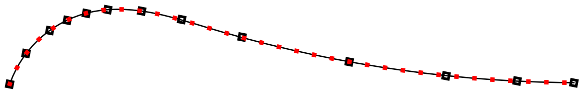

Figure 4.8.: *Redistribution of the immersed boundary marker points*
☐ redistributed point, ■ original marker point

$$\mathbf{F}_p = \sum_{\text{IB}} \left(p \cdot \begin{pmatrix} \Delta y \\ -\Delta x \end{pmatrix} \right) \tag{4.23}$$

---

[8] In case of a trailing edge flap in a hybrid grid (see section 5.2), the two points connecting the body-fitted grid and the immersed boundary are kept the same. This is also important for other sharp edged geometries, since otherwise, one might loose part of the distinct geoemtry features.

[9] This is restricted to points inside the current block corners plus an offset, which should be chosen according to the block shape and cell heights.

4.6. 3D implementation

The implementation of the 3D version of the method is in general analogue to that in 2D. Differences are mainly due to the geometry description of the immersed boundary geometry. Now, the geometry is defined by a minimum of two span wise cuts, which are equivalent to the 2D version plus an additional[10] span wise coordinate. It is possible to define multiple immersed bodies consisting of multiple cuts. Between these cuts the geometry is linearly interpolated. The solid surface is treated as a number of triangles, where for two points of a cut, two triangles are generated with the next cut's points (Fig. 4.9). The two outermost cuts of every body are also filled with triangles to close the body. They might lie outside the computational domain, if desired.

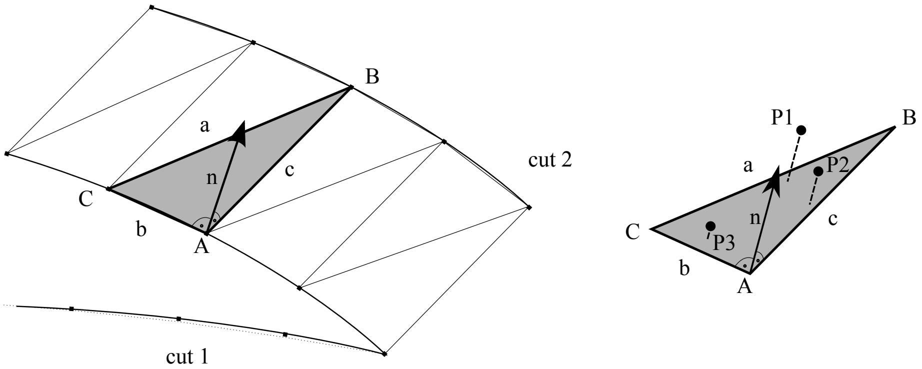

Figure 4.9.: *Geometry representation through triangles* ■ *marker points,* • *cell centers for pressure evaluation*

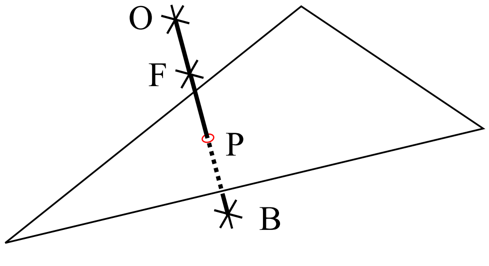

Figure 4.10.: *Three dimensional interpolation*

For the velocity interpolation, Fig. 4.10 shows the three dimensional equivalent of Fig. 4.4, where F is the forcing cell, O is the outer cell and P is the foot point of $\overline{FB}$.

The integral pressure forces in the three dimensional case are found by assigning each triangle a specific pressure from a cell center normal above the triangle's area. If there are multiple points above the triangle when obtaining the integral forces, the average pressure is assigned for evaluation (Fig. 4.9). The normal distance between a cell center and any triangle can be found according to an algorithm based on domain partitioning presented in [25][11]. The averaging of the pressure might lead

---

[10] constant for the whole cut

[11] MATLAB implementation at http://www.mathworks.com/matlabcentral/fileexchange/22857-distance-between-a-point-and-a-triangle-in-3d "*The implementation of the algorithm is designed so that at most one floating point division is used when computing the minimum distance and corresponding closest points.*"

to errors in the integration. Therefore, a refinement algorithm was implemented that splits the triangles along their longest side. Inputs to this algorithm are a maximum desired edge length of the triangles and a maximum number of refinement steps. Fig. 4.11 shows an example output of the algorithm for a flap geometry consisting of three cuts.

In addition to the above integration of the forces on the whole IB geometry, a quasi-2D integration on a spanwise cut was implemented. This method can be used for instance, when investigating an airfoil section under side wall influence.

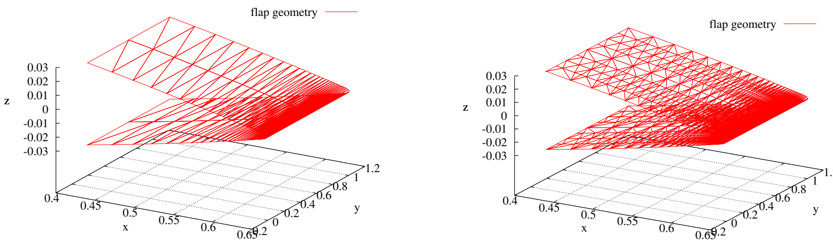

(a) coarse

(b) fine

Figure 4.11.: *Refinement of flap surface triangles (axes not equally scaled)*

5. Validation

To validate the immersed boundary method in EllipSys, different test cases will be presented in this chapter. The first case will be the steady laminar flow around a circular cylinder. The cylinder will be represented fully by an immersed boundary in two different mesh topologies. The solutions will be compared to the literature.
Calculations for a NACA0015 airfoil at $\mathrm{Re} = 5 \cdot 10^4$, where only the trailing edge is modeled by an immersed boundary will introduce the hybrid approach. The results will be compared to those obtained for an equivalent fully body-fitted mesh.
For moving configurations, the computed lift coefficients C_l of an oscillating (pitching) NACA0012 airfoil at $\mathrm{Re} = 1.63 \cdot 10^6$ equipped with an oscillating flap are compared with wind tunnel data and a thin airfoil model.
Finally, 2D airfoil results for the NACA0015 airfoil at $\mathrm{Re} = 5 \cdot 10^4$ are compared with the results obtained by the 3D implementation of the immersed boundary method for an extruded mesh.

5.1. Cylinder test cases

In this section we will compare the results for an immersed boundary representation of a 2D circular cylinder in two different grid configurations. The first type is a Cartesian grid, while the second is an underlying body-adjusted grid. The diameter based Reynolds number is $\mathrm{Re} = 40$ in both cases, which means the flow is laminar and separated.
First the two mesh topologies will be presented and afterwards the results be compared, including a mesh study for each type.

5.1.1. Cartesian grids

The first test case is the flow over a cylinder immersed in a two dimensional Cartesian (rectangular) grid. All lengths are dimensionless by division through the cylinder diameter D. The square domain has a size of $60 \cdot 60$ and is divided into nine blocks with one square central block of dimensions $4 \cdot 4$. The circular immersed boundary was placed in the middle of that block Fig. 5.1. Four different mesh sizes were used (Tab. 5.1). The representative mesh size h is the side length of the square cells inside the middle block. A plot of the distribution of the forcing cells on the three coarsest grids is shown in Fig. 5.2.

	block size	total cells	h
grid A	64^2	$36,864$	0.0625
grid B	128^2	$147,456$	0.03125
grid C	256^2	$589,824$	0.015625
grid D	512^2	$2,359,296$	0.0078125

Table 5.1.: *Cartesian grids, cell numbers and cell sizes*

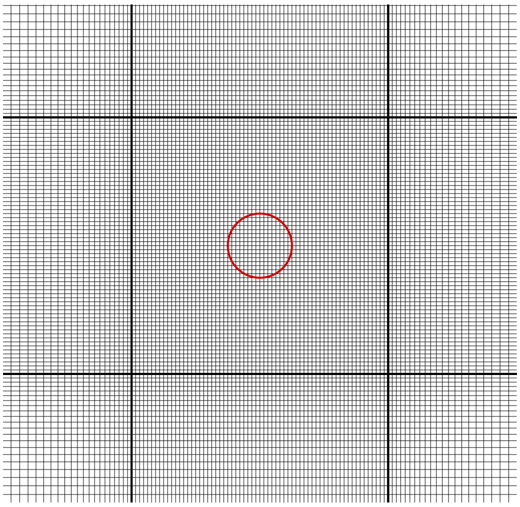

Figure 5.1.: *Immersed boundary cylinder (-) inside the central rectangular mesh section (grid A)*

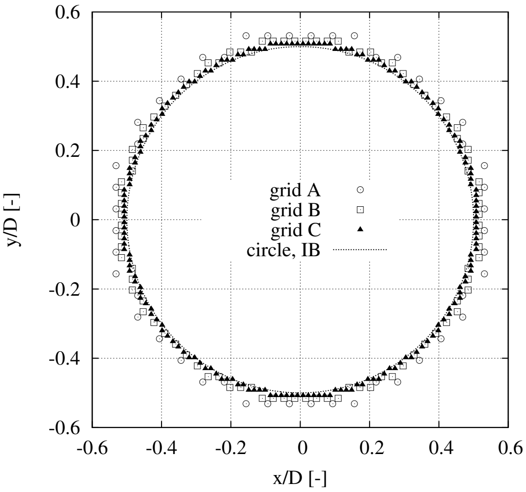

Figure 5.2.: *Forcing points for different grid scales*

5.1.2. Body adjusted grids

For another cylinder test case, the same immersed boundary was used, but together with a different grid topology. Now, the grid was generated as a standard body-fitted grid of a slightly smaller cylinder of a radius of $r = 0.48$. The mesh was set up with a varying cell height in the first normal cells of the cylinder. This was done to ensure that the number of resulting cell centers inside the IB domain (the circle of $r = 0.5$) varied between 3 and 4. This grid type will be called 'body adjusted' in the following, since the grid does not conform with the body, but the overall mesh topology is very similar to the body fitted geometry. The outer domain boundary was a square of side length $l = 44r$, consisting of 4 blocks (Fig. 5.3). The different mesh sizes are tabulated in Tab. 5.2. Here, the representative cell size h is the height of the forcing cell (normal to the boundary) at the interface between the top and left block.

	block size	total cells	h
grid 1	32^2	$4,096$	0.0131
grid 2	64^2	$16,384$	0.0079
grid 3	64^2	$16,384$	0.0046

Table 5.2.: *Cartesian grids, cell numbers and cell sizes*

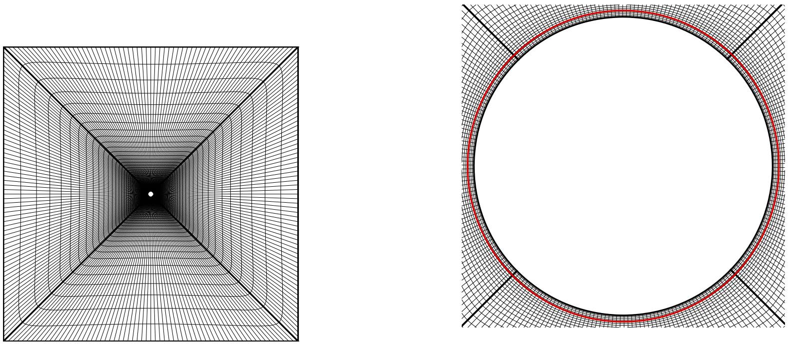

(a) overview

(b) close up, immersed boundary (−)

Figure 5.3.: *2D cylinder on a body adjusted grid*

5.1.3. Results

For both topologies, we recognize the typical flow pattern for a 2D cylinder at very low Reynolds number (Fig. 5.4). The stream lines show the typical pair of vortices that forms after the boundary layer on the cylinder separates. The streamlines are very similar and show that the immersed boundary method is able to enforce the body boundary for both mesh topologies in the coarsest meshes that were used. The non-physical streamlines within the body are plotted in Fig. 5.4(a) solely to show that the computational domain fully covers that region. It can be seen (close up for the body adjusted case in Fig. 5.5), that the separation lines for the body adjusted case clearly originate on the immersed boundary and not on the underlying cylinder boundary of the mesh.

In the following, we will take a closer look at the convergence behavior of the spatial

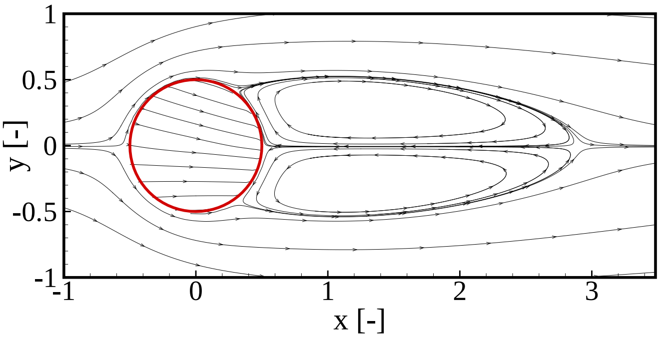

(a) Cartesian grid

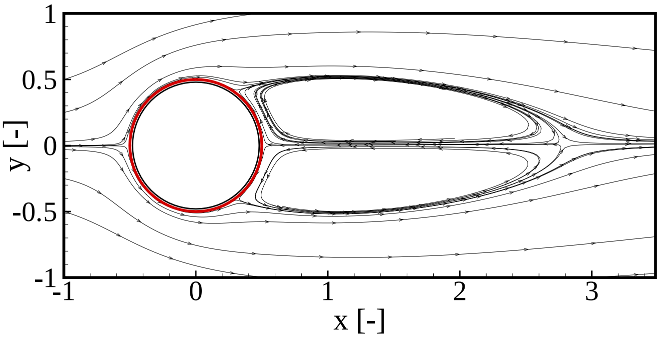

(b) body adjusted grid

Figure 5.4.: *2D cylinder streamlines, immersed boundary (-)*

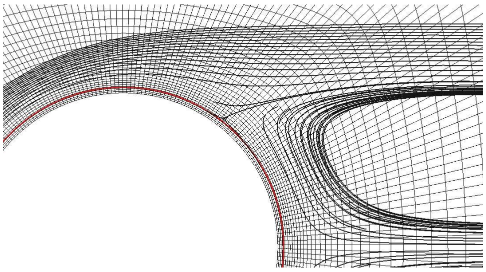

Figure 5.5.: *Cylinder in body adjusted mesh with streamlines,* Re = 40, *immersed boundary (-)*

discretization for the drag coefficient and the separation angle. While doing this, it is important to keep in mind, that two very different mesh topologies were used.

Grid sensitivity study - procedure

For the two global values of total drag coefficient C_d and flow separation angle Θ_s we will compare the convergence behavior of the spatial discretization and estimate the errors. The presented grid studies were conducted according to the ASME procedure [1, 60]. The definitions of that procedure will be quickly summarized for the present cases.

Firstly, a representative cell/mesh size has to be defined for each mesh type. For example in 2D, this might be

$$h = \left[\frac{1}{N} \sum_{i=1}^{N} A_i \right]^{1/2} \tag{5.1}$$

with N being the number of cells and A_i being the cell area, assuming the quantity of interest ϕ is a global values. For a field variables ϕ, the local size can be used.

For the Cartesian grids, it is straightforward to use the side length of the square cells in the middle block. For the body adjusted grids, the normal height of the first outside cell to the immersed boundary is used as an indicator of resolution, since we are mainly interested in the flow close to the immersed boundary.

With the refinement ratios $r_{21} = h_2/h_1$, $r_{32} = h_3/h_2$ and the definition of $\varepsilon_{21} = \phi_2/\phi_1$, $\varepsilon_{32} = \phi_3/\phi_2$ an apparent order p of the convergence can be calculated as:

$$p = \frac{1}{\ln(r_{21})} \left| \ln |\varepsilon_{32}/\varepsilon_{21}| + q(p) \right| \tag{5.2}$$

$$q(p) = \ln \left(\frac{r_{21}^p - s}{r_{32}^p - s} \right) \tag{5.3}$$

$$s = 1 \cdot \operatorname{sign}(\varepsilon_{32}/\varepsilon_{21}) \tag{5.4}$$

For non equal values of r_{21} and r_{32} the values of p and q have to be derived iterative. One can calculate an extrapolated value of the variable ϕ in question by:

$$\phi_{\text{ext}}^{21} = (r_{21}^p \phi_1 - \phi_2)/(r_{21}^p - 1) \tag{5.5}$$

The approximate relative error

$$e_a^{21} = \left| \frac{\phi_1 - \phi_2}{\phi_1} \right| \tag{5.6}$$

The extrapolated relative error

$$e_{\text{ext}}^{21} = \left| \frac{\phi_{\text{ext}}^{21} - \phi_1}{\phi_{\text{ext}}^{21}} \right| \tag{5.7}$$

and finally the fine-grid-convergence index

$$\text{GCI}_{\text{fine}}^{21} = \frac{1.25 \cdot e_a^{21}}{r_{21}^p - 1} \tag{5.8}$$

where the factor 1.25 is a safety factor stated by Roache [60] for high quality mesh studies, while a factor of 3 might be applicable for coarse grids.

Drag coefficients

Tab. 5.3 presents the results of the grid convergence study for the drag coefficient. The drag coefficient showed an oscillating convergence behavior for the body adjusted topology. That topology also resulted in a smaller apparent order than for the Cartesian topology ($0.73 < 1.34$). The extrapolated values of C_d differ by 2.6% between the two topologies. The grid convergence index obtained for the selected grids were 0.66% for the Cartesian and 1.29% for the body-adjusted topology.

	Cartesian	body-adjusted
h_3	0.03125 (B)	0.0131 (1)
h_2	0.015625 (C)	0.0079 (2)
h_1	0.0078115 (D)	0.0046 (3)
r_{21}	2	1.72
r_{32}	2	1.66
ϕ_3	1.60279	1.52323
ϕ_2	1.57132	1.53448
ϕ_1	1.55886	1.52680
p	1.34	0.73
ϕ_{ext}^{21}	1.55069	1.51104
e_a^{21}	0.80%	0.50%
e_{ext}^{21}	0.53%	1.04%
GCI_{fine}^{21}	0.66%	1.29%

Table 5.3.: *Grid convergence behavior for* $\phi = C_d$

Separation angle

The separation angle Θ_S is an important quantity to evaluate the surface representation of the immersed boundary method. Fig. 5.6 shows the geometrical definition of Θ_S.

Tab. 5.4 presents the grid convergence study for the separation angle. Both topologies demonstrate an apparent order p higher than two. The body adjusted topology performs slightly better. Nevertheless, the extrapolated values differ by $\approx 0.5°$. The body adjusted grid achieves a smaller grid convergence index than the Cartesian grid.

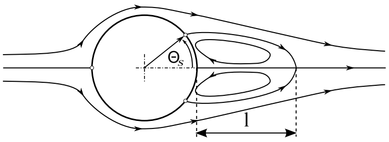

Figure 5.6.: *Geometrical definition of* Θ_S *and* l

Comparison with literature

Out of the vast research on flow around a circular cylinder, some numerical results are presented in Tab. 5.5, together with the present results for the finest grids of both topologies. The present values lie within the rather wide span of published results. It should be noted that both [23, 52] present IB methods.

Fig. 5.7 shows a comparison of the results for the finest body adjusted grid with re-

	Cartesian	body adjusted
h_3	0.0625 (A)	0.0131 (1)
h_2	0.03125 (B)	0.0079 (2)
h_1	0.015625 (C)	0.0046 (3)
r_{21}	2.00	1.72
r_{32}	2.00	1.66
ϕ_3	54.29°	50.97°
ϕ_2	54.63°	52.81°
ϕ_1	52.90°	52.23°
p	2.18	2.35
ϕ_{ext}^{21}	51.99°	51.42°
e_a^{21}	3.27%	1.11%
e_{ext}^{21}	0.81%	0.47%
GCI_{fine}^{21}	1.00%	0.59%

Table 5.4.: *Grid convergence behavior for different test cases, circular grid,* $\phi = \Theta_s$

	C_{df}	C_{dp}	C_d	Θ_s
Sørensen [69]	0.55	1.06	1.61	53.0°
Dennis&Chang [22]	0.524	0.998	1.522	53.8°
Sucker&Brauer [72]	0.557	1.076	1.633	51.94°
Son & Hanratty [68]	0.513	0.997	1.51	53.9°
Dröge [23]	0.56	1.02	1.58	53.33°
Meyer et al. [52]	0.52	1.04	1.56	45.4°
present Cartesian	0.562	0.996	1.559	52.90°
present body adjusted	0.525	1.002	1.527	52.23°

Table 5.5.: *Cylinder* Re = 40*, literature values from calculations; [23], [52] immersed interface/boundary methods*

sults of [22]. For the total drag C_d and the friction/pressure contributions (C_{df},C_{dp}) the results show excellent agreement for the whole range of Reynolds numbers.

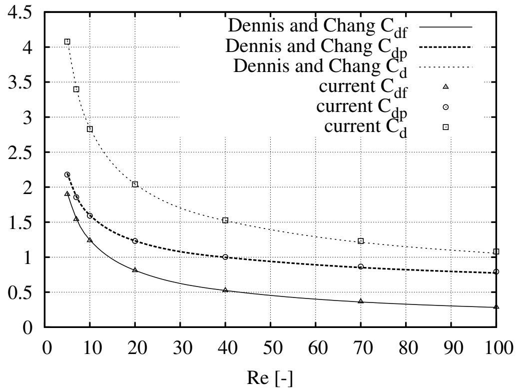

Figure 5.7.: *Cylinder drag - comparison with simulations by [22]*

Conclusion

The first conclusion we can draw from the above study is that both topologies showed similar accuracies. The uncertainty of the total drag coefficient was smaller for the Cartesian topology, while the uncertainty for the separation angle was higher than for the body adjusted topology. To evaluate the results we have to compare the two mesh sizes. The finest Cartesian mesh used 2.4 millions cells[1], while the body adjusted mesh only used 16.384 cells and the last refinement step was solely done through clustering cells close to the immersed boundary. This comparison clearly shows the benefit of using body-adjusted curvilinear grids with the presented configurations.

---

[1] even though this was slightly exaggerated by the rather large middle domain of $4 \cdot 4$

5.2. Airfoil with trailing edge flap - hybrid approach

As we saw in the previous section, full Cartesian grids can become very heavy to compute, since a considerable amount of cells will lie within the body geometry or in regions with small flow gradients. Therefore, using a body adjusted mesh was beneficial. With increasing Reynolds number, the amount of cells inside the body will increase further, since the overall resolution will have to be increased considerably. When generating a mesh for an airfoil with a trailing edge flap, one might use a body-fitted grid for the stationary part and represent only the flap by an immersed boundary. That approach will be called 'hybrid' in the following. The hybrid approach is able to reduce the amount of computational cells inside the body. At the same time it allows to keep the inherent benefits of the body-fitted grid for most of the body geometry (e.g. efficient use of cells in the boundary layer). This section will present a test case for such a hybrid approach and compare it with a standard body-fitted mesh.

5.2.1. Geometry and numerical setup

In the following, results will be presented for a static NACA0015 airfoil at a Reynolds number of Re $= 50,000$. An immersed boundary represents the last 10% of the airfoil (Fig. 5.8) for the hybrid case. The calculations were performed applying the k-ω SST turbulence model. Fig. 5.9 shows the meshes for the fully body-fitted (bf) and the hybrid (ib) approach in the trailing edge region. The body-fitted mesh was a standard C-mesh with $5 \cdot 64^2 = 20,480$ cells. The last 10% of the airfoil geometry were chopped of for the hybrid approach and an extra block was inserted[2]. The cell count was $9 \cdot 64^2 = 36.864$. The immersed flap geometry contains roughly half of all cells inside the trailing edge block of the hybrid grid. These cells can be considered to generate computational overhead, since they do not contribute to the accuracy of the solution. We have to keep in mind that the mesh topologies and cell counts are different.

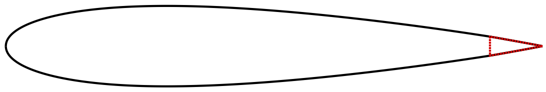

Figure 5.8.: *Geometry of NACA0015 airfoil with a 10% flap represented as an immersed boundary (-)*

5.2.2. Results

In Fig. 5.10 the c_p distributions of both mesh types are plotted for two different angles of attack $\alpha = 1°$ and $\alpha = 5°$. The plots show good agreement, while the suction peak for the $\alpha = 5°$ case is slightly higher for the hybrid approach.
Fig. 5.11 compares the distributions of the velocity component u and the turbulent kinetic energy k along different x-positions. The plots show good agreement for the velocity component u. The turbulent kinetic energy k shows differences in the outer half of the boundary layer. This can be explained by the coarser resolution that was used in this region of the body-fitted mesh. A comparison of the residuals between

---

[2] This also genereated additional blocks above, below and behind.

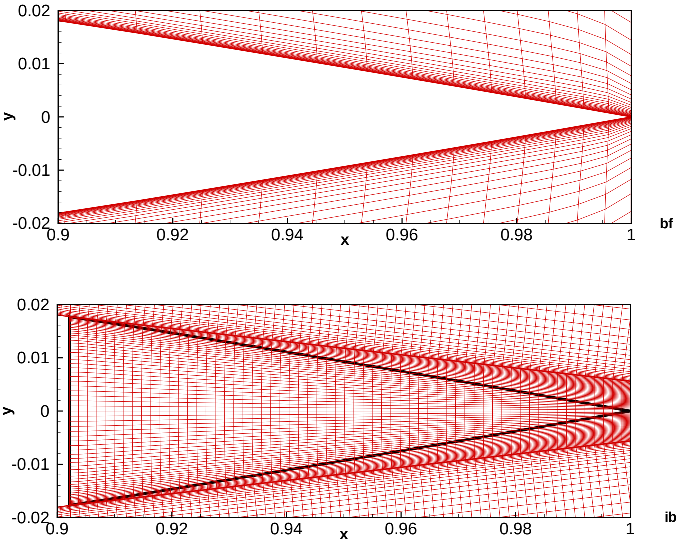

Figure 5.9.: *NACA0015 flap area - mesh comparison between a fully body-fitted grid and the hybrid approach*

the two cases (Fig. 5.12) shows that the hybrid approach reduces the convergence speed per time step. The maximum residual of the turbulent kinetic energy k levels out slightly below 10^{-5}. Tab. 5.6 shows the obtained values of C_l and C_d for the three different angles of attack. At the highest angle of attack $\alpha = 5°$, the lift coefficient is 3.1% and the drag coefficient is 1.7% increased, when comparing with the body-fitted mesh.

	grid	$\alpha = 0°$	$\alpha = 1°$	$\alpha = 5°$
C_l	bf	-0.0000	0.0903	0.4472
	ib	-0.0000	0.0933	0.4615
C_d	bf	0.0192	0.0194	0.0229
	ib	0.0203	0.0204	0.0233

Table 5.6.: *Lift and drag coefficient for body-fitted and hybrid grid*

5.2.3. Conclusion

The two different meshing approaches generated similar results for a relatively low Reynolds number of Re $= 50,000$. A fair comparison is hard to obtain, since the difference in the meshing approach always generates differences in cell count and cell distributions. Still, we can conclude that the hybrid approach is capable of representing the flow around the whole airfoil for this first test case. Now, the challenge is to prove the concept for higher Reynolds numbers and moving inflow conditions as well as moving flap geometries.

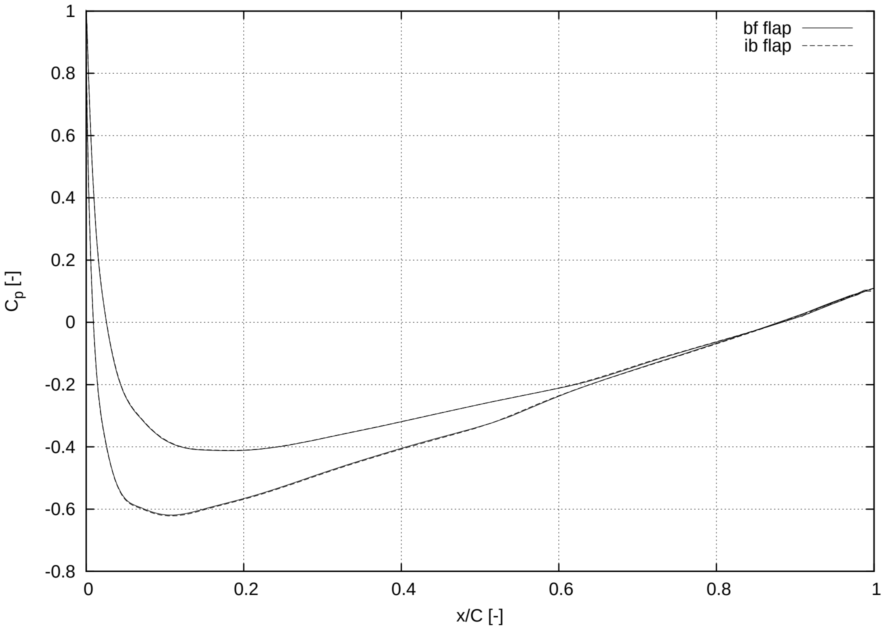

(a) $\alpha = 1°$

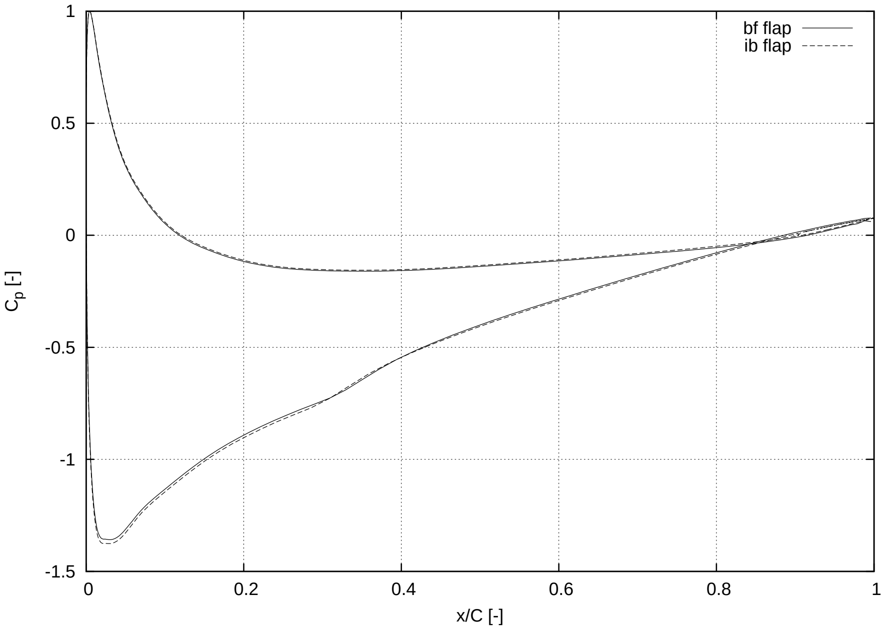

(b) $\alpha = 5°$

Figure 5.10.: *Pressure distribution at* $\mathrm{Re} = 50,000$

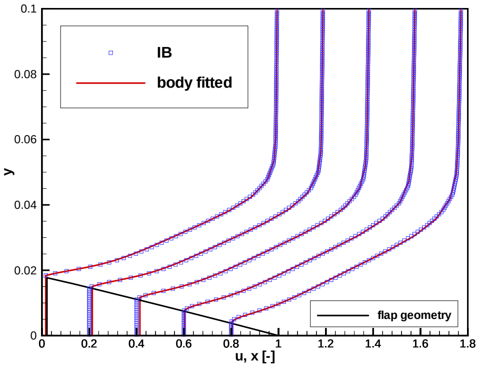

(a) velocity u

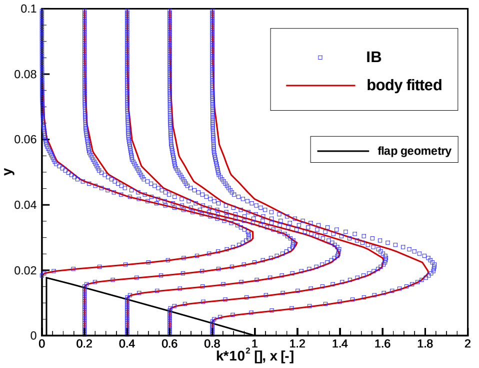

(b) turbulent kinetic energy k

Figure 5.11.: *Distributions at different cuts along the flap geometry*

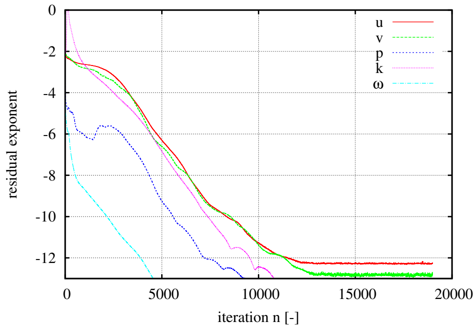

(a) bf

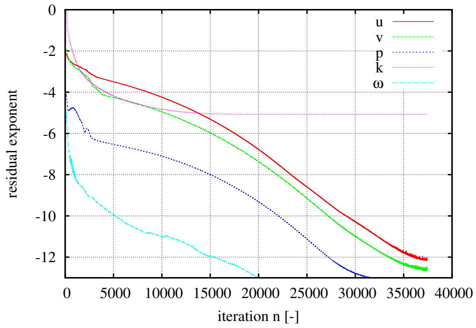

(b) ib

Figure 5.12.: *Residuals for* $\alpha = 0°$, $\mathrm{Re} = 50,000$

5.3. Comparison with wind tunnel experiments

In this section, results from the two-dimensional IB hybrid method will be compared with wind tunnel experiments. In [40], the authors present measurements for a symmetrical airfoil (NACA0012) equipped with a 20% movable hinged flap (see Fig. 5.13). In addition to the rotation of the flap, the airfoil was also able to oscillate around an axis at 35% chord. The wind tunnel was of the blow down type with partial recirculation and perforated top and bottom walls. To get the airfoil pressure distribution and to integrate the lift coefficient C_l pressure tab measurements in the mid-span region were used.

The flow conditions are $\mathrm{Re} = 1.63 \cdot 10^6$ ($\mathrm{Ma} = 0.4$, compressible regime) and results for different phase angles Φ between the pitching motion and the flap deflection are presented. The reduced frequency of the pitching motion is $k_\alpha = 0.021$, while the flap deflection frequency was $k_\delta = 2k_\alpha = 0.042$. The experiments were conducted at a center angle of attack $\alpha_0 = 4°$ and center flap deflection $\delta_0 = 0°$. The maximum deflections were $\alpha_m = 6°$ and $\delta_m = 5.4°$.

$$\alpha(t) = \alpha_0 + \alpha_m \cdot \sin\left(\frac{2 \cdot k_\alpha \cdot U}{C} \cdot t\right) \tag{5.9}$$

$$\delta(t) = \delta_0 + \delta_m \cdot \sin\left(\frac{2 \cdot k_\delta \cdot U}{C} \cdot t - \Phi\right) \tag{5.10}$$

The rest of this section will first present the numerical setup, including results of lift loops for an oscillating inflow and for the airfoil at fixed angle of attack but with an oscillating flap. Afterwards, the measurements from [40] will be compared with 2D hybrid simulations of the airfoil with both oscillating angle of attack and oscillating flap deflection.

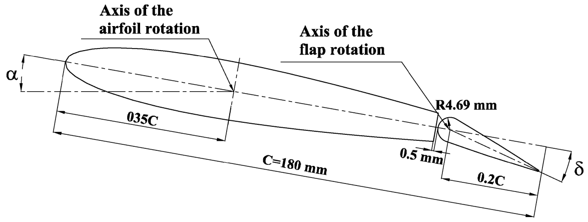

Figure 5.13.: *Experimental setup of Krzysiak and Narkiewicz [40]*

5.3.1. Geometry and numerical setup

The 2D calculations were performed using the hybrid approach. The wind tunnel geometry was not modeled. The flow domain was a disc of radius $21C$ with free stream and outlet conditions applied to the domain boundaries. The moving flap was modeled as an immersed boundary. An overview of the mesh in the airfoil region can be found in Fig. 5.14. Point R denotes the center point of the reference frame rotation at 35% chord. All calculations were performed at the same Reynolds number as the experiment $\mathrm{Re} = 1.63 \cdot 10^6$. The non-dimensional time step was set to $\Delta t^* = 0.001$. The mesh consisted of a total of $35 \cdot 64^2 = 143.360$ cells.

Rotating frame of reference

Instead of pitching the airfoil in the inertial coordinate system, the flow is solved in a rotating frame of reference by introducing acceleration terms in the momentum

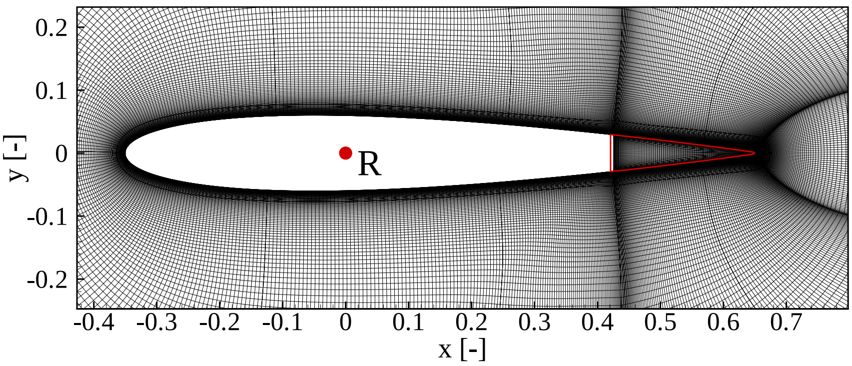

Figure 5.14.: *Grid configuration for the NACA0015,* Re $= 1.63 \cdot 10^6$*; immersed boundary (-), point of rotation R*

equations. The absolute acceleration a of any point (position vector $\mathbf{r}$) in the rotating frame of reference (e.g. [83]) was defined as follows.

$$\mathbf{a} = \frac{\mathrm{d}^2\mathbf{R}}{\mathrm{d}t^2} + \frac{\mathrm{d}\boldsymbol{\Omega}}{\mathrm{d}t} \times \mathbf{r} + \boldsymbol{\Omega} \times (\boldsymbol{\Omega} \times \mathbf{r}\ ) + \frac{\mathrm{d}\mathbf{V}}{\mathrm{d}t} + 2 \cdot \boldsymbol{\Omega} \times \mathbf{V} \tag{5.11}$$

where $\mathbf{V}$ is the non-inertial velocity vector, $\mathbf{R}$ the displacement vector between the two systems and $\boldsymbol{\Omega}$ is the angular velocity vector of the frame. In the following only the rotation of the reference frame around the rotation point will be considered. No translatoric contributions were included.

Fig. 5.15 shows an example of the oscillating reference frame inflow and the resulting lift coefficient on the NACA0012 airfoil with fixed flap. The reduced frequency was low ($k = 0.01$) which resulted in a low phase lag between the angle of attack and the lift coefficient. In Fig. 5.16 the lift loops $C_l(\alpha)$ for two cases $k = 0.01$ and $k = 0.1$ are presented. Both loops are counter-clockwise, which is the expected behavior for attached flow. The common clockwise loops are only seen, when the airfoil is experiencing dynamic stall (e.g. [76]). We see the known effect that higher reduced frequencies decrease the lift amplitude and widen the lift loop. For both cases the drag loops are plotted in Fig. 5.17. The drag loops show the expected eight-shape

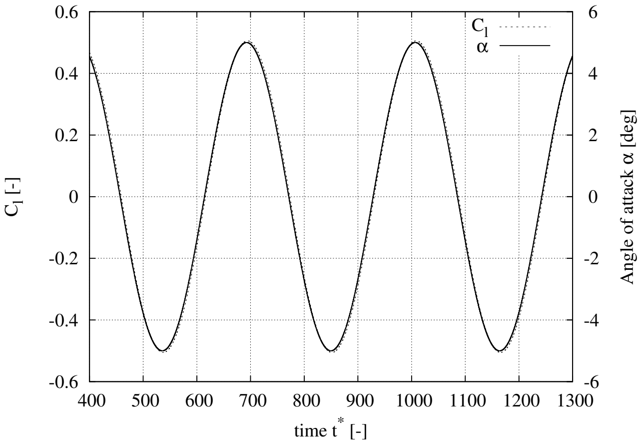

Figure 5.15.: *Lift coefficient C_l and angle of attack α over non-dimensional time t*

behavior for a symmetrical airfoil oscillating around zero angle of attack. For the higher reduced frequency $k = 0.1$ the amplitude of the drag coefficient is increased.

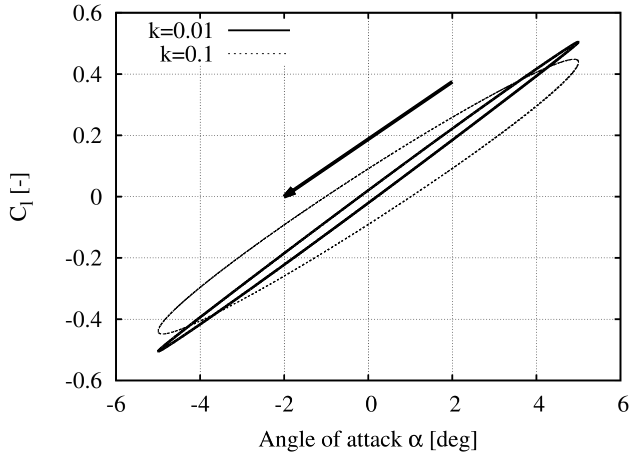

Figure 5.16.: *Lift loops for two different reduced frequencies k, rotation in counter-clockwise direction*

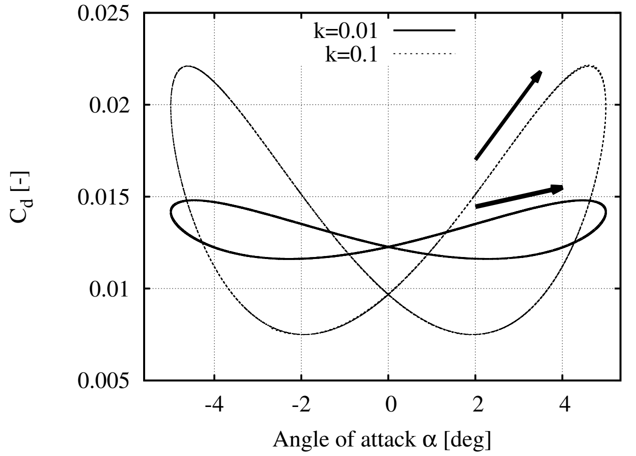

Figure 5.17.: *Drag loops for two different reduced frequencies k*

Moving flap

Before moving on to the comparison with the measurements, the hybrid method shall be also presented for a single oscillating flap deflection in steady inflow conditions. The resulting unsteady lift coefficient for a flap deflection amplitude of $\delta_m = 5°$ at a low reduced frequency of $k = 0.01$ and $\alpha_c = 5°$ is presented in Fig. 5.18. The resulting lift coefficient amplitude of ≈ 0.2 agrees well with experiments[3]. The four snapshots in Fig. 5.19 present the vorticity field and isobars phase-steps of $\Delta\Phi = \pi/2$, starting with the fully upwards deflected flap ($\delta = -5°$). The flap location can easily be identified by the vorticity contours. It is worth noting the different isobars in Fig. 5.19(b) and Fig. 5.19(d). Even though the geometry definition of the flap is the same for both snapshots, the isobars are not. The difference clearly shows the lagging flow response.

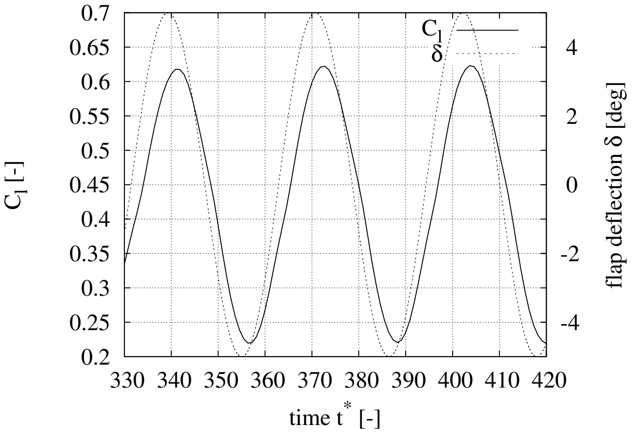

Figure 5.18.: *Moving flap at $k = 0.01$, ±5°*

---

[3] see static flap efficiencies compiled by [4] repeated in the appendix Fig. 2.3

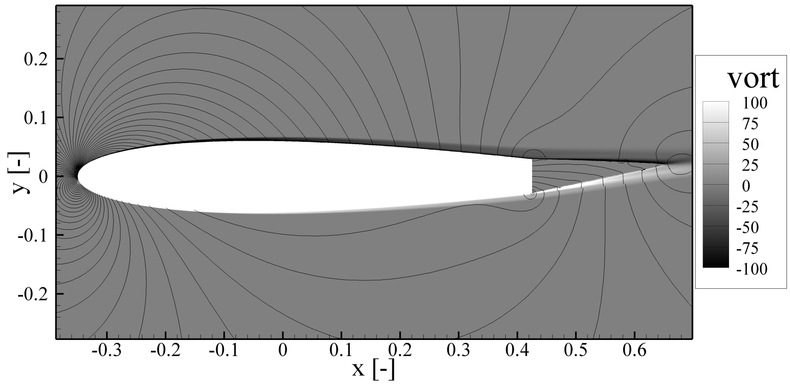

(a) $\delta = -5°$, $\Phi = \Phi_0 + 0$

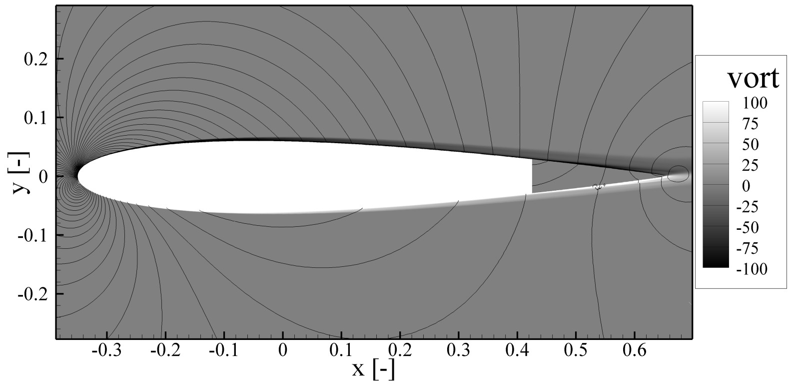

(b) $\delta = 0°$, $\Phi = \Phi_0 + \pi/2$

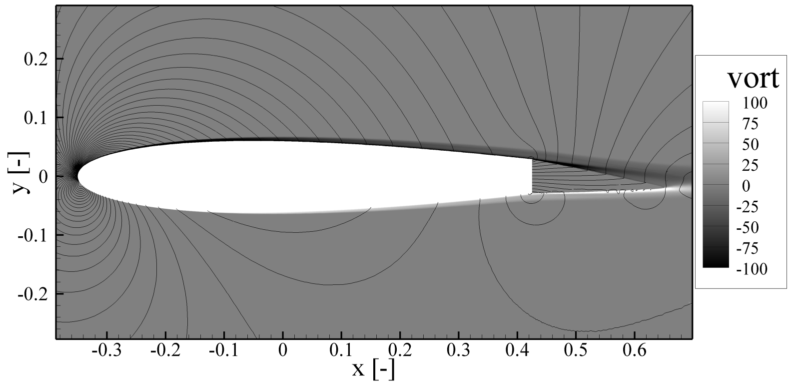

(c) $\delta = +5°$, $\Phi = \Phi_0 + \pi$

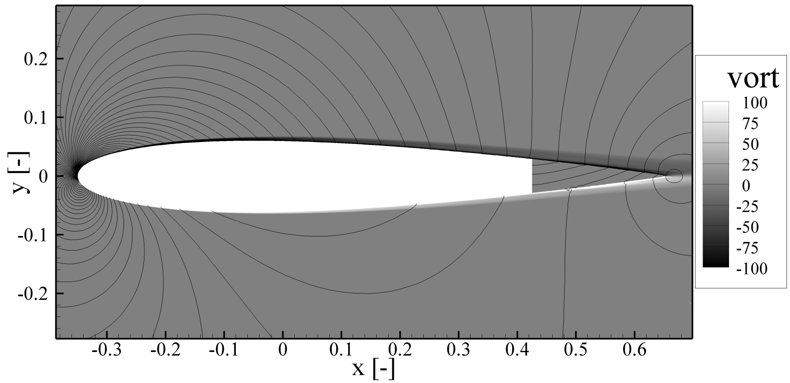

(d) $\delta = 0°$, $\Phi = \Phi_0 + 3/2 \cdot \pi$

Figure 5.19.: *Moving flap, vorticity contours and isobars*

5.3.2. Different flap geometries

Multiple ways exist to calculate the new flap geometry for a given flap deflection. Here, the displacements (Δx_P, Δy_P) for every trailing edge marker point will be calculated at every time step, based on a rigid rotation of the flap chord around the defined hinge point H. The displacement of the trailing edge is distributed along the flap according to the expression 5.13, where the exponent *sc* is a shape parameter of the deflection. Fig. 5.20 depicts the geometric difference between a plain flap (flap deflection exponent sc = 1) and a smoothly curved flap (sc = 2).
The flap deflection δ is defined as the negative angle between the line S (H − TE) and the original chord line.

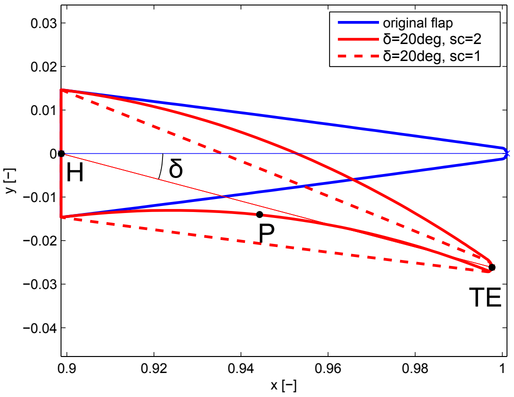

Figure 5.20.: *Geometry for different flap deflection exponents* sc

$$\begin{aligned} \Delta x_P &= S \cdot \cos(\delta) \left[(x_P - x_H)/(x_{TE} - x_H)\right]^{\mathrm{sc}} \\ \Delta y_P &= S \cdot \sin(\delta) \left[(y_P - y_H)/(y_{TE} - y_H)\right]^{\mathrm{sc}} \end{aligned} \tag{5.12}$$

Contrary to the original experiment, where the flap was rotated around its hinge (0.8,0.0), here the above equation with sc = 1 is used and the hinge point is moved upstream to coincide with the blunt airfoil edge. Therefore, the hinged flap is 2.87% shorter than the one used in the calculations (see Fig. 5.21(a)). The difference between both shapes for one of the test cases below shows only very little difference Fig. 5.21(b). Therefore, the use of the closed geometry is appropriate.

5.3.3. Combined airfoil and flap oscillation

In this section the results from the wind tunnel experiment [40] for different phase lags Φ between the pitching motion and the flap deflection are compared to the 2D simulations. The oscillations in the simulations were set up according to equations 5.9 and 5.10. Fig. 5.22 plots both the simulation results and the experimental data for the lift coefficient at different phase angles Φ. Additionally, the actual obtained values for angle of attack and flap deflection from the experiment (exp.) are plotted together with their prescribed values. We can see differences in prescribed and obtained angle of attack of up to $\approx 1.5°$ when downward sloping. The biggest deviations of the flap deflection from the prescribed values is $\approx 1°$.
The lift loops no longer have an O-shape as for the single oscillatory inflow, but are now 8-shaped. The new shape is the effect of simultaneous moving the flap at $k_\delta = 2k_\alpha$, where the phase angle Φ between the two oscillations determines the

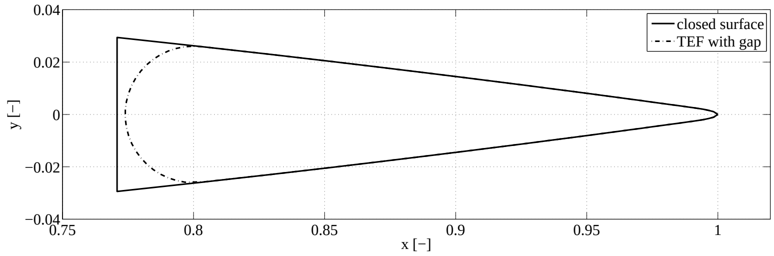

.

(a) Different flap geometries

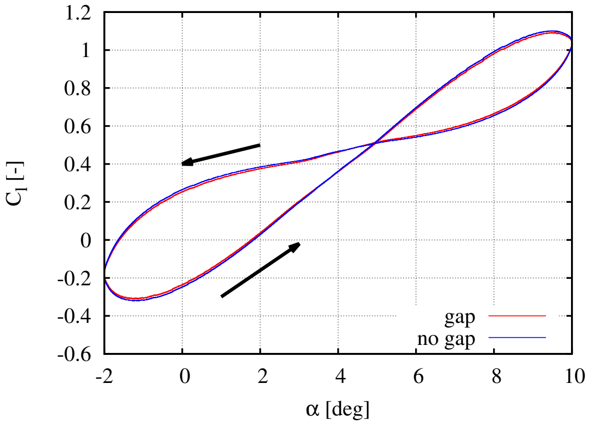

(b) result for $\Phi = 357°$

Figure 5.21.: *Results for different flap geometries*

final shape of the loop. In Fig. 5.22(d), we see that the α-peaks coincide with the minimum flap deflection angles, which leads to the lowest minimum and maximum C_l for the $\Phi = 298°$ case Fig. 5.22(c).

In general, the simulations capture the shape of the lift coefficient loops well. They do appear to be more bellied, which might be due to the larger flow domain in the simulations. The lift coefficient amplitude is overpredicted for all three cases. The knot of the 8-loop is shifted to $\approx 1°$ smaller angles of attack for the first two presented cases ($\Phi = 148°$ and $\Phi = 298°$).

Fig. 5.23 shows two cases where the center angle of attack has been increased to $\alpha_c = 10°$. Now, the prescribed angle of attack range is $4° \leq \alpha \leq 16°$. The rest of the setup is unchanged. The experimental pitching mechanism was not able to reach the full oscillation range. We see that the steep drop in lift at high angles of attack is not present in the simulations.

In Fig. 5.22 and Fig. 5.23 the numerical results from a thin airfoil model applied in [40][4] are plotted where available. For the cases at $\alpha_c = 4°$, the hybrid IB method clearly outperforms the thin airfoil code, which seems to overestimate the effect of the flap by a large factor. Both cases at $\alpha_c = 10°$ are not predicted well by both models. For the two dimensional free stream calculations, the high angle of attack cases are still challenging. A comparison with 3D wind tunnel data is not straightforward due to distinct three dimensional effects like tunnel blockage[5] and wall interaction which can significantly change the airfoil's stall behavior.

Nevertheless, we can conclude that the hybrid IB method is a suitable tool for calculations of pitching airfoils with moving trailing edge flaps and extends the current modeling capabilities.

---

[4] the model - named 'theoretical 2' in [40] - was fed the values of angles of attack and flap deflections from the experimental data

[5] The wind tunnel section was $0.6\text{m} \cdot 0.6\text{m}$, which leads to a 8.3% geometrical blockage at $\alpha = 16°$ and $\delta = 0$

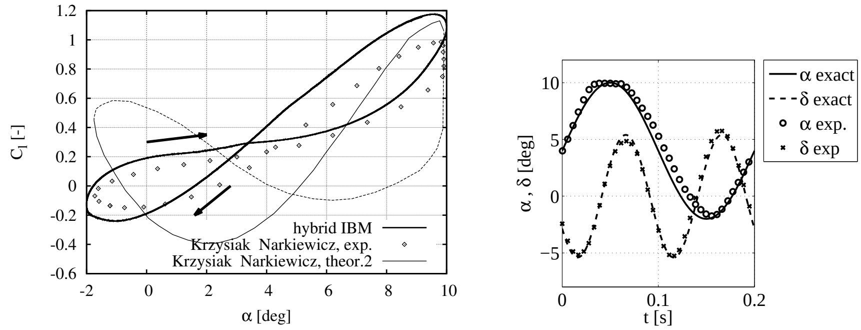

(a) $\Phi = 148°$ (b) $\Phi = 148°$

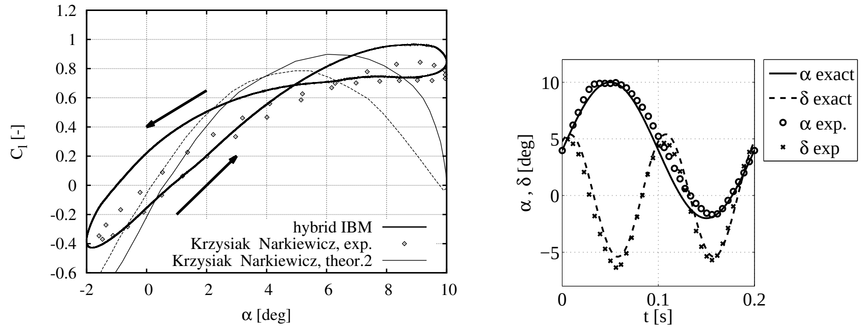

(c) $\Phi = 298°$ (d) $\Phi = 298°$

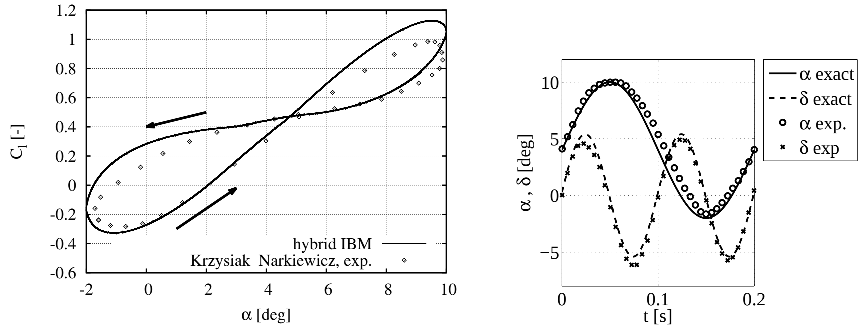

(e) $\Phi = 357°$, 'theor.2' not reported in [40] (f) $\Phi = 357°$

Figure 5.22.: *$C_l(\alpha)$ for different phase angles Φ at $\alpha_0 = 4°$*

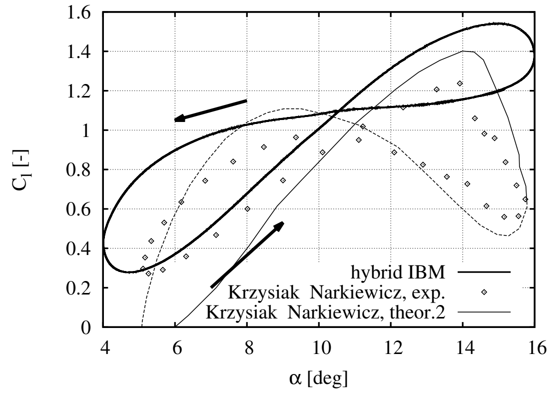

(a) $\Phi = 343°$

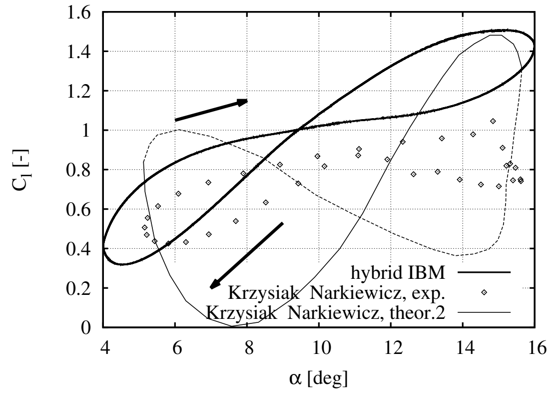

(b) $\Phi = 177°$

Figure 5.23.: *$C_l(\alpha)$ for different phase angles Φ, $\alpha_0 = 10°$*

5.4. Comparison of 2D and 3D solutions

In this section, we will compare a two dimensional and a three dimensional solution of flow around an airfoil modeled with the hybrid approach.

5.4.1. Geometry and numerical setup

The two dimensional mesh was the same as in the comparison with the wind tunnel data in section 5.3. That mesh was extruded 0.5 chord lengths in span-wise direction (Fig. 5.24)[6]. The span was discretized into 32 cells that were uniformly distributed. The total number of cells was $140 \cdot 32^3 = 4.587.520$. Periodic boundary condition were assigned to the span-wise sidewalls. The flap geometry was defined on two cuts at minimum and maximum span. The Reynolds number of the simulations was $\mathrm{Re} = 1.63 \cdot 10^6$ and the angle of attack was $\alpha = 5°$. The non-dimensional time step was $t^* = 0.001$.

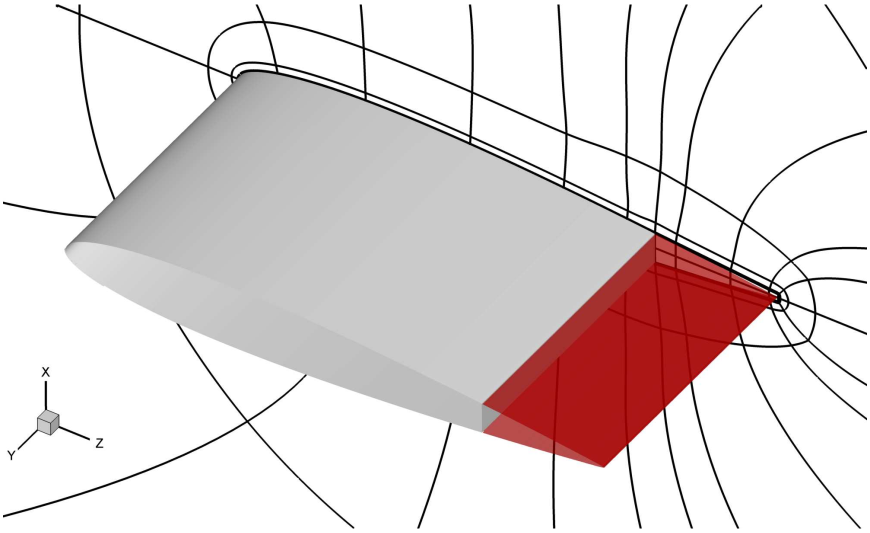

Figure 5.24.: *3D geometry extended from 2D mesh*

5.4.2. Results

Fig. 5.25 shows iso-levels of the velocity magnitude. The plots shows values on slice at $y = 0.25$ for the three dimensional case. In general the plots show good agreement. Slight differences can bee seen in the wake and esp. in the outer part of the flow field behind half-chord.
To allow us to have a closer look at the flow, Fig. 5.26 shows four plots with different flow variables for a line ((0.55,0.2) to (0.55,-0.2)) that cuts through the immersed boundary flap. The chord wise velocity u agrees well between both cases. One can recognize the boundary layer and the drop to zero for the region inside the flap. When looking at the velocity component v we see that the peaks deviate by around 5% from the 2D case. The turbulent kinetic energy k shows much higher peak values. On the suction side, the maximum k increases about 30% and on the pressure side it increases about 50%. For the specific dissipation ω, the curve shape is less affected, but the suction side peak is reduced by more than $\approx 50\%$ for the 3D case (note the logarithmic scale).

---

[6] Note the changed coordinate system, this section will use the 2D definition when comparing the two cases.

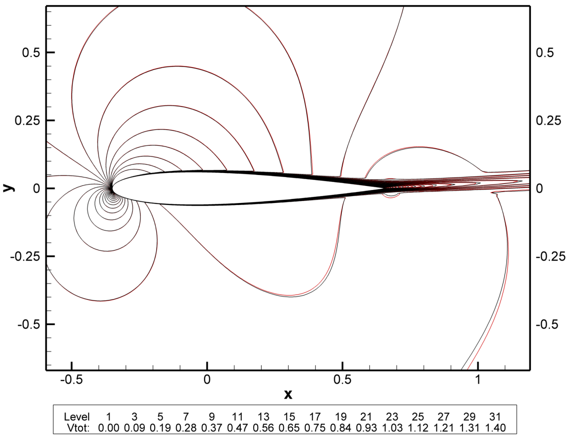

Figure 5.25.: *Comparison of velocities magnitudes for a 2D (black) and a 3D case (red) at* $\alpha = 5°$*,* $y = 0.25$

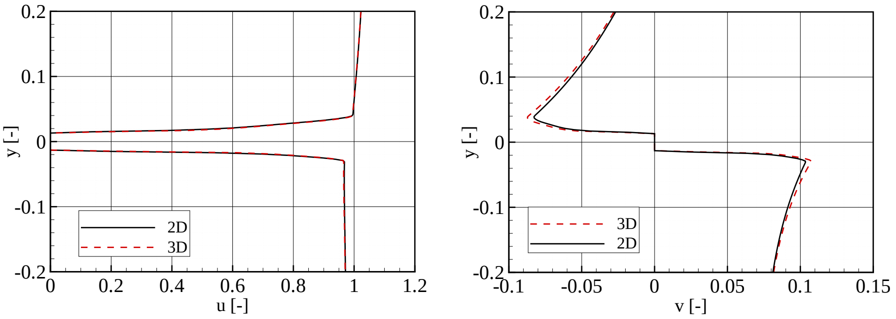

(a) u velocity

(b) v velocity

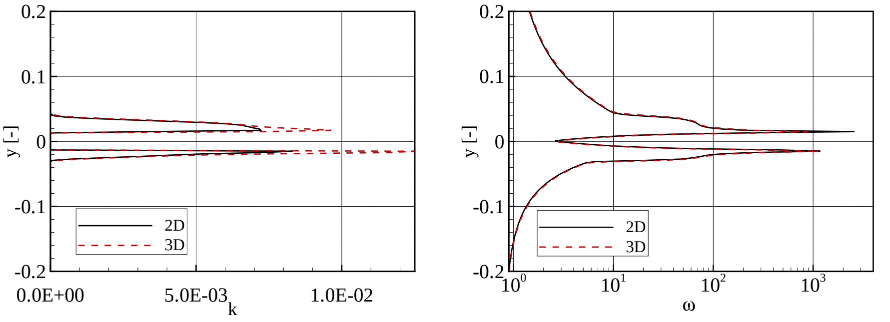

(c) turbulent kinetic energy k

(d) specific dissipation ω

Figure 5.26.: *Comparison of scalars for a 2D (black) and 3D case (red) at* $\alpha = 5°$*, line ((0.55,0.2) to (0.55,-0.2)), 3D span-wise coordinate* $y = 0.25$

5.4.3. Conclusion

The general agreement between the flow fields of the 2D and the 3D case was fair. The cause of the slight difference between the peak values of the u, k and ω values for both cases is not obvious. The main part of the airfoil was not affected by these differences, however. The overall flow field was represented well and we can conclude that the 3D implementation of the method was able to represent the trailing edge geometry.

At this point, it is interesting to stop for a moment and evaluate the extra computational effort caused by the immersed boundary method for both a static and a moving flap case. Tab. 5.7 presents percentages of the overall computational time consumed by the IB method and its subcomponents. For the 2D case, most of the time is spent on the velocity interpolation (≈ 40%) and the calculation of the force integration on the flap (≈ 16%). While the cell tagging only has a small contribution, the calculation of the normal distance increases for the moving flap to 4.3% of total calculation time. Only a small difference in total computional time exists between the static and the moving flap case. For the 3D case, the added computing time amounts to only 0.9% for a static flap, while it amounts to 71.4% for a moving flap. This huge difference is due to two factors. Firstly, the increased time consumption of the basic solver in 3D reduces the IB contribution to the total calculation time for the static case significantly. Secondly, the calculation of normal distances and integrated forces becomes increasingly expensive.

IBM	vel.interp.	force integr.	normal dist.	cell tagging	total IB
static flap 2D	39.7%	11.8%	0.7%	0.01%	56.6%
moving flap 2D	40.1%	10.3%	4.3%	0.11%	60.8%
static flap 3D	0.16%	0.2%	0.07%	0.01%	0.9%
moving flap 3D	1.92%	16.5%	34.31%	5.52%	71.4%

Table 5.7.: *Fractions of total computational time for representative configurations*

5.5. Conclusion of validation

For the cylinder cases, both the Cartesian and the body-adjusted topology showed similar accuracies. The uncertainty of the total drag coefficient was smaller for the Cartesian topology, while the uncertainty for the separation angle was higher. The finest Cartesian mesh used 2.4 millions cells while the body adjusted mesh used 16.384 cells and the last refinement step was solely done through clustering cells close to the immersed boundary. The comparison showed the benefit of using body-adjusted curvilinear grids with the presented configurations.
For the airfoil with a fixed trailing edge flap, two different meshing approaches (full body-fitted and IB) generated similar results for a relatively low Reynolds number of $\mathrm{Re} = 50,000$. A fair comparison was hard to obtain, since the differences between the meshing approaches always lead to differences in cell counts and cell distributions. Still, we can conclude that the hybrid approach is capable of representing the flow around the whole airfoil for this case. To prove the concept for high Reynolds numbers and moving inflow conditions as well as moving flap geometries computational, simulation results were compared to published wind tunnel data. It was concluded that the hybrid IB method is a suitable tool for calculations of pitching airfoils with moving trailing edge flaps. The method extends the modeling capabilities of e.g. thin airfoil codes.
The agreement between the flow fields of a 2D and a 3D hybrid case at high Reynolds number was fair. The main part of the airfoil was not affected by differences close to the immersed boundary. The overall flow field was represented well and the 3D implementation of the IB method was able to represent the trailing edge geometry.
Finally the fraction of total computing time that the IB method consumed was evaluated. The 2D cases used around 60% of the total computing, while in the 3D case, the computing time amounted to only 0.9% for a static flap and to 71.4% for a moving flap.

Part III.

Applications

This second part of the thesis presents applications of the hybrid immersed boundary method. Two variants of local load alleviation control methods are presented. The first controller will be based on the lift coefficient as sensor input and uses a trailing edge flap that is divided in two single independent portions. The second controller will use the unsteady hinge moment acting on the moving flap as a sensor input to alleviate changes in lift.

Three applications of the hybrid IB method to 3D airfoils section will be demonstrated. The ability of the method to model a gap between two flap sections will be shown for a low Reynolds case. A similar configuration without gap will be used to demonstrate a first control setup which uses two independent flaps. Finally, a high Reynolds configuration will be presented where a flap deflected over 50% of the span generates a pair of distinct trailing vortices.

6. Divided flap action

6.1. Motivation

Wind turbine rotors are subject to a variety of unsteady loads. In general, these unsteady loads can be separated into two frequency domains:

- **Low frequency** loads originate among others from wind shear, yaw error, tower shadow, partial wake situation or rotor imbalance. These loads appear in a narrow band close to the rotor frequency (1P and higher harmonics).
- **High frequency**, highly stochastic loads originate mainly from the turbulent wind and vibrations of the wind turbine blades and other components (e.g. drive train).

The very low ($\ll$1P) frequencies can easily be mitigated by the hydraulic or electric blade pitch system. The smart rotor offers a solution to alleviate higher frequencies loads at 1P and above.

In smart rotor research, most of the studies on actuator systems have been focused either on low frequency actuators (e.g. shape memory alloys) or high frequency actuators such as piezo-electric benders. Usually, there is an inconvenient trade-off between fast actuation and total stroke or total force achievable. The faster an actuator moves, the less force it is able to create.

An idea to counter this drawback is to combine two different actuator species (or embodiments), one for each of the specific load frequency spectra [13]. Possible realizations could be a fully integrated flap module with both actuators or distributed fast and slowly actuated surfaces along the blade (see Fig. 6.1). The latter approach would for instance place the smaller faster actuators in the outer region of the blade, where the available space is very limited.

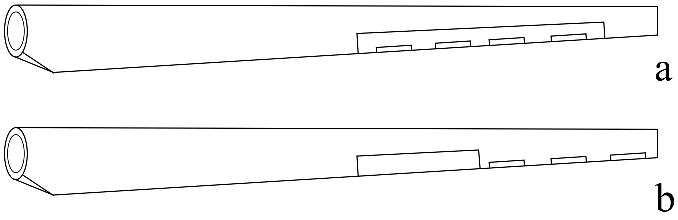

Figure 6.1.: *Possible actuator setups along the blade span*

Fig. 6.2 presents one possible example of the integrated approach, where an airfoil is equipped with a divided trailing edge flap, operated by two separate actuators. The full flap is separated into one slow moving (possibly morphing) base flap and an additional faster moving end part. This combined system approach would allow each of the actuator system to operate within their durability region. Thereby, actuator wear and tear can potentially be reduced, while it would still be possible to alleviate loads in a broad frequency range. This benefit comes of course at the cost of having to design, manufacture and maintain two different systems inside the constrained space of a blade trailing edge region. These additional costs have to be weighted against the benefits from actuators reliability and control authority.

The idea of dividing the desired flap deflection into two separate deflections will be investigated in the next sections from an aerodynamic point of view.

After introducing a baseline control in section 6.2 for a single full flap deflection case, section 6.3 will study a divided flap concept for different maximum deflections and deflection speeds of an additional fast moving flap part.

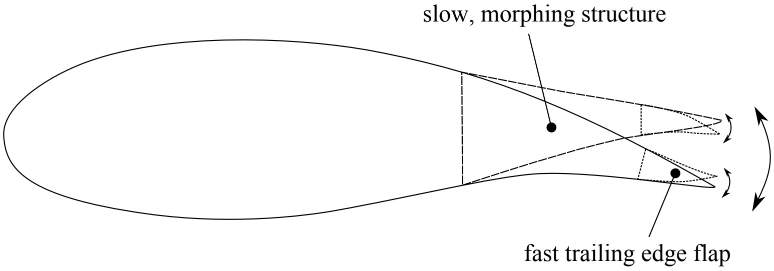

Figure 6.2.: *Sketch of a possible configuration for divided trailing edge flap actuation*

6.2. Lift based control for a single flap

A controller based on the instantaneous lift coefficient C_l will be used to generate a set of baseline results. This simple control approach is considered appropriate, since the study focuses on the actuator capabilities. It shall be noted though, that on a real blade, the airfoil section's current C_l is usually unknown and the sectional load has to be derived differently.

6.2.1. Controller

A simple PID controller was based on the difference between the instantaneous and the zero angle of attack lift coefficient C_l^0. Multiplied with k_{C_l}, this difference generated a target flap deflection for load alleviation, yielding the control error e:

$$e = \delta - \left(-k_{C_l} \cdot \left(C_l - C_l^0\right)\right) \tag{6.1}$$

This control error was then fed into a PID-control loop, which then generated a new flap deflection speed $\widetilde{\omega_1}$. This deflection speed was mixed[1] into the last time step's value ω_1 by r.

$$\widetilde{\omega_1} = (1 - r) \cdot \omega_1 + r \cdot \left(\left(P \cdot e + I \cdot \int e + D \cdot \frac{\Delta e}{\Delta t} \right) / \left(\delta_{m,1}\right) \cdot \omega_{1_m} \right) \tag{6.2}$$

P, I and D denote the proportional, integral and differential gain. Integral anti-windup was added to the base controller. The anti-windup stopped further error integration when the actuator was saturated. Thereby, it prevented the PID controller from getting winded up (or 'stuck'), when the control error grew beyond what the actuator was able to alleviate. The maximum flap deflection was limited to $\delta_{m,1} = \pm 4^\circ$ and the flap shape exponent was $\mathrm{sc} = 2$, resulting in a smoothly curved geometry. The respective PID gains were found through parameter sweeps[2].

6.2.2. Geometry and numerical setup

The airfoil geometry used was a NACA63-200 airfoil with a slightly modified trailing edge and relative thickness of $t = 16.6\%$. The flap length was 16% of the chord. A hybrid approach was used when generating the 2D computational domain (Fig. 6.3). The stationary part of the airfoil was represented by a body conformal C-like grid. An immersed boundary represented the trailing edge flap, which moved inside a block attached to the end of the cut airfoil body. The trailing edge was blunt with a

---

[1] equivalent to a low-pass filter. Standard value through out this work was $r = 0.1$.

[2] $(P = 1,\ I = -0.025,\ D = 0)$

thickness of 0.2% chord, since the immersed boundary method needed at least one computational cell inside the body geometry. The total number of grid points was $64 \cdot 64 \cdot 9 = 36.864$. The first cell height above the wall was chosen to satisfy, that the dimensionless wall distance y^+ was smaller than one. A similar grid spacing was used close to the immersed boundary.

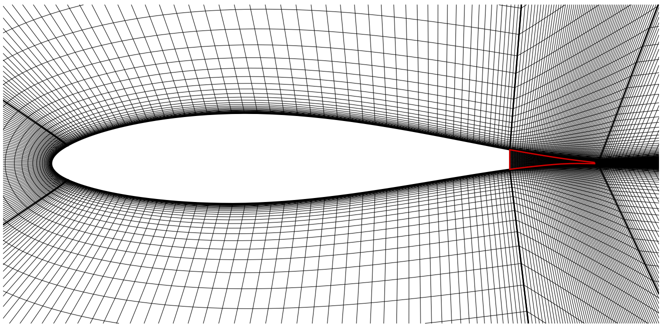

Figure 6.3.: *Computational grid for the NACA 63-200, t = 0.166, – immersed boundary*

All calculations were performed at a Reynolds number of $\mathrm{Re} = 10^6$. The distance of the airfoil to the free stream boundaries was 11 chord lengths[3]. The disturbances were introduces by applying a rotating frame of reference (section 5.3.1). The simulations calculated 120.000 non-dimensional time steps ($\Delta t^* = 0.002$), starting from a steady solution. For post-processing the first 5% of the output were dropped, resulting in 7.25 periods of the pitch oscillation for a reduced frequency of $k = 0.1$.

6.2.3. Results

The variance σ^2 of the lift coefficient can serve as an estimate of blade fatigue loads.

$$\sigma^2(X) = \overline{(X - \overline{X})^2} \tag{6.3}$$

Eqn. 6.3 defines the variance for a variable X. The bar denotes the expected value. The variable is dropped in the further notation, since we solely use the lift coefficient C_l. The reduction ρ was defined with the ratio between the variance σ^2 of C_l for an uncontrolled reference case σ^2_{ref} and the result with an activated control (eqn. 6.4).

$$\rho = 1 - \frac{\sigma^2}{\sigma^2_{ref}} \tag{6.4}$$

In Fig. 6.4 a sweep for the gain k_{C_l} is shown. A value of $k_{C_l} = 200$ was used in the following[4].

Fig. 6.5 presents a set of reductions achieved over different maximum actuator speeds ω_m for three flow conditions of pitch amplitude Φ and reduced frequency k. Comparing the two cases for a pitch amplitude of 1°, there is only little difference between the curves above $\omega_m = 0.01$. The reduction is up to 94%. Below $\omega_m = 0.01$, for the faster oscillation of $k = 0.1$ the achievable reductions drop significantly. For the slower oscillation of $k = 0.033$, the C_l variance can still be reduced to about 70% at an actuator speed of $\omega_m = 0.02$ before the steep drop in reduction is seen.

---

[3] This is a rather small distance to the domain boundary, but for the demonstration of a controller it is considered to be sufficient.

[4] This is a rather high value, only possible due to the sinusoidal inflow. With a more random inflow, the parameter's value might have to be reduced considerably.

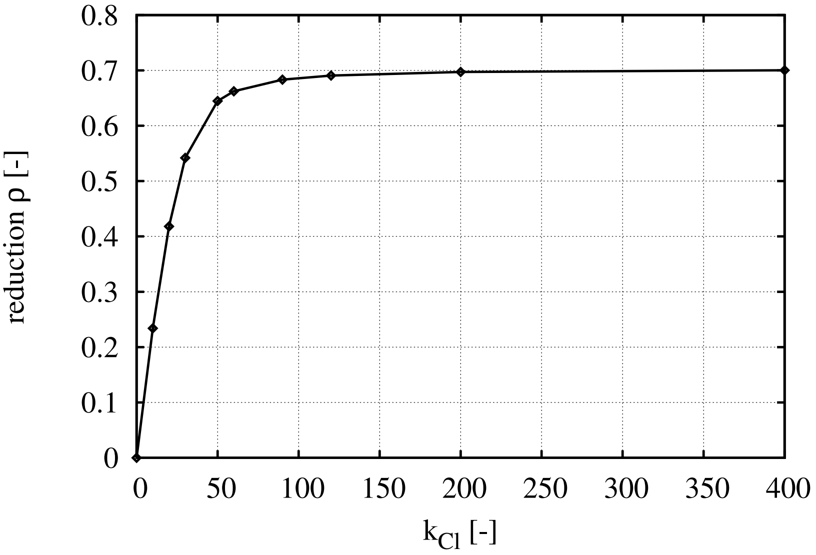

Figure 6.4.: *Lift based control, reduction ρ over gain k_{C_l}*

For the larger pitch amplitude of 2°, in general lower reductions of about 74% could be achieved, with a less severe drop for smaller actuation speeds than $\omega_m = 0.02$.

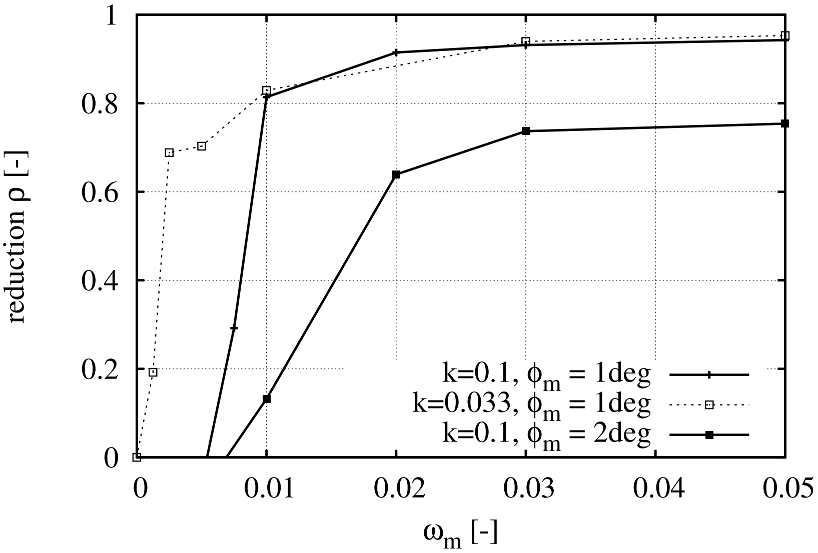

Figure 6.5.: *Reduction ρ over maximum flap deflection speed ω_m for different reduced frequencies k and pitch amplitudes Φ*

6.3. Lift based control for a divided flap

Now, the influence of an additional second flap portion will be investigated. The second flap deflection is added on top of the full flap for the smaller last part of the airfoil. The computational setup is unchanged.

6.3.1. Flap geometry

The flap lengths are $E_1 = 0.16$ for the main flap and $E_2 = 0.048$ for the additional flap. The flap geometry scaling factors were $sc = 1$ (plain/rigid) for both flaps. The flap angles are defined according to Fig. 6.6(a). Since we are investigating a cambered airfoil, the "zero" angles $\delta^0_{1/2}$ become important, when applying the deflections. For the main flap, it is defined as the angle between the x-axis and the line connecting the two hinge points P_{H1} and P_{H2}. For the second flap δ^0_2 is defined as the angle between the extension of the main flap and the line defined by P_{H2} and the trailing edge.

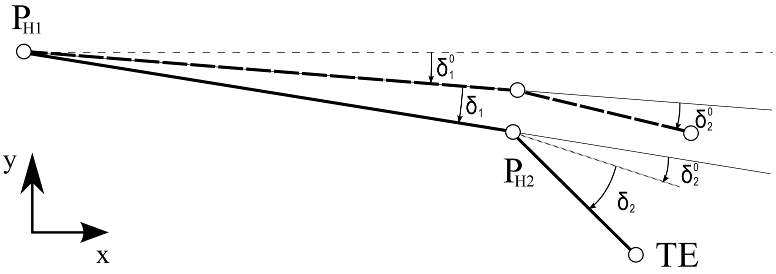

(a) Definition of angles for the divided flap, - - undeflected, - deflected

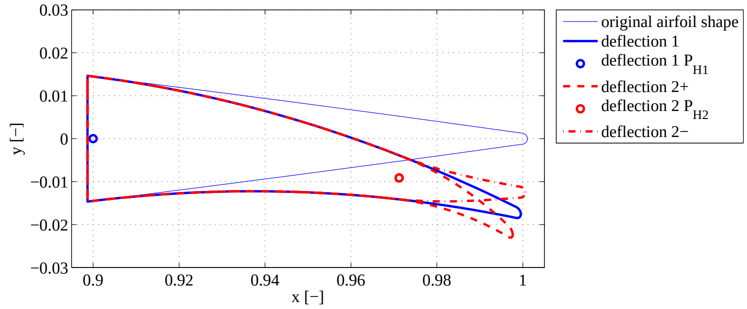

(b) Example geometry of a divided flap

Figure 6.6.: *Implementation of geometry changes for divisional flap action*

6.3.2. Controller

The controller for the divided flap is analogue to the one used above for a single flap. Now, we extend to two $i = [1, 2]$ flaps, which gives the control errors as

$$e_i = \delta_i - \left(-k_{C_l i} \cdot \left(C_l - C_l^0\right)\right) \tag{6.5}$$

The errors e_i are then fed into a PID-control loop, which in turn generates the two flap deflection speeds $\widetilde{\omega}_i$. These deflection speeds are mixed into the last time step's values by r.

$$\widetilde{\omega_i} = (1-r)\cdot\omega_i + r\cdot\left(\left(P\cdot e_i + I\cdot\int e_i + D\cdot\frac{\Delta e_i}{\Delta t}\right) / (\delta_{m,1})\cdot\omega_{m_i}\right) \tag{6.6}$$

6.3.3. Results

Four different maximum deflections and deflection speeds for the smaller flap part were investigated. Each configuration was run for the single flap (S) and combined (C) action with the larger flap part. The test case setups are tabulated in Tab. 6.1. To simulate different inflow conditions, two different functions A and B for the pitch angle Φ were used. Case A was a single sine function with $k = 0.1$ and pitch amplitude of $\Phi_m = 2°$. Case B consisted of the A oscillation superposed with another sine at $k = 0.4$ and an amplitude of $\frac{1}{5}\cdot\Phi_m$ at zero phase difference ($t^* = 0$). See Fig. 6.7 for a plot of the two pitch curves. In total, eighteen simulations were performed with different setups.

Name	δ_{m1}	δ_{m2}	ω_{m1}	ω_{m2}
0	0°	0°	0.00	0.000
L	2°	0°	0.02	0.000
L2	4°	0°	0.03	0.000
S1	0°	6°	0.00	0.025
C1	2°	6°	0.02	0.025
S2	0°	12°	0.00	0.050
C2	2°	12°	0.02	0.050
S3	0°	18°	0.00	0.075
C3	2°	18°	0.02	0.075
S4	0°	24°	0.00	0.100
C4	2°	24°	0.02	0.100

Table 6.1.: *Case setups for divided flap action; (S) single, (C) combined flap*

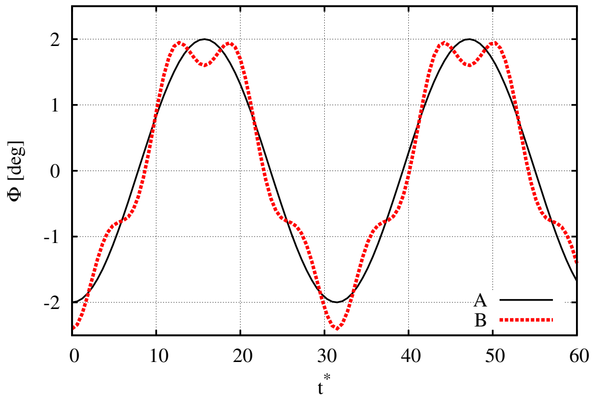

Figure 6.7.: *Pitch oscillations for cases A and B*

Fig. 6.8 shows the results comparing the effect of actuating only the second flap (1) and actuating both flaps (2) together. The plotted relative reduction is defined as $\frac{\rho}{\rho_L}$ with the reduction for case L where only the full flap is activated with

$\delta_{1\mathrm{m}} = 2°$. The reduction ρ itself, is always defined with the reference case 0, where the flaps were inactive.

$$\text{relative reduction} = \frac{\rho}{\rho_L} \tag{6.7}$$

$$\rho = 1 - \frac{\sigma^2}{\sigma_0^2} \tag{6.8}$$

We start with looking at the actuation of the single short flap. For a deflection of $\delta_{2\mathrm{m}} = 18°$, it is equivalent to the full flap with $\delta_{1\mathrm{m}} = 2°$ (relative reduction 1.03). This holds for both inflow types.
To achieve the same relative reduction as the full flap with $\delta_{1\mathrm{m}} = 4°$ (case L2, relative reduction 1.84), the full flap with lower maximum deflection $\delta_{1\mathrm{m}} = 2°$ has to be used together with the short flap at $\delta_{2\mathrm{m}} \approx 16°$.
For the cases at $\delta_{2\mathrm{m}} = 24°$, the single short flap is less efficient in the B-inflow than in the A-inflow, since it reacts to the additional changes (derivatives) in C_l.

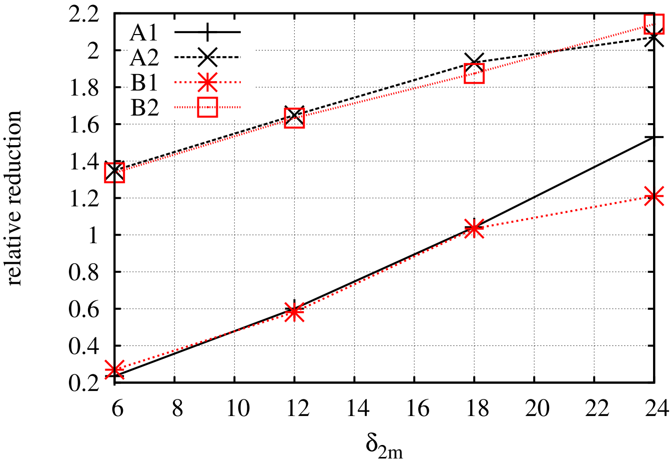

Figure 6.8.: *Relative reductions for pitch cases A and B and single (1) and double action (2) over maximum flap speed* $\delta_{2\mathrm{m}}$

The additional overall deflection of the double action increases the relative reduction for the whole range of flap deflections $\delta_{2\mathrm{m}}$. With an additional deflection of $\delta_{2\mathrm{m}} = 6°$ the relative reduction can be increased to 1.34. Comparing the two setups at $\delta_{2\mathrm{m}} = 24°$, the single flap's drop from case A to case B is not seen for the combined flap. The relative reduction for the double action flap even increases slightly from 2.07 to 2.14 (A to B).

6.4. Conclusion

Even though the present work only presents a very limited study, it has been demonstrated that the total deflection can be divided into two separated deflections, without losing control authority. The results suggest, that the combined use of two independent flap actuators is beneficial when dealing with complex inflows. Though, more studies on realistic stochastic inflows are needed.
The main driver for choosing between the different concepts has to be a cost function covering the overall system. Such a cost function would have to include load reductions, bills of material, maintenance costs etc., which is beyond the scope of

this work.
The hybrid immersed boundary method has clearly shown its flexibility when covering such geometries with superposed movements.

7. Flap as a sensor

7.1. Introduction

A disadvantage of most sensor concepts in smart rotor applications is their low survivability (including e.g. frequent replacement of strain gages, contamination of pressure holes, and lightning attraction). Clearly, integration of the whole flap system into a commercial wind turbine blade is nontrivial and additional restrictions to the blade's structural design and production process should be minimal.

A new idea to alleviate loads on wind turbines is to sense the local loading by measuring the fluctuating hinge moment acting upon a trailing edge flap [6, 14]. This measurement can provide an estimate of the change in local loading. The approach requires no extra parts outside the blade structure and may use robust hinge moment sensors. It is beneficial to use an already present trailing edge flap structure to supply a sensor input, especially when considering a possible modular layout of the system.

This chapter reports a study on hinge moment data acquired from a full scale test and draws some preliminary conclusions. Afterwards, a feasibility study on flap hinge moments as sensor input for load alleviation control on smart wind turbine rotors will be presented. A controller will be designed that uses an indicial response method to predict the flap hinge moment assuming constant inflow. The controller compares the predicted hinge moment with a measured hinge moment in disturbed inflow. The difference of the two values defines a flap deflection set point via a simple gain parameter.

To study the controller's performance, two-dimensional flow simulations were carried out for NACA63-200 type airfoil with a trailing edge flap of 16% chord length at a Reynolds number of 10^6.

The individual impacts of signal-to-noise ratio, first order sensor lag, incorrect flow velocity estimation, and increased angle of attack will be assessed to prove the robustness of the control concept.

This chapter has been partly presented in [15]. The content and the style have been adjusted to fit into the frame of this dissertation and Section 7.2 concerning the full scale measurements has been added.

7.2. Full scale measurements

As a first step in evaluating the approach of using hinge moment measurements as control inputs, we will derive a conclusion from a full scale measurement campaign. The experiment was conducted on a Vestas V27 (Fig. 7.1) wind turbine owned by Risø DTU. The V27 is a pitch controlled horizontal axis turbine with a rated power of 225 kW. The blades are 13m long. The test site is located at the Risø DTU campus in Roskilde. Within the ATEF project, the turbine was equipped with multiple sensors and one blade was equipped with three trailing edge flaps. A meteorological mast was located 70m west of the turbine.

We will first investigate if a correlation between the flap hinge moment and the angle of attack (via a local Pitot tube) can be found in the measured data. Fig. 7.2 shows a sketch of the general setup. Since we will only investigate cases where the flap is fixed, the whole flap system can be simplified to a single load carrying cantilever. A strain gage is located close to the cantilever's attachment to the blade (root). The raw strain gage output is denoted by $a_{3,1}$[Volts]. To simplify the investigation, we will use the value $a_{3,1}$ directly, without translating it into an equivalent hinge moment.

Figure 7.1.: *ATEF turbine with active trailing edge flaps and Pitot tubes*

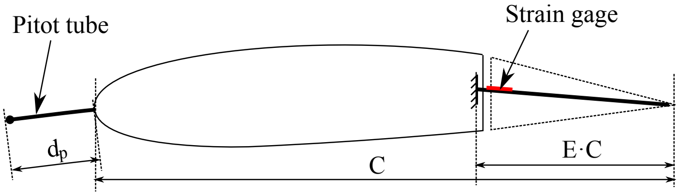

Figure 7.2.: *Sketch of experimental setup and strain gage placement*

All measurements presented were band-pass filtered (0.2-5Hz). Fast Fourier Transforms (FFT) were applied to the filtered signals with four averaging blocks for the given time series. The sampling rate of the measurements was 100Hz. The turbine operated at a rotor speed of 43rpm[1]. The wind speeds W and direction were taken from the meteorological mast at a height of 30m placed close by the turbine. The prevailing wind direction was north-eastly (inland direction, no turbine wake). In particular, we will investigate three specific time series of two minutes each (Tab. 7.1).

We will now have a closer look at the local angle of attack α, the strain gage measurement $a_{3,1}$ (both at radius $R = 11m$) and the blade flap-wise bending moment M_x to get a first impression of the relations between them. In Fig. 7.3, the angle of attack, the strain gage measurement and the flap-wise blade root bending moment are plotted. They are non-dimensionalized by applying equation 7.1, where γ is a

---

[1] The V27 comprises a two generator design for low/high winds

date dd.mm.yyyy	time hh:mm	W_{avg} m/s	$\sigma(W)$ m/s	Ti [-]
10.02.2010	12:40	9.30	0.82	0.09
10.02.2010	14:20	8.81	0.94	0.11
10.02.2010	14:30	8.07	1.20	0.15

Table 7.1.: *Two minutes series, average wind speeds W_{avg} and turbulence intensity Ti*

variable place holder and the bar denotes the average.

$$\gamma_0 = \frac{\gamma_i - \bar{\gamma}}{\max(|\gamma - \bar{\gamma}|)} \tag{7.1}$$

There is clearly a connection between the angle of attack and the bending moment in Fig. 7.3(a), where α is phase-leading when the curve moves away from the mean and phase-lagging when it moves back. When plotting both the angle of attack and the flap strain gage measurement in Fig. 7.3(b), we see that the behavior is very similar, but the strain gage measurement generally lags behind the angle of attack measurement.

In Fig. 7.4, we compare the measurements in the frequency domain for a single time series (12:40). First, we look at the blade bending moments in flap-wise (M_x) and edge-wise (M_y) direction. M_y is mostly influenced by the 1P, first edge-wise and flap-wise eigenfrequencies. M_x shows contributions of 1P, 2P, 3P and both first eigenfrequencies. The two spectra of the angle of attack α and the strain gage measurement $a_{3,1}$ look very similar to that of the flap-wise bending moment.

The plot also presents an additional strain gage measurement $a_{1,1}$ on the flap root closer to the hub. Here, the first edge-wise eigenfrequency is more pronounced, while the first flap-wise shows less clearly than for $a_{3,1}$.

To quantify the correlation between the angle of attack and the measurement of flap root strain gage we can first define a new quantity $\tilde{a}$ as follows:

$$\tilde{a} = \frac{a_{3,1}}{V_{\text{rel}}^2} \tag{7.2}$$

The relative velocity V_{rel} is measured with the local Pitot tube. The correlation R between the angle of attack α and $\tilde{a}$ is defined by the correlation coefficients

$$R = \frac{C(\alpha, \tilde{a})}{\sqrt{C(\alpha, \alpha) C(\tilde{a}, \tilde{a})}} \tag{7.3}$$

where C is the covariance matrix

$$C(x_1, x_2) = E[(x_1 - \mu_1)(x_2 - \mu_2)] \tag{7.4}$$

with E being a function giving the expected value and

$$\mu_i = E[x_i] \tag{7.5}$$

Fig. 7.5 shows a study of R, where an offset t_0 was introduced[2] when comparing the two unfiltered values. It shows, that an offset of about 0.03s is beneficial for times series 12:40 and 14:20, while a slightly longer time gives better results for case 14:30 (the one with the highest turbulence intensity and lowest average wind speed). A time span of 0.03s correspond roughly to a traveled distance of 1.5m at flap three. This is longer than the distance between the Pitot tube head and the flap of 1.22m, suggesting that there is an additional time lag due to the blade aerodynamics.

The effect on the correlation of averaging the values is shown in Fig. 7.6. The correlation coefficient is plotted over the length of the averaging window t_w. The curve starts at R=0.801 and has a maximum of R=0.986 at $t_w \approx 1.3$ which corresponds roughly to one full rotor revolution. The effects of wind shear, yaw error etc. are therefore averaged out and the correlation is driven be large scale wind speed changes.

Finally, a comparison with the temporal self-correlation of the angle of attack shall

---

[2] by using data points at a later time, thereby comparing $\alpha(t)$ with $\tilde{a}(t + t_0)$

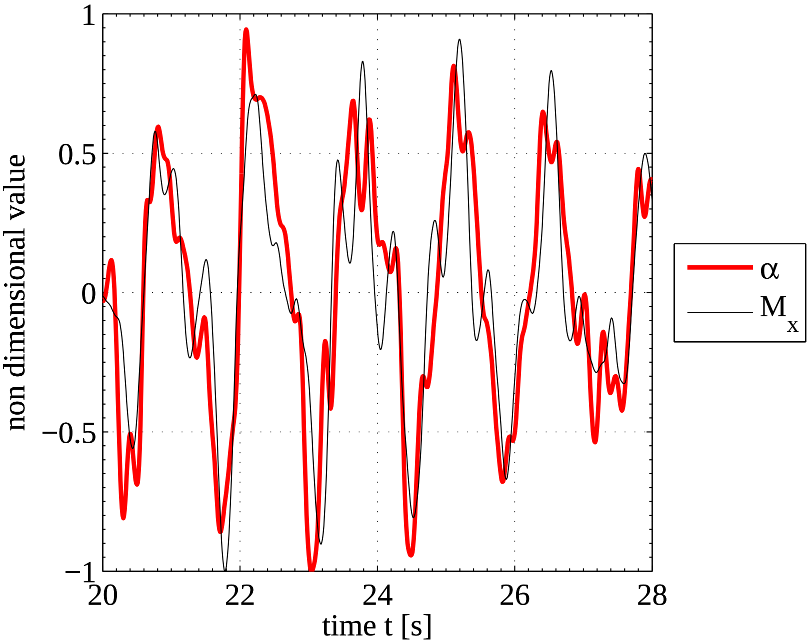

(a) Angle of attack α and blade root flapwise bending moment M_x

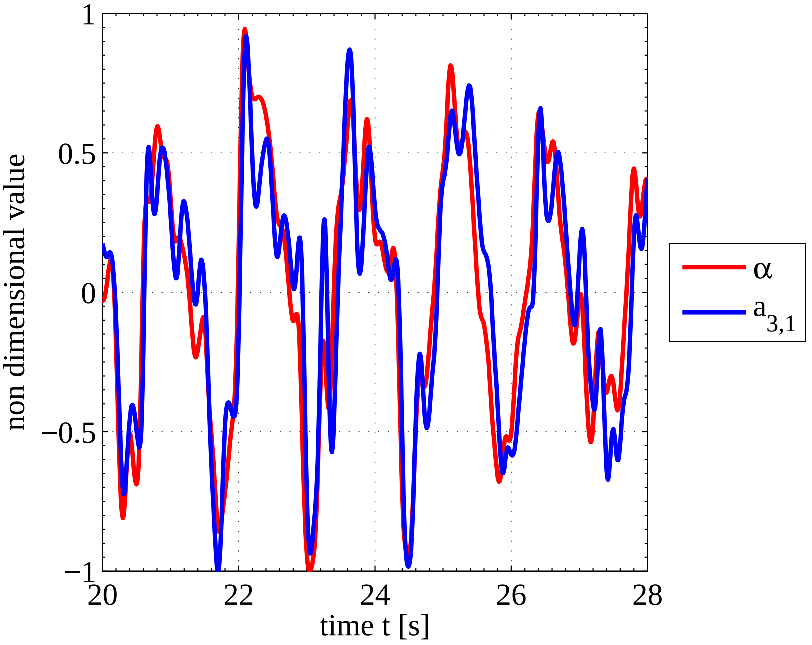

(b) Angle of attack α and blade root flapwise bending moment M_x

Figure 7.3.: *Comparison of angle of attack α with blade root flapwise bending moment M_x and flap root strain gage output $a_{3,1}$, filtered*

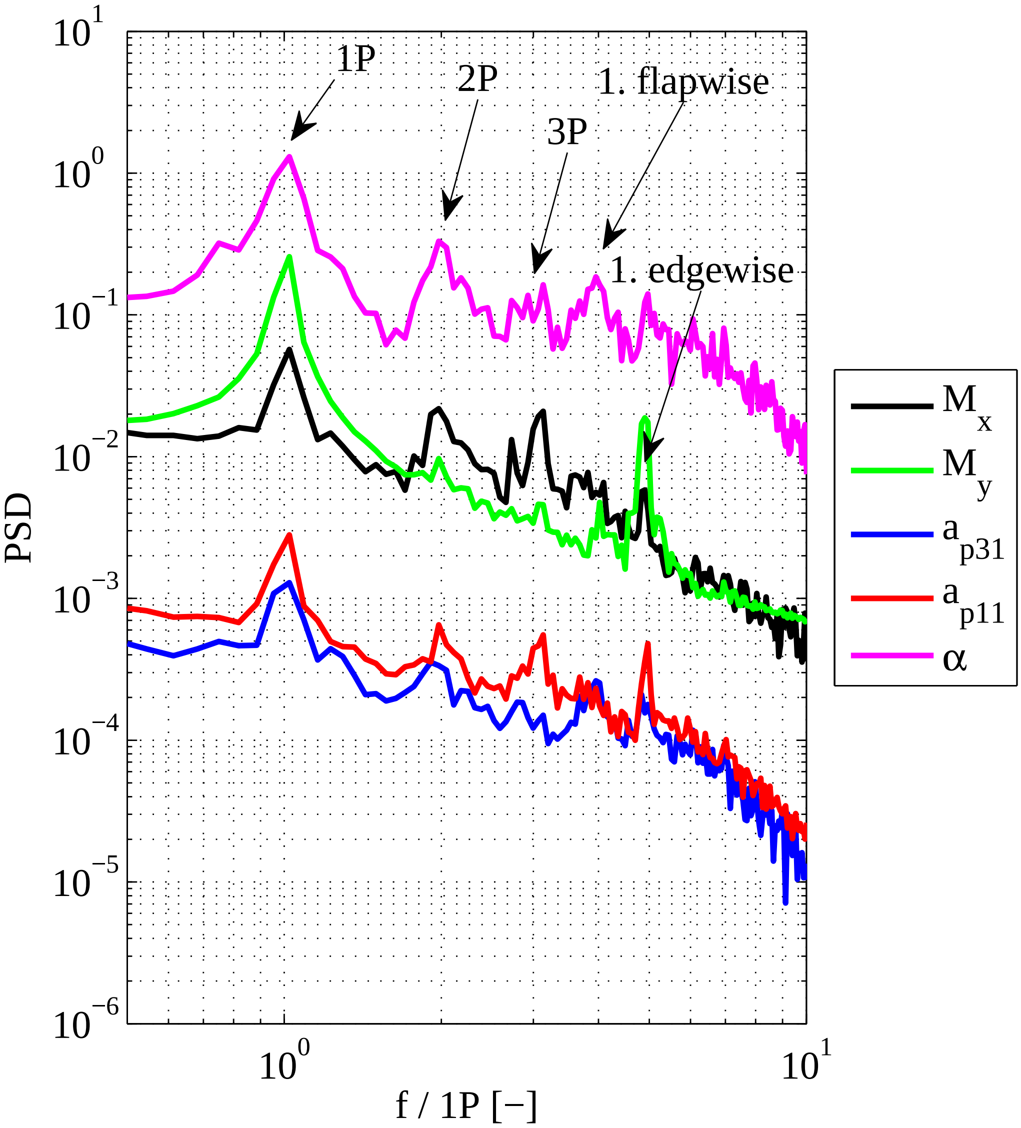

Figure 7.4.: *Power spectral densities from measurement (12:40)*

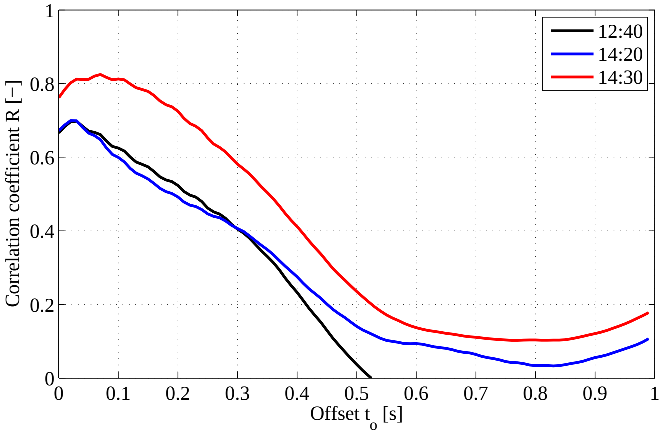

Figure 7.5.: *Correlation R with a time offset* t_0

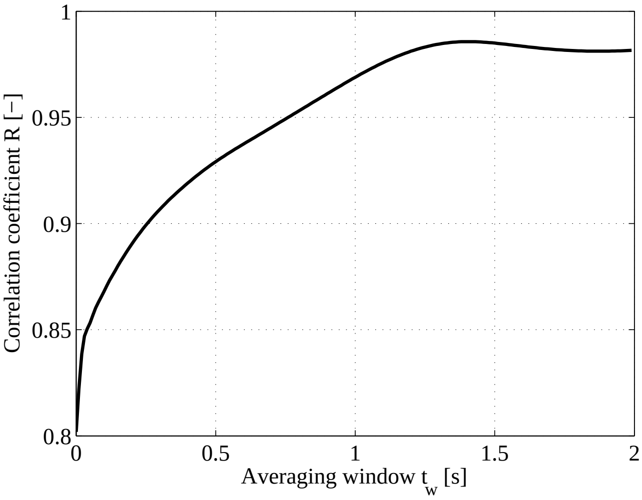

Figure 7.6.: *Correlation between* $\alpha(t)$ *and* $\tilde{a}$ *with averaging window*

be drawn. Fig. 7.7 shows the self correlation of the angle of attack $\alpha(t)$ with $\alpha(t+t_0)$.

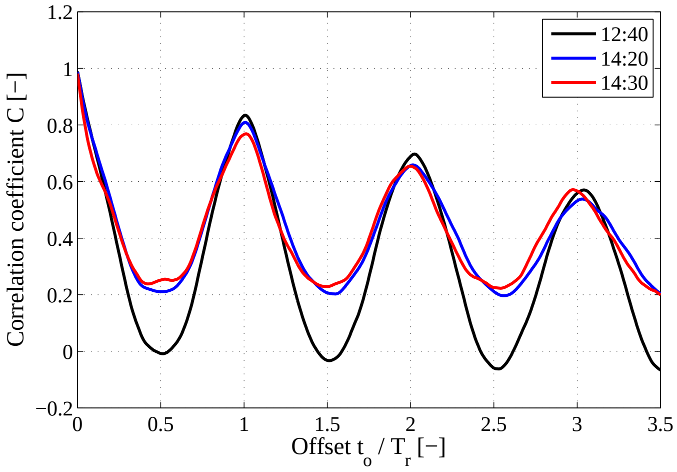

Figure 7.7.: *Correlation between* $\alpha(t)$ *and* $\alpha(t+t_0)$

We can see, that the temporal correlation of the section's angle of attack with itself goes down, while it travels along circumference. When the blade is returning to its starting position, the correlation increases again, since there is also the effect of the spatial correlation. Looking at the first peak after one rotation, we can clearly see, that for the lower turbulence case (12:40) the best correlation exists, while the correlation decreases with increasing turbulence level.

Conclusion of measurement

The measurements showed that a correlation between the angle of attack and the output of the flap root strain gage exists. The measurements covered only static flap deflection, though. The main difficulty in using the hinge moment of a moving flap as a sensor input lies in the hinge moment's strong dependency on the flap deflection and the deflection rate when both aerodynamic and inertial forces are concerned.

Within the following section, a load alleviation controller based on flap hinge moment and deflection sensing will be presented. The controller will then be applied to two-dimensional CFD simulations of an airfoil with a flexible trailing edge flap using the hybrid IB approach. To investigate feasibility of the approach, the potential reductions in lift coefficient variance will be studied for disturbed inflow conditions. Finally, the robustness of the developed controller will be presented.

7.3. Modeling of the unsteady hinge moment

For attached flows, aerodynamic indicial response theory [75, 82] deals with solutions to step changes between two steady conditions. The main advantage of this theory is that one can easily compose an arbitrary history of flow state values by single impulse solutions. In general, airfoil loads consist of a circulatory and a non-circulatory term. The circulatory load gradually builds up to a steady value, while the non-circulatory load or 'apparent mass' represents an instantaneous loading that quickly reaches zero again. Hariharan [32] derived an inviscid compressible flow model for airfoils equipped with plain trailing edge flaps. The model supplies the unsteady additional lift, moment, and hinge moment coefficients for time varying inputs of flap deflection δ and deflection rate $\mathrm{d}\delta/\mathrm{d}t$. The time-discrete formulation of the model is beneficial for embedded control systems. Figure 7.8 shows the resulting amplitudes of the main aerodynamic components for a sweep of reduced frequencies. Equation 7.6 defines the reduced frequency k, where f is the significant frequency; C is the airfoil chord length and U the free stream velocity.

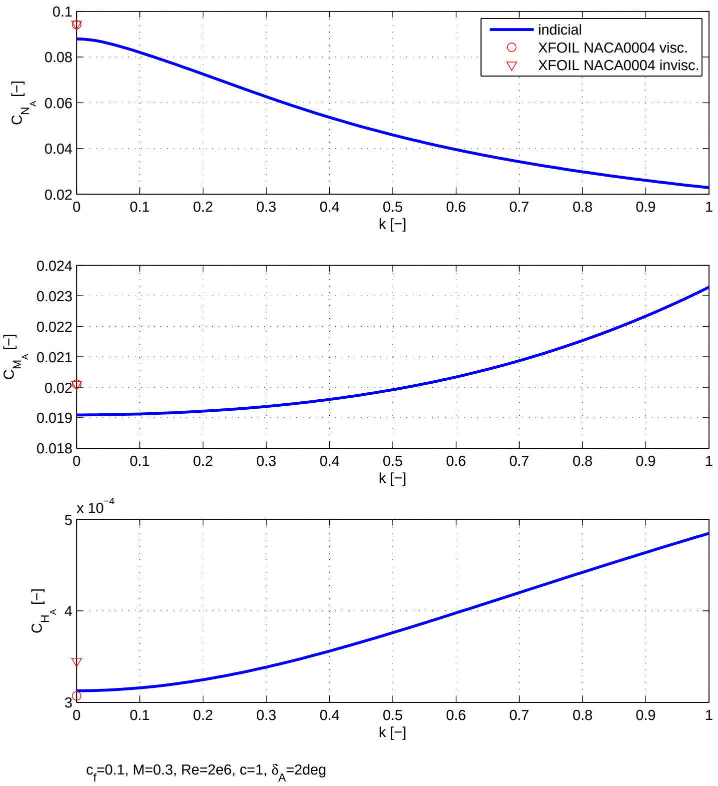

Figure 7.8.: *Hariharan [32] model*

$$k = \frac{\pi f C}{U} \tag{7.6}$$

The flap length was 10% chord and the deflection amplitude was two degrees. For a reduced frequency $k = 0$ (i.e. static values) XFOIL calculations of a NACA0012 in viscous and inviscid flow were compared. The difference between the two hinge-moment coefficients is about 10%, while the result of the indicial model lies in between them.

Since the model was applied in connection with smoothly curved flaps, instead of plain flaps, the influences of the shape deviation (see Section 5.3.2) will be investigated.

We compared the implemented model with hybrid IB calculations and Gaunaa's thin airfoil flow model [29]. The latter is able to handle generalized deflection mode shapes (including both plain and smooth flaps). The flow conditions were at a Reynolds number of $\mathrm{Re} = 10^6$, a center angle of attack of $\alpha_c = 0°$, a reduced frequency of $k = 0.1$, and a flap length of 16% chord. For the hybrid IB calculations, we used a NACA63-200 geometry (see details below in Section 7.5). Figure 7.9 shows the amplitudes of the hinge moment coefficient C_h for different oscillating flap deflections. For the plain flap (sc = 1), the differences between both thin airfoil codes and the hybrid IB simulations were in the range of 40%-60%. Whereas the amplitudes of the plain flap calculated with the Gaunaa code and the curved IB flap agreed well. Gaunaa's code overpredicted the effect of a smoothly curved flap (sc=2) by a factor of about 2.8 compared with the EllipSys2D results. This difference was most likely due to the smooth flap's high local trailing edge angle compared to the full flap deflection angle (factor of 3.9), because the trailing edge angle is of central importance in potential flow solvers.

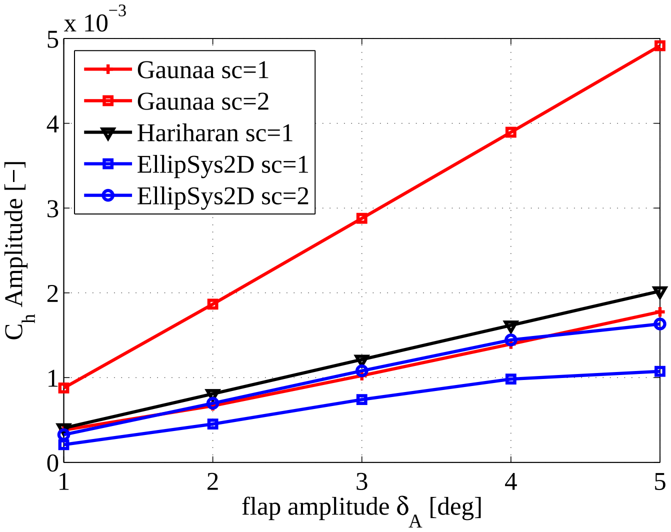

Figure 7.9.: *Hinge moment amplitudes for an oscillating trailing edge flap*

Fig. 7.10 presents hybrid IB results for a pitching airfoil (pitch amplitude $\Phi_A = 5^\circ$) at a low reduced frequency of $k = 0.01$. For different static flap deflections, the hinge moment coefficients demonstrated a non-linear behavior. The figure also shows that

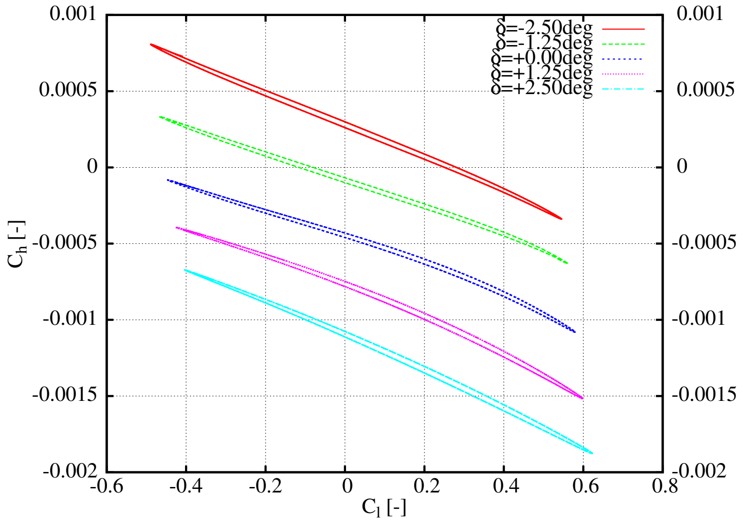

Figure 7.10.: *Hinge moment coefficient C_h over lift coefficient C_l for different flap deflections δ and oscillating pitch at a reduced frequency of $k = 0.01$*

the evaluation of any measured hinge-moment needs information about the flap deflection and - for unsteady cases - knowledge about the flow history is needed.
Flap efficiency factors were introduced to manage the viscous effects as well as the shape derivation between the flexible flap and the plain flap. We implemented two additional factors $\epsilon_{u/d}$ for upward and downward deflections. They were inherent to the used airfoil/flap geometry, but changed with angle of attack and flap deflection. Although a multi variable function $\epsilon_{u/d}(\alpha, \delta)$ was considered beneficial, a static combination of flap efficiency factors was chosen to reduce the complexity of the design process.

7.4. Controller design

The implemented controller (see Figure 7.11) consisted of two parts. The first part was an open-loop control based on the difference between a measured (CFD) and a predicted hinge moment $\Delta C_h = C_h - C_{h,p}$. The predicted hinge-moment coefficient itself consisted of the airfoil's steady state coefficient $C_{H,0}$ and an additional part due to the flap deflection. The open-loop provided a flap deflection set-point δ_s. In this investigation, a constant gain of $k_h = 4.66 \cdot 10^2$ was applied. A low-level PID controller ensured that the flap followed the set point. Additionally, the low-level controller mimicked a real flap actuator by applying restrictions to maximum flap deflection and maximum actuation speed. Further, the updated flap deflection speed was low-pass filtered ($\tau = 2.4$ms) . The results were smoothed flap actuation and an additional flap actuation time constant of $\tau = 3.4$ms (for $\Delta\delta = 1°$). For the integral part of the low-level controller, an anti-windup technique allowed for actuator saturation. The flap efficiency factors were obtained by running oscillating flap cases with steady inflow. Additionally, the factors were subjected to a parameter optimization for the design control case.
The following section will describe the geometry and the numerical setup of the conducted simulations, where the controller was applied.

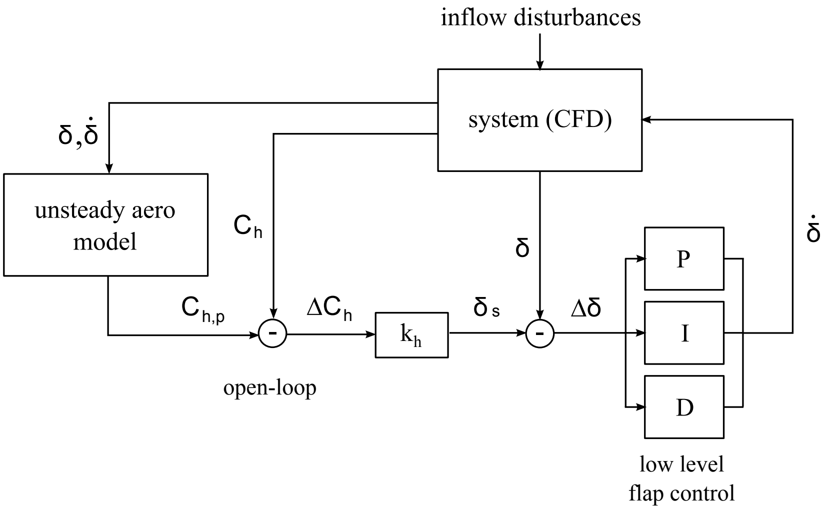

Figure 7.11.: *Controller diagram*

7.5. Geometry and numerical setup

The used airfoil geometry was a NACA63-200 with a slightly modified trailing edge and relative thickness of 16.6%. The flap length was 16% of the chord. The hybrid approach was used when generating the 2D computational domain (Fig. 7.12). The trailing edge had a bluntness of 0.2% chord. The total number of grid points was $64 \cdot 64 \cdot 9 = 36.864$. The first cell height above the wall allowed to obtain a dimensionless wall distance y^+ smaller than one. A similar grid spacing was kept close to the immersed boundary.

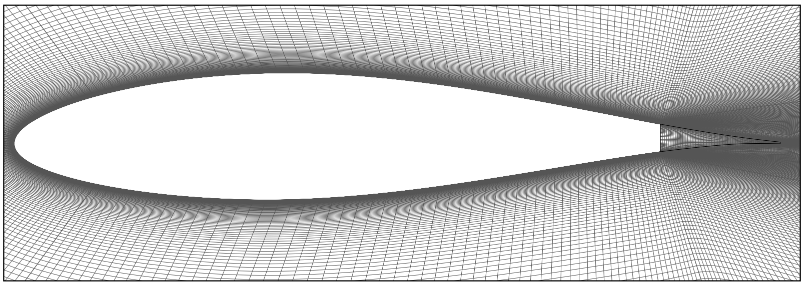

Figure 7.12.: *Airfoil mesh with immersed boundary (-) flap*

All calculations were performed at a Reynolds number of $\text{Re} = 10^6$. The distance of the airfoil to the free stream boundaries was 11 chord lengths[3]. The simulations ran for 120.000 non-dimensional time steps ($\Delta t^* = 0.002$), starting from a steady solution. For post-processing the first 5% of the resulting output were dropped, resulting in 7.25 periods of simulated pitch oscillation for $k = 0.1$.

An upstream turbulence plane introduced velocity fluctuations via an additional forcing term [77]. The turbulence model of Mann [47, 48] provided the underlying turbulence field. The forcing resulted in a one-dimensional turbulence intensity in free stream direction of $\text{Ti} = 11.85\%$.

7.6. Results

For the above setup, the controller was applied for different pitch amplitudes and two different reduced frequencies of the pitch oscillation[4] $k = 0.033$ and $k = 0.1$. The maximum allowed flap deflection was fixed to $|\delta_{max}| = 4°$ for all cases. This deflection resulted in an estimated maximum change in the equivalent angle of attack[5] of $\alpha_0 = \pm 1.6°$. The maximum flap deflection speed was fixed to $|\omega_m| = 0.05$.

7.6.1. Design case

The controller was designed for a pitch amplitude of $\Phi_A = 2°$ at a reduced frequency of $k = 0.1$. The center angle of attack was $\alpha_c = 0°$. Fluctuations from the turbulence plane accounted for an additional angle of attack amplitude of about $\pm 0.5°$. Therefore, the flap could not fully cancel out the effect of the inflow change on C_l and the flap 'actuator' was saturated a considerable amount of time.

We chose the variance σ^2 of the lift coefficient as an estimate of fatigue loads. Equa-

---

[3] This is a rather small distance to the domain boundary, but for the demonstration of a controller it is considered to be sufficient.

[4] corresponding to the 1P and 3P frequencies on a small utility-scale turbine

[5] for a symmetric airfoil, according to [4], c.f. Fig. 2.3

tion 7.7 defines the reduction ρ with the reference variance (uncontrolled case).

$$\rho = 1 - \frac{\sigma^2}{\sigma^2_{ref}} \tag{7.7}$$

For the controlled design case a reduction of $\rho = 71.76\%$ was achieved. The same controller resulted in a reduction of $\rho = 83.40\%$ for a decreased amplitude of $\Phi_A = 1°$ and a decreased reduced frequency of $k = 0.033$. A reduction of $\rho = 79.94\%$ was achieved for a combination of pitch amplitude $\Phi_A = 1°$ and reduced frequency $k = 0.1$.

Figure 7.13 shows the C_l variances σ^2 and the corresponding relative reduction ρ/ρ_0 for a range of different pitch amplitudes Φ_A and two different reduced frequencies. The index 0 denotes the C_l variance reduction of 83.40% for the best case ($k = 0.033$, $\Phi_A = 1°$). The drop at $\Phi_A = 0.5°$ was due to the pitch oscillation effect being in the order of the stochastic turbulence fluctuation, as indicated by the values of the absolute variances. For zero pitch amplitude, the controller even increased the variance since only high frequency disturbances were present.

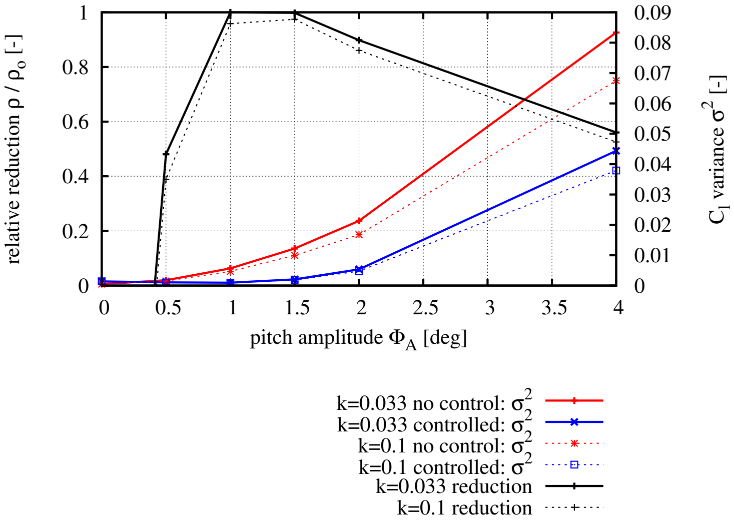

Figure 7.13.: *Variance reductions ρ for different pitch amplitudes and frequencies*

7.6.2. Robustness

For wind turbine implementation of the hinge-moment based controller, one can consider the rotor speed and flap deflection to be measurable with good quality. The wind speed estimated by nacelle anemometers is less suited for high-speed control purposes. The uncertainty of any hinge moment measurement is clearly depending on the chosen sensor type and setup.

In the following, the effects of signal noise, a first order sensor time constant, and the estimated total inflow velocity on the *relative reduction* ρ/ρ_0 will be investigated. The index 0 denotes the reduction ρ_0 for the design case ($k = 0.1$, $\Phi_A = 2°$).

To investigate changes in signal-to-noise ratio (SNR), white Gaussian noise was added to the hinge moment measurements. The noise was generated by the polar method of [49] based on the Box-Muller Method [16], which uses the technique of inverse transformation to turn two uniformly distributed randoms, U1 and U2, into two unit normal randoms, X and Y.

```
    S=1;
    do while (S.ge.1)
      call random_number(U1)
      call random_number(U2)
      V1=2*U1-1;
      V2=2*U2-1;
      S =V1*V1+V2*V2;
    end do
   wgnoise = meanv + sqrt(variance) * sqrt(-2*log(S)/S)*V1;;
```

$$\text{SNR(dB)} = 20 \cdot \log\left(\frac{A_s}{A_n}\right) \tag{7.8}$$

Eqn. 7.8 defined the SNR in decibel; A_s and A_n were the root mean square amplitudes of the signal (from a clean run) and the added noise respectively. Fig. 7.14 depicts the results, showing the raw SNR and the input to the controller after low-pass filtering with a time constant of $\tau = 0.3$ms. Low-pass filtering naturally enhanced the results when signal noise was present. For a SNR of 3dB, ρ/ρ_0 dropped to around 70%.

To investigate the effect of signal lag, the reduced cut-off frequency k_c of a first order sensor model was changed. As shown in Fig. 7.15, decreasing the cut-off frequency decreased the potential for load reduction. At $k_c = 0.077$ the relative reduction dropped to 50%, while at $k_c = 0.045$ no load reduction was achieved anymore.

The dimensionless force and moment coefficients are by definition directly affected by changes in air density and flow velocity. For a small utility-scale wind turbine, we can assume the wind speed estimate to be off by ±5%. The resulting uncertainty in the airfoil's inflow velocity would be around ±0.35%. Fig. 7.16 shows the behavior of the relative reduction ρ/ρ_0, when the value of the flow velocity V was modified within both the hinge moment model and the calculation of the hinge moment coefficient. An error of ±5% on the flow velocity V estimate resulted in a ρ/ρ_0 of 85% for the lower estimate and a decrease to 69% for the higher estimate. Increasing the velocity estimate by 10%, a significant load reduction could no longer be achieved, while decreasing the estimate by 10% lowered the relative reduction to 56%.

The controller was also applied to different angles of attack α_c. For each angle of attack α_c, we adjusted the corresponding steady C_{H0}. Fig. 7.17 shows the C_l variances σ^2 and the relative reductions ρ/ρ_0 based on the design case. The controller operated above 94% of relative reduction ρ/ρ_0 for $0° < \alpha_c < 9.5°$. A further increase in angle of attack resulted in a steep drop in ρ/ρ_0. Fig. 7.18 shows the time series of the lift coefficients for a representive case at $\alpha_c = 5°$, clearly demonstrating the amplitude reduction for the controlled case.

7.7. Conclusion

The hinge moment of a trailing edge flap was applied as a sensor input for a load alleviation control. A thin airfoil model based on indicial response theory predicted the flap hinge moment in steady inflow for arbitrary flap deflections. The developed controller compared this predicted hinge moment with a measurement. Based on the difference, the controller generated a flap deflection set point aiming to reduce fluctuations in lift coefficient. The controller was applied to hybrid IB simulations of an airfoil with a flap of 16% chord length. The inflow disturbances consisted of a rotating frame of reference and an additional turbulence plane upstream of the

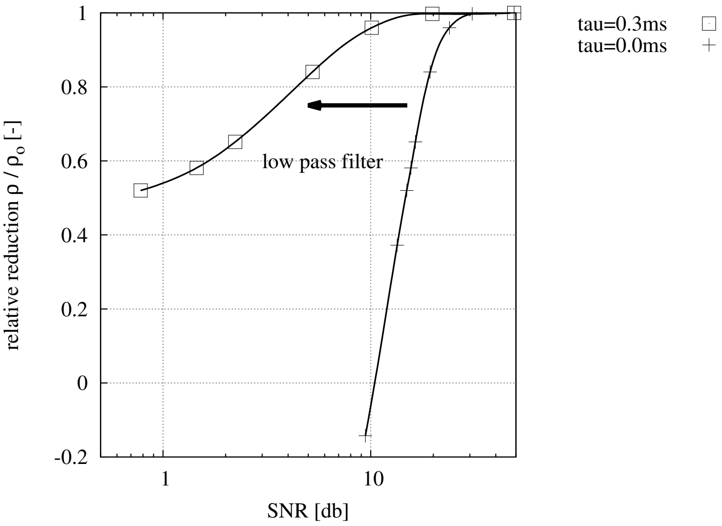

Figure 7.14.: *Variation of signal-to-noise ratio*

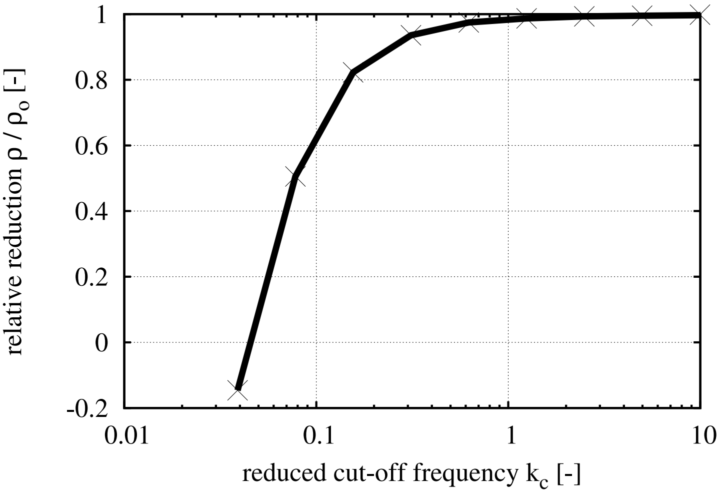

Figure 7.15.: *Variation of reduced cut-off frequency k_c*

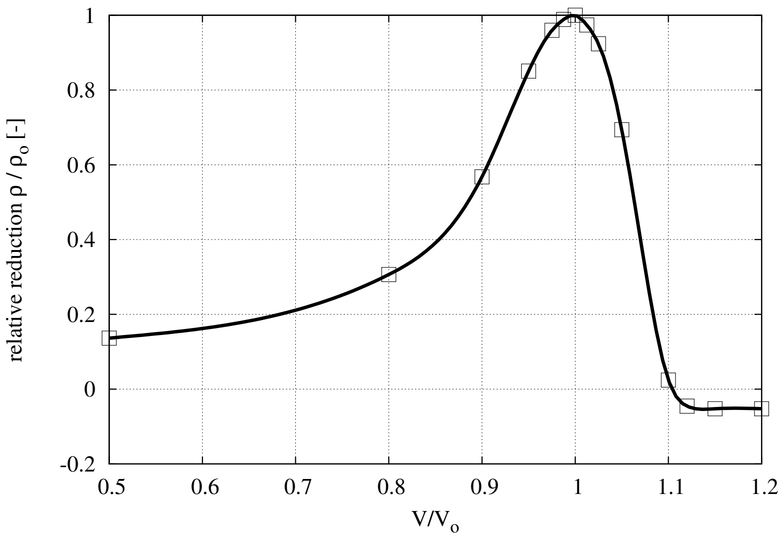

Figure 7.16.: *Variation of estimated inflow velocity V*

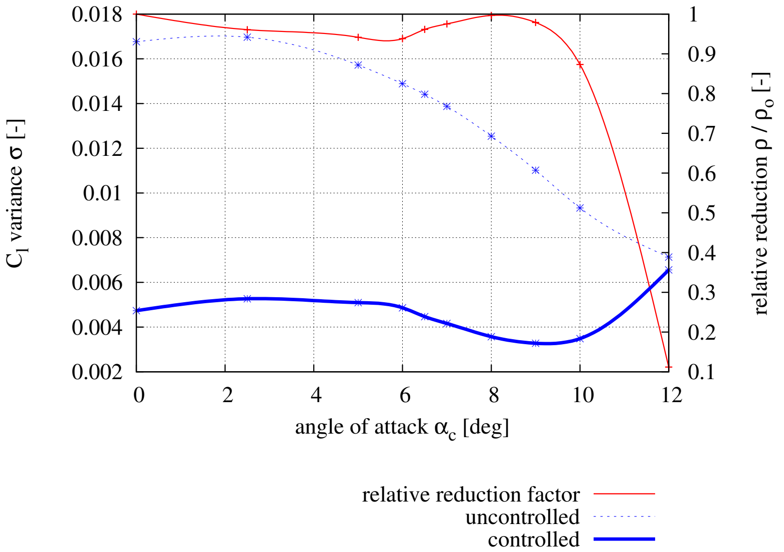

Figure 7.17.: *Lift coefficient variances and their reductions over center angle of attack α_c*

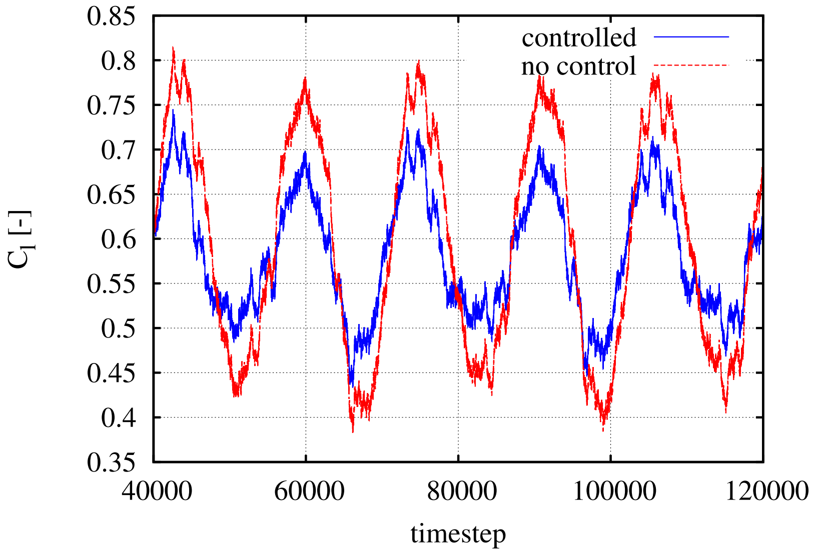

Figure 7.18.: *Lift coefficient* C_l *over time step for* $\alpha_c = 5°$

airfoil.

It was shown that the hinge-moment based control could alleviate the effects of inflow disturbances, even with frequently saturated actuators. The reduction in lift coefficient variance was 71.76% for the design case of underlying pitch oscillation amplitude $\Phi_A = 2°$ at a reduced frequency of $k = 0.1$. For an amplitude of $\Phi_A = 1°$ and a reduced frequency of $k = 0.033$, a maximum reduction in C_l variance of 83.40% was demonstrated.

Both a signal-to-noise ratio of 3dB and a first order model time constant of 30ms each resulted in a decrease to 70% of the maximum variance reduction. Erroneous flow velocity estimation of -5% decreased the reduction to 85%, while overestimating by 5% resulted in 69% of maximum variance reduction. The controller operated above 93% of relative reduction ρ/ρ_0 for $0° < \alpha_c < 9.5°$. A steep drop in relative reduction occured for higher angles of attack, when the flow was separated.

Despite the rather small flap deflections of only four degrees, the developed alleviation method showed good potential and was comparable to a controller using the deviation in lift coefficient as control error. Flap configurations with more control authority might lead to better results. For the presented method, longer flaps with moderate deflections would be beneficial to enhance the signal quality and reduce the risk of flow separation.

8. Blade section with flaps

8.1. Introduction

This chapter applies the 3D implementation of the hybrid immersed boundary method to three problems. Firstly, a span-wise flap gap of 3% chord will be investigated for an undeflected flap on a low Reynolds number airfoil. A similar configuration will be used to demonstrate the implementation of a flap controller for two independent flaps. As a final demonstration of the hybrid immersed boundary method, the flow around a 50% span-wise flap on a section will be investigated at a high Reynolds number. The resulting flow on and behind the airfoil section will be presented.

8.2. Flap gap

One interest when designing control surfaces is to quantify the effects of span-wise gaps between the moving surface and the static part of the geometry or other moving parts. In CFD simulations, the flap gap has to be sufficiently resolved. When moving meshes are used, the mesh generation is hard to handle since highly skewed and stretched cells might appear.
The main restriction for representing gaps with an IB method is that at least three cells are required between the two bodies. The external forcing cells would overlap otherwise. This restriction is of a more theoretical nature, when assuming that a gap will be sufficiently resolved to capture the main flow features.

8.2.1. Geometry and numerical setup

The mesh for the NACA0015 airfoil geometry of section 5.2 was extruded to a span of 0.5 chord. The span-wise cells were distributed with a cosine function to cluster more cells in the middle region. The cell count in span-wise direction was 32. The flap covered 10% of the chord length. Two setups were investigated. The first setup applied a full span trailing edge that was represented by one immersed boundary body. The second setup represented the flap geometry by two single bodies with a span-wise gap of 3% chord in between them ($y = 0.24$ to $y = 0.27$, covered by 12 cells in span-wise direction).
The Reynolds number of the simulation was $\mathrm{Re} = 25,000$ and the angle of attack was fixed to $\alpha = 5°$. The non-dimensional time step of the unsteady simulations was $\Delta t^* = 0.01$.

8.2.2. Results

Fig. 8.1 visualizes both geometries by iso-surfaces of the velocity magnitude. We can clearly see the gap region between the two immersed boundaries in the right hand figure. Additionally, slices at $y = 0.01$ show the total pressure contours. We recognize the thick loss area for both cases. The snapshot in Fig. 8.2 shows a cut through the gap center at $y = 0.255$. The velocity magnitude and streamlines for the u and the w velocity components are shown. The figure points out two regions. Region A shows a large separation bubble after the mid-chord region on the suction side. Region B shows the entry of fluid from the sides into the gap region in a spiral structure. We see that fluid from the pressure surface is entering the gap. The flow

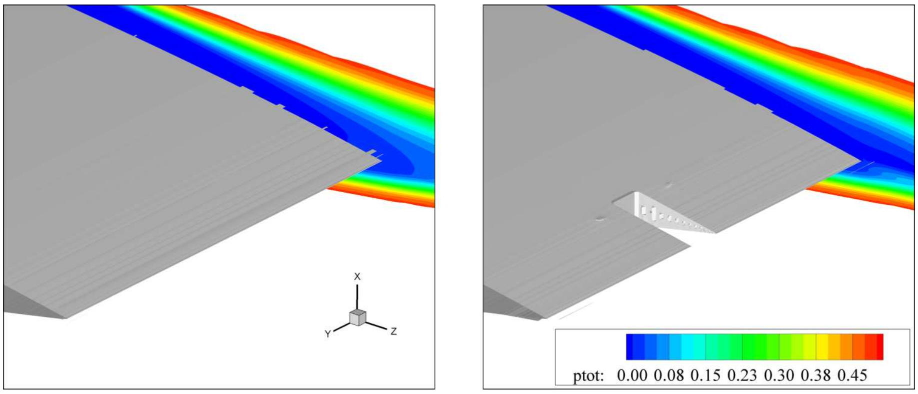

Figure 8.1.: *Geometry of NACA0015 section with/without gap via iso-surfaces of* $|V| = 0.001$*; slice shows* p_t *at* $y = 0.01$

reaches the suction surface eventually. The airfoil effectively de-cambers in this sectional cut, when comparing with the full airfoil. Fig. 8.3 compares the unsteady lift curves for both setups. One notices that both setups exhibit a sinusoidal variation in the lift coefficient. The amplitude for the setup with gap increases, while the average slightly decreases. Tab. 8.1 presents the averaged values for lift and drag coefficients[1], their peak-to-peak amplitudes and their glide ratios. The averaged values differ only slightly between the two cases, resulting in a 0.5% reduction in glide ratio for the 'gap' case. Both lift and drag amplitudes are higher for the case with the gap by factors of 2.21 and 2.54.

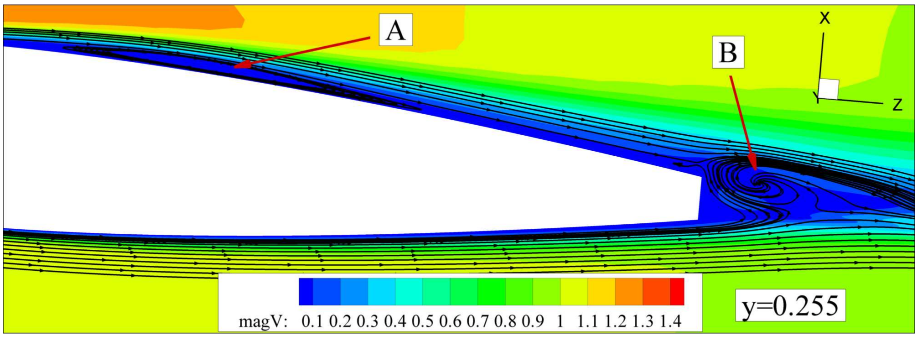

Figure 8.2.: *Streamlines in gap at $y = 0.255$, streamlines generated with u and w velocity components*

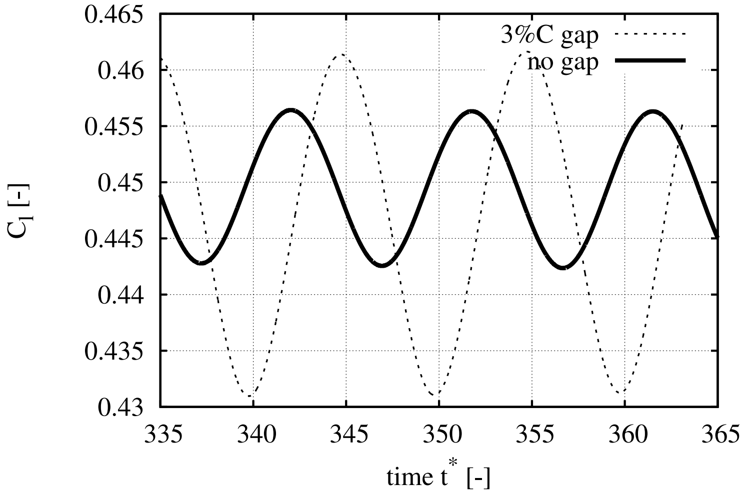

Figure 8.3.: *Comparison of unsteady lift curves, span-wise average*

To investigate the flow field further, Fig. 8.4 shows recirculation areas ($w = -0.01$)

	$\overline{C_l}$	C_l^a	$\overline{C_d}$	C_d^a	$\overline{C_l}/\overline{C_d}$
no gap	0.4463	0.0137	0.03546	0.0013	12.66
gap	0.4443	0.0303	0.03548	0.0033	12.59

Table 8.1.: *Lift and drag coeffcients*

---

[1] C_l and C_d with reference to unit area

on the airfoil section. The configuration without gap shows two large areas of recirculation. One is starting at the location of maximum thickness and one is starting slightly upstream of the flap part. Indeed, these two recirculation areas are only one connected separation region. They are only separated in the present visualization because of the assigned iso-surface level. For the 'gap' case, the strengths of the recirculation areas change esp. in the trailing edge region. Here, the length of the iso-surface is about halved and we can see an upstream flow emerging from the gap. The upstream iso-surface is slightly influenced by the flow through the gap, shortening slightly in the side region.

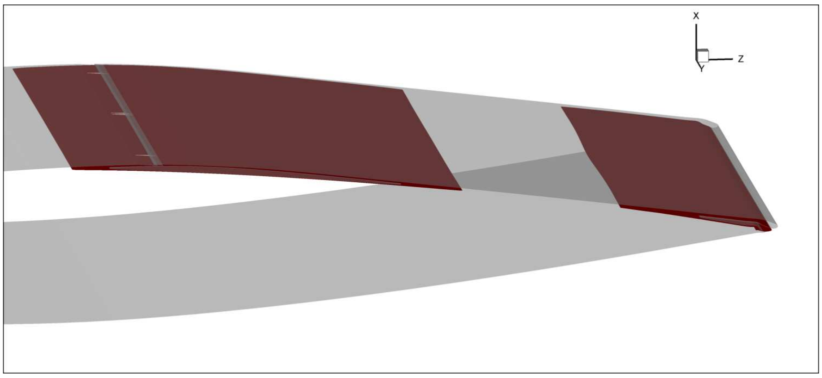

(a) no gap

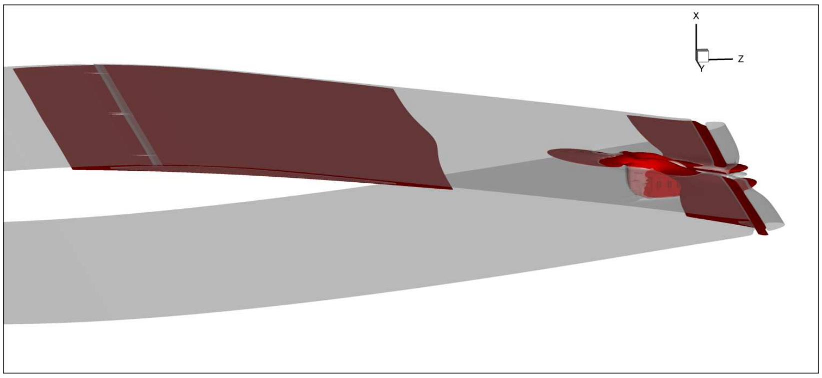

(b) gap

Figure 8.4.: *Recirculation areas, iso-surface of* $|V| = 0.02$ *(grey) and iso-surface of* $w = -0.01$ *(red)*

8.2.3. Conclusion

This test case was set up for a low Reynolds number of $\mathrm{Re} = 25,000$. At this Reynolds number, the flow is susceptible to separation and large separation areas showed on the airfoil. The difference in values of lift and drag between the two cases was small. However, the flow field did change and a flow through the gap to the suction side was observed. This flow reduced the strength of the recirculation area in the trailing edge region and thereby mitigated the influence on the lift and drag coefficients. The glide ratio was reduced by 0.6% when introducing the gap.

8.3. Control with multiple flap actuators

This section demonstrates a controller setup for two independent span-wise distributed flaps, following the argumentation from section 6.3 about distributed actuators. For a low Reynolds number of Re $= 50,000$ the basic principle will be demonstrated to show the capability of the hybrid IB method.

8.3.1. Geometry and numerical setup

The mesh for the NACA0015 airfoil geometry of section 5.2 was extruded to a span of $0.5C$. The span-wise cells were distributed with a cosine function to cluster more cells in the middle region around $y = 0.25$. The cell count in span-wise direction was 32 to keep the mesh size as small as possible. This was esp. important since long time spans have to be simulated for controller applications and small time steps are needed because of the moving geometries. The trailing edge flap covered 10% of the chord. The mesh was not altered to account for the moving boundaries. Two separate span-wise flaps were used in this study. Each flap spanned $0.25C$; there was no gap between them. The angle of attack was varied according to case B from Fig. 8.5 ($\alpha = \phi$, see section 6.3.3).

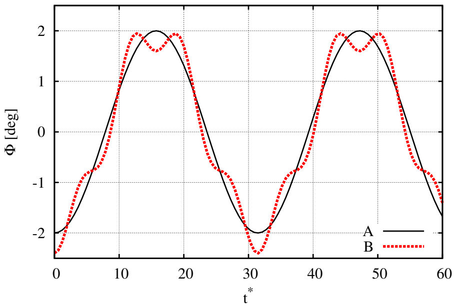

Figure 8.5.: *Pitch oscillations for cases A and B*

8.3.2. Controller

The lift based controller from section 6.2 was applied. Each of the two flaps was controlled by an independent version of the controller. For the first flap a value of $k_{C_l} = 20$ was applied, while for the second flap $k_{C_l 2} = 60$ was applied to map the lift to a flap deflection. The second flap was therefore more sensitive to deviations from zero lift. Two different maximum deflection speeds and maximum deflection angles were assigned to the flaps (Tab. 8.2). The controller parameters were not optimized for this setup.

Name	δ_{m1}	δ_{m2}	ω_{m1}	ω_{m2}
reference	0°	0°	0.00	0.00
independent	5°	2°	0.05	0.10

Table 8.2.: *Case setup*

8.3.3. Results

Fig. 8.6 compares the obtained time-varying lift for both the controlled case and an uncontrolled case with static flaps. A reduction in lift coefficient variance of 3.96% was achieved. Fig. 8.7 show the corresponding flap deflections. We see that the second flap showed an on/off behavior and moved fast between the two maximum deflections. The first flap was well adjusted to the range of C_l variations and reached its peak deflections for a lift coefficent of $C_l \approx 0.3$.

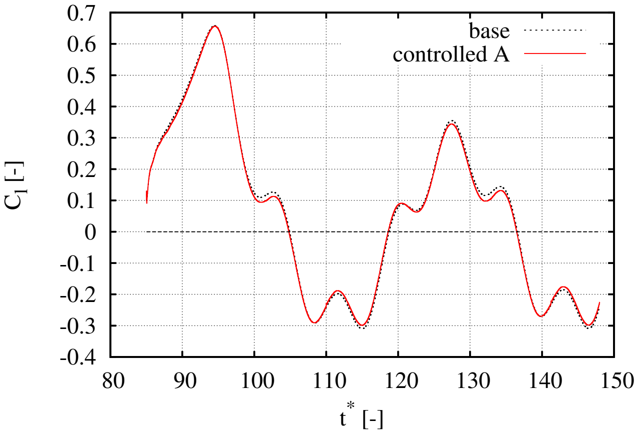

Figure 8.6.: *Lift coefficients C_l for reference and controlled run*

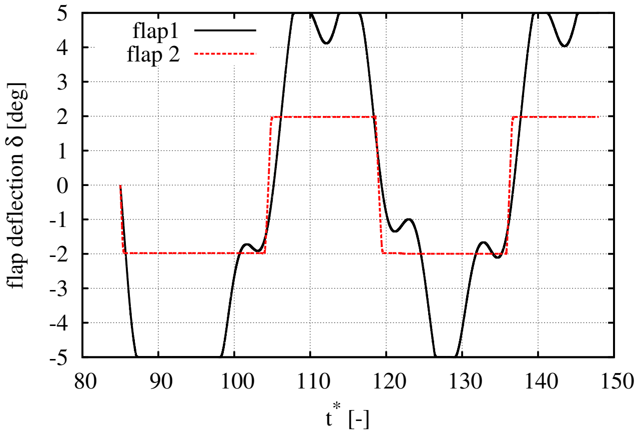

Figure 8.7.: *Flap deflections $\delta_{1/2}$ for controller run*

8.3.4. Conclusion

Even though the control parameters were not optimized for the presented setup, the flap deflections showed the expected behavior. The low achieved lift variance reduction was mainly the result of the short flap lengths and the low deflections. However, an estimated maximum lift change of $\Delta C_l = 0.072$ was derived from 2D XFOIL calculations for a plain flap at $\alpha = 2°$ and negative flap deflection, averaging between the cases for $\delta = -2$ and $\delta = -5$. The data presented earlier in Fig. 2.3

suggests higher flap efficiencies, but has been derived for high Reynolds numbers of $1.2 \cdot 10^6 \leq \mathrm{Re} \leq 16 \cdot 10^6$. The actually obtained maximum lift change $\Delta C_l \approx 0.017$ accounted for only one quarter of the XFOIL estimate. An early separation on the flap occurred, which was not predicted in XFOIL. Fig. 8.8 shows the recirculation areas on the two flaps for a static deflection of $\delta_1 = 2°$ and $\delta_2 = 5°$ at $\alpha = 0°$. More investigations are needed for such low Reynolds number cases. However, the next section will focus on the flow around a flap configuration at a high Reynolds number.

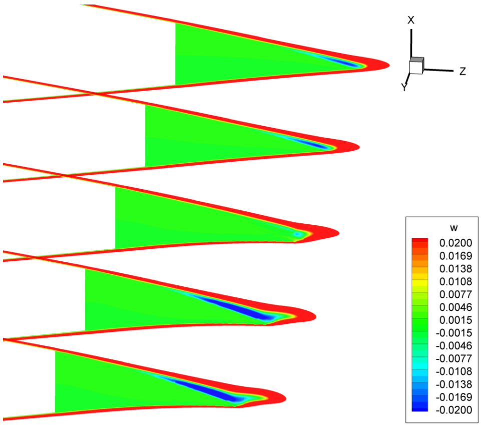

Figure 8.8.: *Slices of velocity component w*

8.4. Single deflected flap in 3D

As a final application of the hybrid immersed boundary, an investigation on a NACA0012 at $\mathrm{Re} = 1.63 \cdot 10^6$ with a 50% span-wise flap will be presented in this section. The focus will be on the effect of the deflected part on the flowfield and esp. the wake structure.

8.4.1. Geometry and numerical setup

The extruded three dimensional geometry of the NACA0012 from section 5.4 is used ($0.5C$ span), the total number of cells was $35 \cdot 64^3 = 9.175.040$. The distribution of grid points has been changed to accumulate more of them close to the middle of the domain (Fig. 8.9), where a $0.23C$ long and $0.25C$ wide flap is deflected by 5° (flap shape $\mathrm{sc} = 2$). The geometry is located between $z = -0.35$ (LE) and $z = 0.65$ (TE).
The angle of attack was fixed to $\alpha = 0°$ and the Reynolds number was $\mathrm{Re} = 1.63 \cdot 10^6$. The results present the flow state after 20 non-dimensional time-steps of an unsteady simulations with $\Delta t^* = 0.001$.

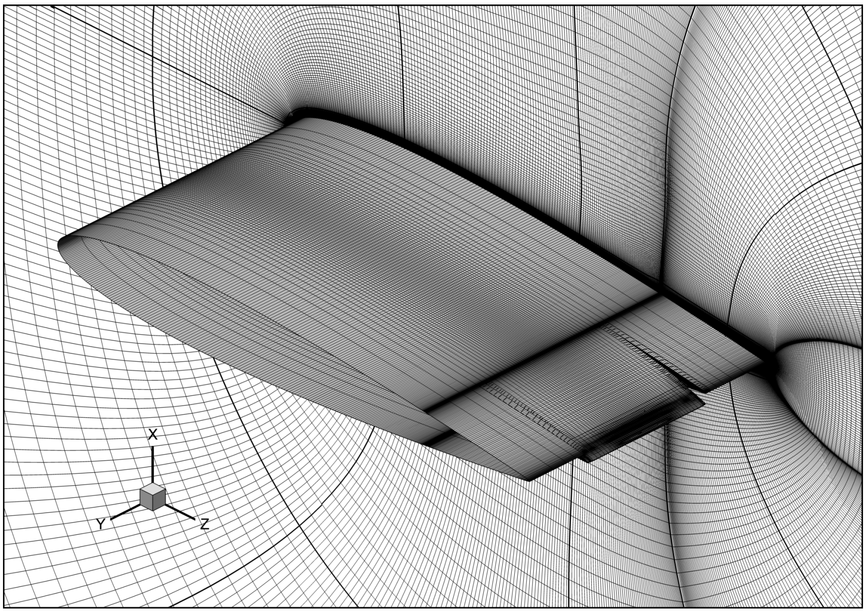

Figure 8.9.: *Overview of 3D geometry with deflected middle flap $\delta = 5°$, body representation by iso-surface of velocity magnitude $V_t = 0.01$*

8.4.2. Results

First, we can compare the lift generated by the deflected partial flap with that for a simulation where the flap was deflected along the full span (not shown). The 50% span flap resulted in a lift coefficient of $C_l = 0.124$, whereas the 100% span flap resulted in $C_l = 0.267$. Assuming that the lift coefficient would double when the spanwise flap lenght doubles we can compare the lift for the full flap $C_l = 0.267$ and an extrapolated lift of $C_l = 0.248$. The comparison yields a loss in C_l per flap-span of 3.48% for the partial flap.
Looking at the velocity magnitude at three different slices (Fig. 8.10), one sees that for the first slice at $y = 0.01$ close to the domain boundary, the velocity contours

close to the trailing edge are already slightly asymmetrical. Even though that the flap part of the airfoil is not deflected in this sectional cut.
The slice at $y = 0.125$ is exactly at the transition between the deflected and the undeflected flap part. The flow asymmetry becomes more pronounced and both flap shapes can be seen through their region of zero velocity magnitude.
Finally, the slice at $y = 0.25$ cuts through the deflected flap at mid-span. Here, the speed-up effect on the suction side can be seen most clearly.
When looking at the same slice positions but plotting the pressure (Fig. 8.11), we see that the pressure is influenced by the flap deflection along the whole span. Therefore, the flap generates a lift force along the whole span. The span-wise influence can be seen even clearer when looking at the isobars on the airfoil section (Fig. 8.12). The upstream influence of the flap is visible on both suction and pressure side. The isobars are non-uniform in span-wise direction up to $0.3C$ upstream of the flap. One can see directly, that the pressure distribution along the chord deviates from the symmetrical distribution one would expect for a symmetrical airfoil at zero incidence, when comparing the suction and the pressure side.
The flow over the airfoil section is influenced to a large degree by the trailing edge flap. Therefore, Fig. 8.13 takes a closer look at the flap region and presents slices at different z-positions . The slices show only values from the side walls to mid-span. The velocity component w is plotted to give an idea about the geometry and the wake. The two other components u and v are represented by a vector field[2] to show the tangential flow directions. The slice at $z = 0.6$ is cutting through the trailing edge geometry. It can be seen, that the vector field already shows an inwards movement on the suction side part and an outward movement on the pressure side with high gradients in the boundary layer. A vortex structure with a clear core region can already be seen $0.05C$ downstream in the slice at $z = 0.7$. Further down at $z = 0.8$ the structure is more homogeneous and has less steep gradients. Now, we like to obtain an overview of the forming vortex system. Fig. 8.14 shows the absolute vorticity in z-direction $|\Omega_z|$ with slices and iso-surfaces. The highest values can be found on the gap and immediately after the trailing edge. We see two vortex sheets that start to roll up quickly after the trailing edge. The $|\Omega_z|$ value in the vortex cores decreases fast, but the distinct vortex structures stay stable convecting downstream.
Out of curiosity, the total pressure p_t (reference pressure $p_r = 0$, $\rho = 1$) is plotted in Fig. 8.15 in different z-slices. Thereby, we can investigate the propagation of the wake loss downstream. The development of the wake structure from $z = 0.65$ directly after the trailing edge until $z = 4.00$ shows the forming of the vortex structure. The wakes of the deflected flap part and the undeflected parts are clearly separated in x-direction by the forming vortices.

8.4.3. Conclusion

The hybrid IB approach was able to handle the three dimensional flow around a partially deflected flap. The flap influenced the flow field along the full span. The deflection led to the formation of a distinct pair of trailing vortices. A loss in C_l per span of 3.48%, compared to the a full flap case, was observed.

---

[2] scaling 0.1 grid units / magnitude

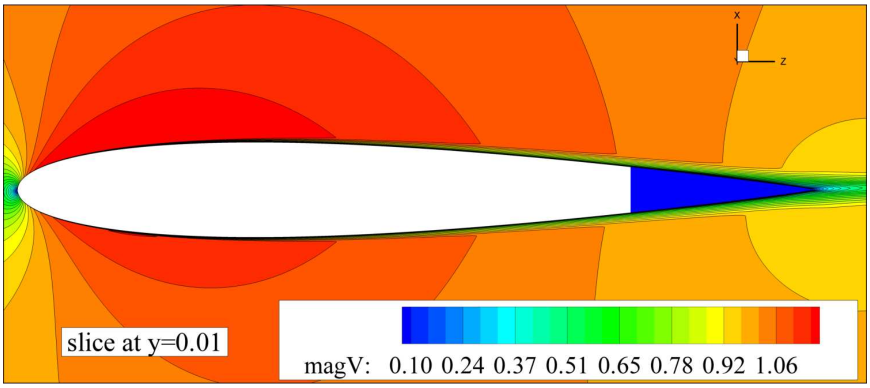

(a) $y = 0.01$

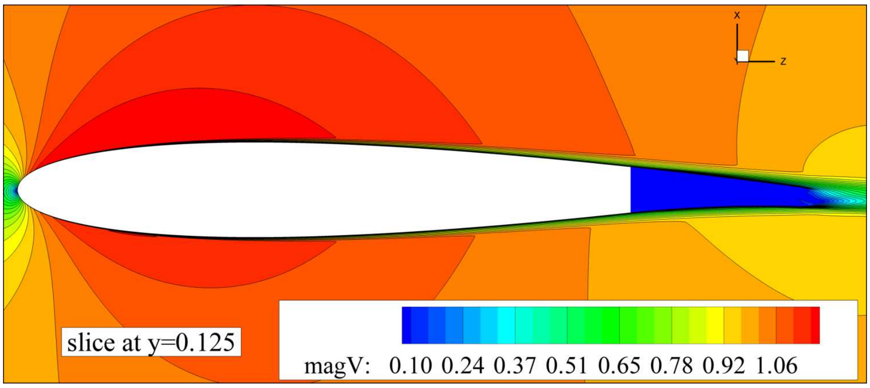

(b) $y = 0.125$

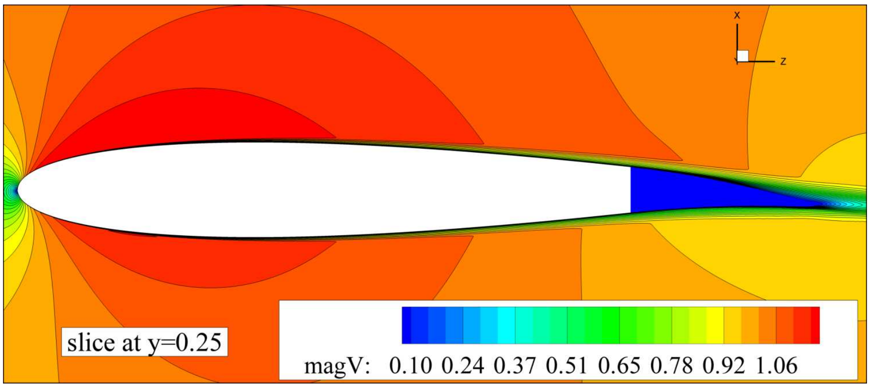

(c) $y = 0.25$

Figure 8.10.: *Slices of velocity component v*

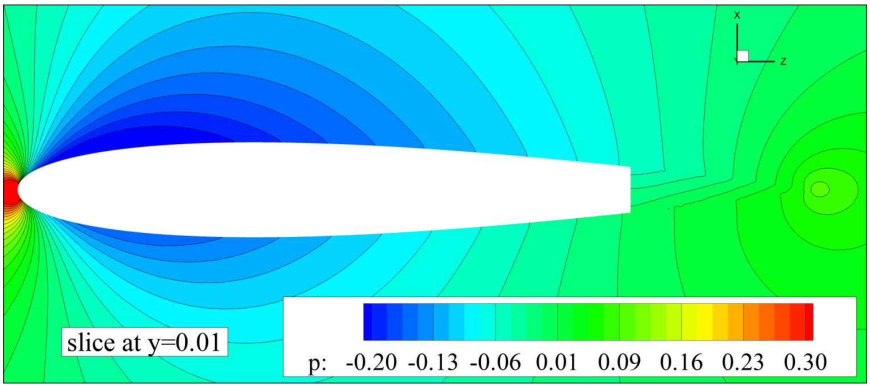

(a) $y = 0.01$

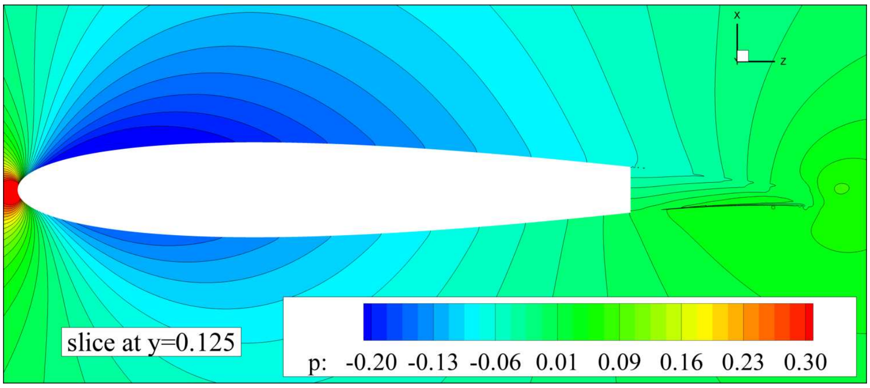

(b) $y = 0.125$

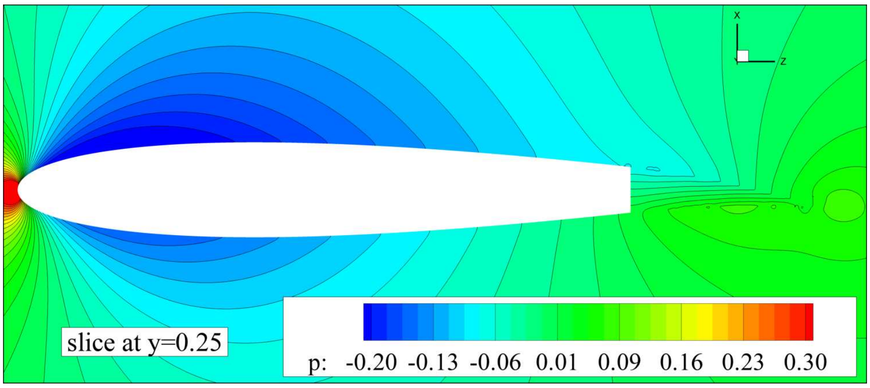

(c) $y = 0.25$

Figure 8.11.: *Slices of pressure p*

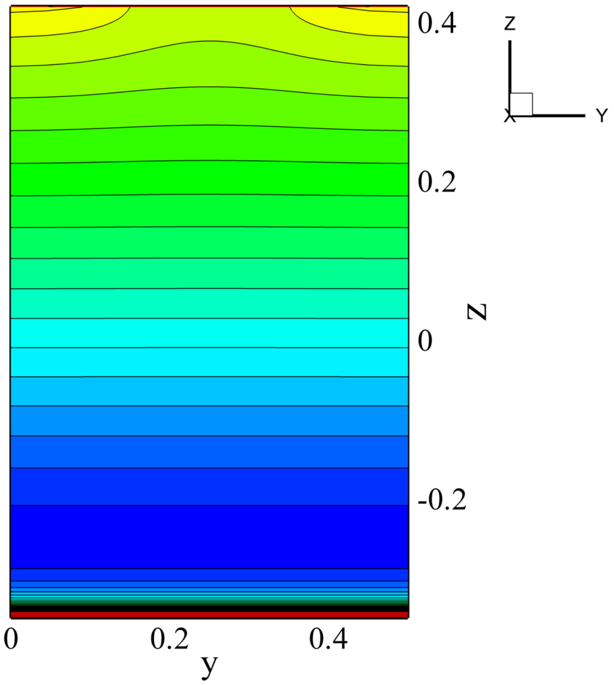

(a) suction side

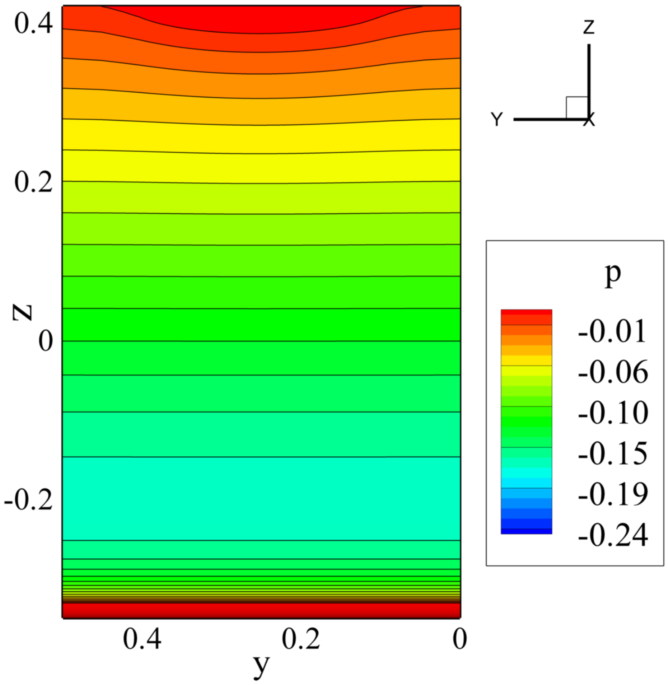

(b) pressure side

Figure 8.12.: *Surface pressures on body (only body fitted part shown here)*

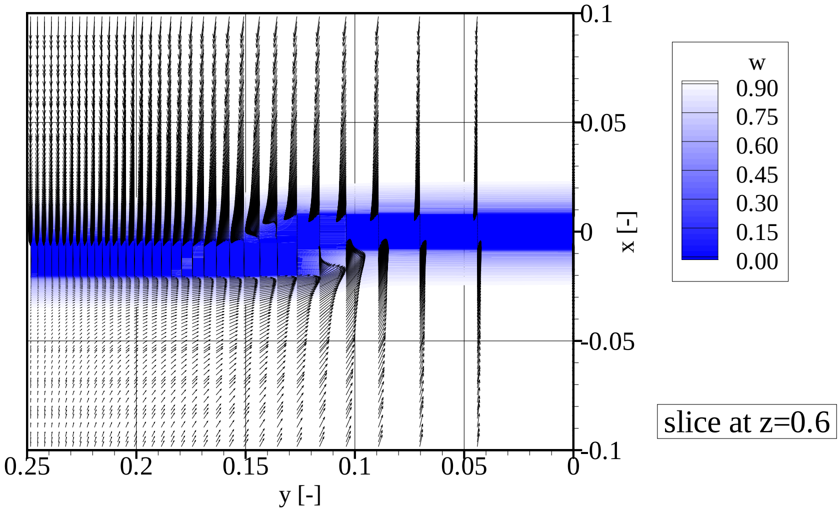

(a) $z = 0.6$

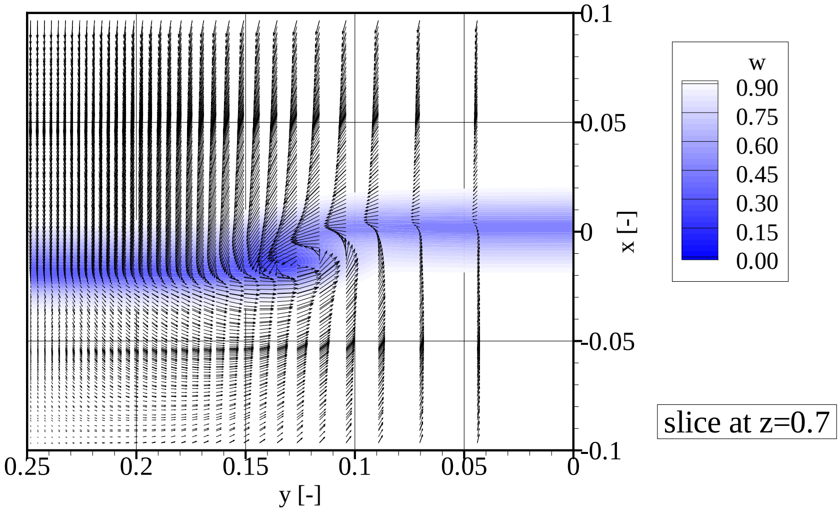

(b) $z = 0.7$

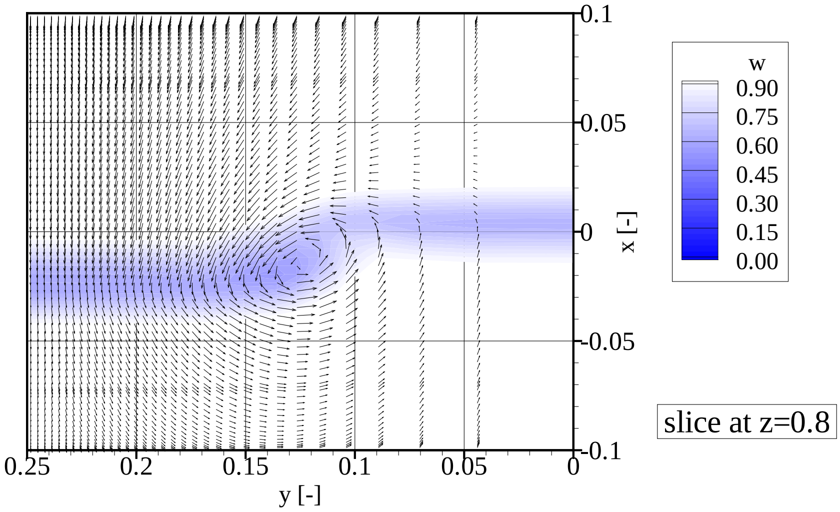

(c) $z = 0.8$

Figure 8.13.: *Slices showing the tangential vectors*

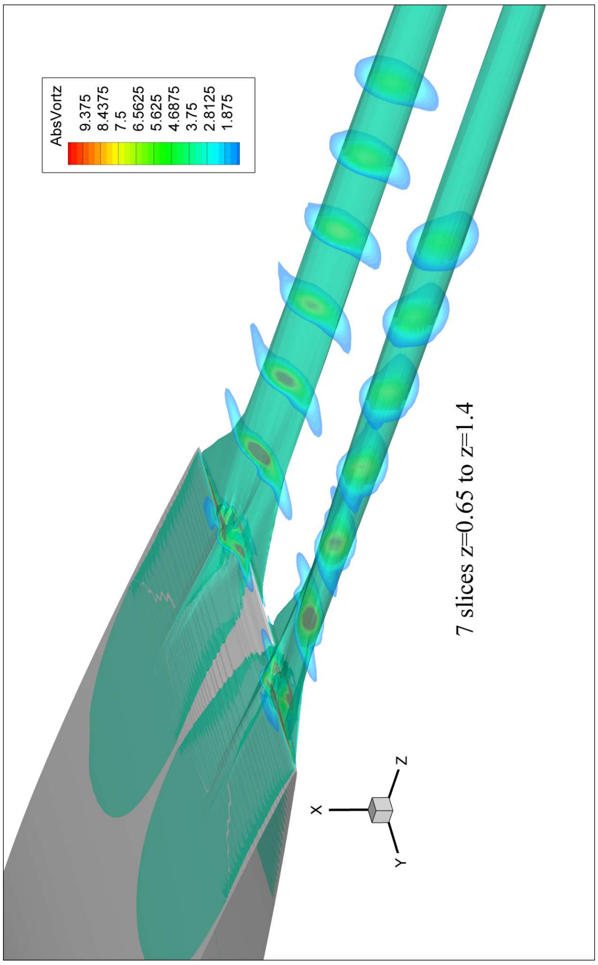

Figure 8.14.: *Slices and iso-surface of* Ω_z

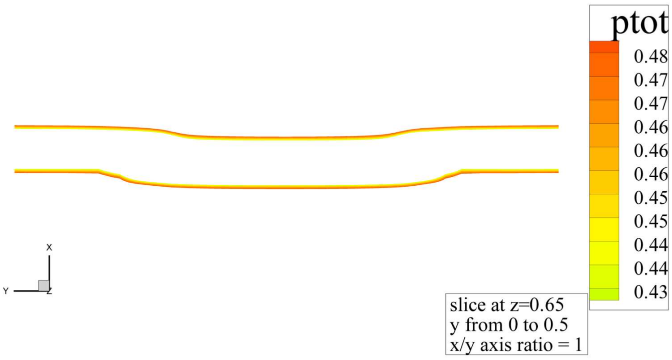

(a) $z = 0.65$

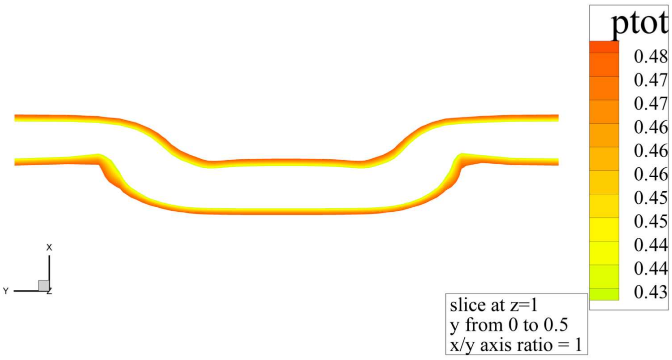

(b) $z = 1.00$

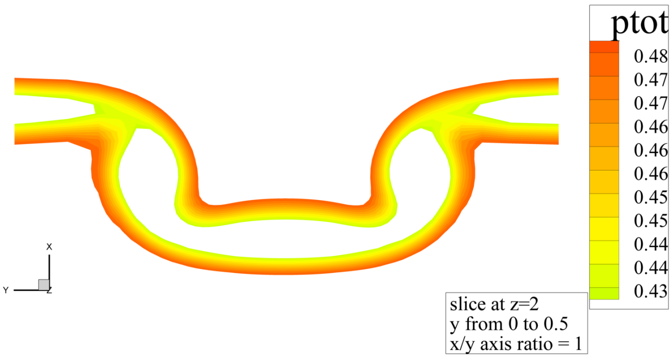

(c) $z = 2.00$

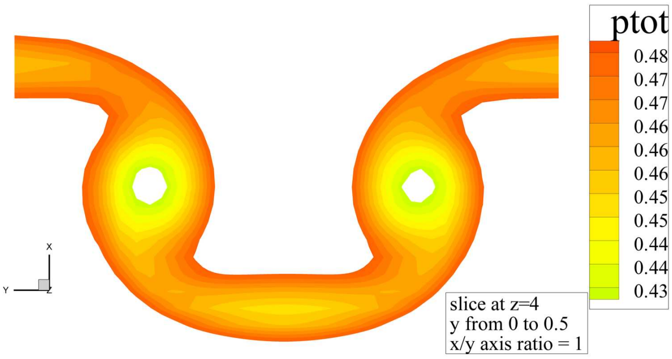

(d) $z = 4.00$

Figure 8.15.: *Wake - total pressure levels*

Part IV.

Conclusions and perspectives

9. Conclusions and perspectives

This final part will conclude the dissertation and offer some recommendations and perspectives for future work.

Introduction

The ever increasing rotor diameter of modern wind turbines calls for ways to considerably decrease the resulting loads on the structure. The so-called 'smart rotor' concept is perceived as a promising way to generate significant load reductions. The concept applies distributed aerodynamic control surfaces to the turbine blades, so that the blade lift can be swiftly adjusted to the unsteady inflow conditions.

The trailing edge flap control surface is of particular interest. Today, the unsteady flow around such devices is usually investigated by applying linearized unsteady aerodynamic models (based on e.g. thin airfoil assumptions) or by solving the two dimensional unsteady Reynolds averaged Navier-Stokes equations. The latter method is usually applied together with morphing or interpolated meshes to model the moving geometries. A more flexible method would open up an opportunity to investigate the flow features of complex moving flap geometries in great detail.

The immersed boundary method offers the needed high flexibility for moving and for complex geometries, as it represents the body boundaries by introducing additional forcing terms in the governing equations. The immersed boundary method allows for simulation of arbitrary geometries in fixed meshes that do not have to conform to the body geometry.

The aim of this research was to evaluate, prepare and demonstrate an immersed boundary method for application to trailing edge flaps.

Summary of results

The flow solver EllipSys has previously been extended with a base implementation of an immersed boundary method. The present work developed the necessary tools to handle trailing edge flap geometries in two and three dimensions. To begin with, validation cases were presented for a circular cylinder in a Cartesian mesh topology and in a topology similar to that of a standard body fitted mesh. The body adjusted mesh topology proved to be able to reduce the cell count considerably.

For application to trailing edge flaps, a hybrid approach was presented that only modeled the moving flap as an immersed boundary, whereas the rest of the airfoil was represented by a conventional body-fitted mesh. The approach was compared to wind tunnel measurements and improvement over thin-airfoil based flow models was proven.

A load alleviation control in a changing inflow was presented for a divided flap action. It has been demonstrated that the flap movement can be divided into two separate deflections without deteriorating control authority. The results suggested that the combined use of two independent flap actuators might be beneficial when dealing with complex inflows.

Full scale turbine measurements were presented and indicated that the flap hinge moment is a suitable input for load control. A novel way of using the hinge moment of a moving flap for load alleviation control was presented and simulations demonstrated the feasibility and the robustness of the approach.

This work presented three demonstrator cases, applying the hybrid approach to 3D geometries. The approach was able to handle 3D airfoil sections with span-wise flap gaps. A control for two span-wise independent flaps was implemented and first load reductions were achieved. The flow around and in the wake of a deflected flap at a Reynolds number of $1.63 \cdot 10^6$ was presented for steady inflow conditions.

The method has demonstrated to be a versatile tool for investigating moving trailing edge flaps. It could be demonstrated that improvements in prediction ability were possible when comparing with a thin airfoil code. The possibilities of the three dimensional method have been presented and they shall serve as the basis for future investigations of the unsteady flow field around trailing edge flaps.

Recommendations

In this last section of the dissertation, I will present some recommendations for improvements to the numerical methods and propose topics for further research.

Firstly, a clear line should be drawn between further development of the code and its application to concrete problems. Two topics are of utmost importance in terms of improving the implemented immersed boundary method, esp. in 3D.

The first topic is to reduce the restrictions inherent in the structured meshes by introducing a local grid refinement technique. Since this is not straightforward for structured meshes, maybe the approach presented in [24] can serve as inspiration. The presented local adaptive refinement of fully structured grids applies an *iblanking* technique to disable grid points of underlying high resolution meshes. It is stated that the approach does not lead to computational or memory penalties, since no additional variables are used in the coarse region and no equations have to be solved at the blanked locations. Using that method, the higher local resolution does not have to lead to an increased resolution in regions of small gradients. Such a method could possibly be integrated into EllipSys through the already present multi-grid capability. Further, the method could be limited to supply the finer mesh only in blocks containing the immersed boundary, without using the full algorithm for local refinement.

The second important topic is the investigation of wall models, as presented in [20, 21] among others, for immersed boundary methods in an LES environment. The wall models could allow for coarser mesh resolution in the vicinity of the immersed boundary. Adding wall models to the code should go hand in hand with revising the interpolation schemes.

Aside from the above improvements to the numerical methods, the handling of the geometries in three dimensions can also be improved. Geometries are treated as triangles inside the code. Therefore, a direct geometry input through e.g. STL[1] files would considerably increase the flexibility of the method and allow its application to a wider range of problems. Additionally, faster algorithms to calculate the normal distances[2] should be investigated to reduce the computing time both in 2D and 3D. A thorough comparison with overset and morphing mesh methods should help in identifying which method should be preferred for a given application and where the methods complement one another.

The applications presented in this work may only scratch the surface of what is possible. More comprehensive studies are needed to leverage on the work done so far. Esp. unsteady simulations with high quality grids and possibly large scale turbulence in three dimensions offer exciting opportunities, given that the computational resources are available.

The concept of using the flap as a sensor has proven its potential to become a viable option for traditional flow sensors. Enhanced prediction of the hinge moment,

---

[1] this file format provides the triangulated surface through its vertices and its unit normal vector

[2] e.g. the idea of interpolating/mapping the distances on the block boundaries and the immersed boundary

through additional stall modeling in the potential flow model (as e.g. in [8]) or implementing parameterized flap efficiency factors might further improve the results. A wind tunnel test could answer questions regarding the practical implications and the feasibility of the sensor integration. In addition, it would be interesting to derive the hinge moment contribution of the inertial forces resulting from the blade movement.

Investigating the aerodynamic influence of the flaps on each other, and applying a flap controller in large scale 3D turbulence could give a realistic impression of the hinge moments that a real life actuator would need to overcome on a spinning turbine in turbulent inflow.

An application of the hybrid IB approach together with noise predictions tools [87] would allow a possibility to investigate the influence of active trailing edge flaps on the airfoil noise, which might be a critical topic in the context of wind energy.

Obvious applications of the implemented hybrid method would be the investigation of movable micro-tabs and slats. Further, the method might allow for interesting applications within full rotor investigations when used to model the nacelle and tower geometries. For flow in complex terrain, immersed boundary methods have already seen applications [45, 35]. The combination of the IB method with large-eddy simulations of wind farm flows poses interesting challenges in the field of complex terrains flows.

Bibliography

[1] Procedure for Estimation and Reporting of Uncertainty Due to Discretization in CFD Applications. *Journal of Fluids Engineering*, 130(7):078001, 2008.

[2] *Proceedings of the Academy Colloquium Immersed Boundary Methods: Current Status and Future Research Directions. KNAW, Amsterdam (The Netherlands), 15-17 June 2009*, 2009.

[3] H. Aagaard Madsen et al. The potentials of the controllable rubber trailing edge flap (CRTEF). In *EWEC 2010 Proceedings online*, page 11, 2010.

[4] I. H. Abbott and A. E. von Doenhoff. *Theory of Wing Sections: Including a Summary of Airfoil Data*. Dover Publications, 1959.

[5] I. Abdallah. Advanced load alleviation for wind turbines using adaptive trailing edge geometry: Sensoring techniques. Master's thesis, Technical University of Denmark, 2006.

[6] I. Abdallah et al. Patent application 2009056136 (A2), WIND TURBINE BLADE AND METHOD FOR CONTROLLING THE LOAD ON A BLADE, May 2009.

[7] P. B. Andersen. *Advanced Load Alleviation for Wind Turbines using Adaptive Trailing Edge Flaps: Sensoring and Control*. PhD thesis, Risø-DTU - National Laboratory for Sustainalbe Energy, 2010.

[8] P. B. Andersen et al. A Dynamic Stall Model for Airfoils with Deformable Trailing Edges. *Journal of Physics: Conference Series*, 75(1):012028, 2007.

[9] P. B. Andersen et al. Deformable trailing edge flaps for modern megawatt wind turbine controllers using strain gauge sensors. *Wind Energy*, 13(2-3):193–206, 2010.

[10] P. Bæk et al. A comparison of two devices for distributed active load control of wind turbine blades. In *Proceedings of TORQUE 2010 The science of making torque from wind, June 28-30, 2010, Heraklion, Greece*, 2010.

[11] T. Barlas and G. van Kuik. Review of state of the art in smart rotor control research for wind turbines. *Progress in Aerospace Sciences*, 46(1):1 – 27, 2010.

[12] A. Bechmann et al. The Bolund Experiment: Overview and Background, Risø-R1658(EN). Technical report, Risø-DTU, National Laboratory for Sustainable Energy, 2009.

[13] T. Behrens, D. Castaignet, and C. H. Westergaard. Patent application WO 2010124914 (A2), WIND TURBINE BLADE, May 2010.

[14] T. Behrens et al. Patent application WO 2011057633 (A2), IMPROVED CONTROL OF WIND TURBINE BLADE LIFT REGULATING MEANS, May 2011.

[15] T. Behrens and W. J. Zhu. Feasibility of aerodynamic flap hinge moment measurements as input for load alleviation control. In *Scientific Proceedings of the European Wind Energy Conference & Exhibition, 14 - 17 March 2011, Brussels - Belgium*, pages 28–32, 2011.

[16] G. E. P. Box and M. E. Muller. A note on the generation of random normal deviates. *The Annals of Mathematical Statistics*, 29(2):pp. 610–611, 1958.

[17] P. Bradshaw, D. H. Ferriss, and N. P. Atwell. Calculation of boundary-layer development using the turbulent energy equation. *Journal of Fluid Mechanics*, 28(03):593–616, 1967.

[18] T. Buhl, M. Gaunaa, and C. Bak. Potential load reduction using airfoils with variable trailing edge geometry. *Journal of Solar Energy Engineering*, 127(4):503–516, 2005.

[19] D. Castaignet et al. Results from the first full scale wind turbine equipped with trailing edge flaps. In *28th AIAA Applied Aerodynamics Conference, 28 June - 1 July 2010, Chicago, Illinois*, 2010.

[20] J.-I. Choi, R. C. Oberoi, J. R. Edwards, and J. A. Rosati. An immersed boundary method for complex incompressible flows. *Journal of Computational Physics*, 224(2):757 – 784, 2007.

[21] A. Cristallo and R. Verzicco. Combined immersed boundary/large-eddy-simulations of incompressible three dimensional complex flows. *Flow, Turbulence and Combustion*, 77:3–26, 2006. 10.1007/s10494-006-9034-6.

[22] S. Dennis and G.-Z. Chang. Numerical solutions for steady flow past a circular cylinder at Reynolds numbers up to 100. *J. Fluid Mech.*, 42(3):471–489, 1970.

[23] M. T. Dröge. *Cartesian grid methods for turbulent flow simulation in complex geometries*. PhD thesis, Rijksuniversiteit Groningen, 2007.

[24] P. A. Durbin and G. Iaccarino. An approach to local refinement of structured grids. *Journal of Computational Physics*, 181(2):639 – 653, 2002.

[25] D. Eberly. Distance between point and triangle in 3D, http://www.geometrictools.com/Documentation/DistancePoint3Triangle3.pdf, March 2008.

[26] S. Eisenbach and R. Friedrich. Large-eddy simulation of flow separation on an airfoil at a high angle of attack and Re=10000 using Cartesian grids. *Theoretical and Computational Fluid Dynamics*, 22(3):213–225, May 2008.

[27] M. Frederick, E. Kerrigan, and J. Graham. Gust alleviation using rapidly deployed trailing-edge flaps. *Journal of Wind Engineering and Industrial Aerodynamics*, 98(12):712 – 723, 2010.

[28] P. P. Friedmann, G. P. Carman, and T. A. Millott. Magnetostrictively actuated control flaps for vibration reduction in helicopter rotors–design considerations for implementation. *Mathematical and Computer Modelling*, 33(10-11):1203 – 1217, 2001.

[29] M. Gaunaa. Unsteady 2d potential-flow forces on a thin variable geometry airfoil undergoing arbitrary motion. Technical Report Risø-R-147, Risø, 2005.

[30] M. Gaunaa and P. B. Andersen. Load reduction using pressure difference on airfoil for control of trailing edge flaps. In *2009 European Wind Energy Conference and Exhibition, 2009, Marseille (FR), 16-19 Mar*, 2009.

[31] L. Ge and F. Sotiropoulos. A numerical method for solving the 3d unsteady incompressible navier-stokes equations in curvilinear domains with complex immersed boundaries. *Journal of Computational Physics*, 225(2):1782 – 1809, 2007.

[32] N. Hariharan. Unsteady aerodynamics of a flapped airfoil in subsonic flow using indicial concepts. Master's thesis, Dept. of Aerospace Engineering, University of Maryland, 1995.

[33] M. Harris, M. Hand, and A. Wright. Lidar for turbine control. Technical report, NREL National Renewable Energy Laboratory, 2005.

[34] J. C. Heinz. Investigation of piezoelectric flaps for load alleviation using cfd. Master's thesis, Wind Energy Department, Risø National Laboratory for Sustainable Energy, Technical University of Denmark DTU, 2008.

[35] S. Jafari, N. Chokani, and R. S. Abhari. An immersed boundary method for efficient simulation of wind flow over complex terrain. In *Scientific Proceedings of the European Wind Energy Conference & Exhibition, 14 - 17 March 2011, Brussels - Belgium*, pages 28–32, 2011.

[36] S. J. Johnson, C. van Dam, and D. E. Berg. Active load control techniques for wind turbines. Technical Report SAND2008-4809, Sandia National Laboratories, 2008.

[37] G. Kalitzin and G. Iaccarino. Turbulence modeling in an immersed-boundary rans method. Annual research briefs, Center for Turbulence Research, Annual Research Briefs, 2002.

[38] G. Kalitzin and G. Iaccarino. Toward immersed boundary simulation of high reynolds number flows. Annual research briefs, Center for Turbulence Research, Annual Research Briefs, 2003.

[39] C. S. Kothera and N. M. Wereley. *Wind Tunnels*, chapter Wind Tunnel Testing of Pneumatic Artificial Muscles for Control Surface Actuation. InTech, 2011.

[40] A. Krzysiak and J. Narkiewicz. Aerodynamic loads on airfoil with trailing-edge flap pitching with different frequencies. *Journal of Aircraft*, 43(2):407–418, March-April 2006.

[41] M.-C. Lai and C. S. Peskin. An immersed boundary method with formal second-order accuracy and reduced numerical viscosity. *Journal of Computational Physics*, 160(2):705 – 719, 2000.

[42] T. J. Larsen, H. A. Madsen, and K. Thomsen. Active load reduction using individual pitch, based on local blade flow measurements. *Wind Energy*, 8(1):67–80, 2005.

[43] B. Launder and B. Sharma. Application of the energy-dissipation model of turbulence to the calculation of flow near a spinning disc. *Letters in Heat and Mass Transfer*, 1(2):131–137, 1974.

[44] J. G. Leishman. Challenges in modelling the unsteady aerodynamics of wind turbines. *Wind Energy*, 5:85–132, 2002.

[45] K. A. Lundquist, F. K. Chow, and J. K. Lundquist. An Immersed Boundary Method for the Weather Research and Forecasting Model. *Monthly Weather Review*, 138(3):796–817, 2010.

[46] H. A. Madsen et al. The DAN-AERO MW Experiments. Final Report. Technical Report Risø-R-1726(EN), Risø-DTU, National Laboratory for Sustainable Energy, September 2010.

[47] J. Mann. The spatial structure of neutral atmospheric surface-layer turbulence. *Journal of Fluid Mechanics*, 273:141–168, 1994.

[48] J. Mann. Wind field simulation. *Probabilistic Engineering Mechanics*, 13(4):269 – 282, 1998.

[49] G. Marsaglia. Normal (gaussian) random variable for supercomputers. *J. Supercomput.*, 5:49–55, June 1991.

[50] C. Meneveau, T. S. Lund, and W. H. Cabot. A lagrangian dynamic subgrid-scale model of turbulence. *Journal of Fluid Mechanics*, 319:353–385, 1996.

[51] F. Menter. Two-equation eddy-viscosity turbulence models for engineering applications. *AIAA J*, 32(8):1598–1605, 1994.

[52] M. Meyer et al. A conservative immersed interface method for Large-Eddy Simulation of incompressible flows. *Journal of Computational Physics*, 229(18):6300 – 6317, 2010.

[53] M. Méheut, O. Atinault, and J.-L. Hantrais-Gervois. elsA and TAU Assessment for Wing Control Surfaces. Technical Report TP 2011-102, ONERA, 2011.

[54] J. Michelsen. Basis3D - A Platform for Development of Multiblock PDE Solvers. Technical Report AFM 92-05, Technical University of Denmark, 1992.

[55] J. Michelsen. Block Structured Multigrid Solution of 2D and 3D Elliptic PDEs. Technical Report AFM 94-06, Technical University of Denmark, 1994.

[56] T. Mikkelsen et al. Lidar wind speed measurements from a rotating spinner. In *Scientific Proceedings of the European Wind Energy Conference & Exhibition, 20 - 23 April 2010, Warsaw, Poland*, 2010.

[57] R. Mittal and G. Iaccarino. Immersed boundary methods. *Annu. Rev. Fluid Mech.*, 37(1):239–, Jan. 2005.

[58] C. Peskin. Flow patterns around heart valves: A numerical method. *Journal of Computational Physics*, 10(2):252–271, October 1972.

[59] M. Reck. *Computational fluid dynamics, with detached eddy simulation and the immersed boundary technique, applied to oscillating airfoils and vortex generators*. PhD thesis, Technical University of Denmark, 2005.

[60] P. J. Roache. Quantification of uncertainty in computational fluid dynamics. *Annual Review of Fluid Mechanics*, 29(1):123–160, 1997.

[61] J. P. Rodgers and N. W. Hagood. Preliminary mach-scale hover testing of an integral twist-actuated rotor blade. volume 3329, pages 291–308. SPIE, 1998.

[62] F. Roman, E. Napoli, B. Milici, and V. Armenio. An improved immersed boundary method for curvilinear grids. *Computers & Fluids*, 38(8):1510–1527, Sept. 2009.

[63] H. Shan et al. Numerical study of passive and active flow separation control over a naca0012 airfoil. *Computers & Fluids*, 37(8):975–992, Sept. 2008.

[64] W. Z. Shen et al. An Improved SIMPLEC Method for Steady and Unsteady Flow Computations. *Numerical Heat Transfer*, 32(3), 2003.

[65] W. Z. Shen, J. A. Michelsen, and J. N. Sørensen. Improved Rhie-Chow Interpolation for Unsteady Flow Computations. *AIAA Journal*, 39:2406–2409, Dec. 2001.

[66] W. Skamarock et al. A Description of the Advanced Research WRF Version 2. NCAR Technical Note NCAR/TN-468+STR, NCAR, 2005.

[67] J. Smagorinsky. General circulation experiments with the primitive equations. *Monthly Weather Review*, 91(3):99–164, 1963.

[68] J. S. Son and T. J. Hanratty. Numerical solution for the flow around a cylinder at Reynolds numbers of 40, 200 and 500. *Journal of Fluid Mechanics*, 35(02):369–386, 1969.

[69] N. N. Sørensen. *General Purpose Flow Solver Applied to Flow over Hills*. PhD thesis, Risø National Laboratory, 1995.

[70] N. N. Sørensen. k-omega Turbulence Models Implementation and Testing. Technical Report Risø Report R-864, Risø National Laboratory, 1995.

[71] P. R. Spalart and S. R. Allmaras. A one-equation turbulence model for aerodynamic flows. *La Recherche Aerospatiale*, 1(1):5–21, 1994.

[72] D. Sucker and H. Brauer. Fluiddynamik bei quer angeströmten Zylindern. *Wärme- und Stoffübertragung*, 8(3):149–158, Sept. 1975.

[73] R. Szasz and L. Fuchs. Computations of the flow around a wind turbine: Grid sensitivity study and the influence of inlet conditions. In M. Deville, T.-H. Lê, and P. Sagaut, editors, *Turbulence and Interactions*, volume 110 of *Notes on Numerical Fluid Mechanics and Multidisciplinary Design*, pages 345–352. Springer Berlin / Heidelberg, 2010.

[74] F. Tessicini et al. Wall modeling for large eddy simulation using an immersed boundary method. *CTR Center for Turbulence Research, Annual research briefs*, 2002.

[75] T. Theodorsen. General theory of aerodynamic instability and the mechanism of flutter. Technical Report 496, NACA, 1935.

[76] N. Troldborg. Computational Study of the Risø-B1-18 Airfoil Equipped with Actively Controlled Trailing Edge Flaps. Master's thesis, Technical University of Denmark, Fluid Mechanics Section, 2004.

[77] N. Troldborg, J. N. Sørensen, and R. Mikkelsen. Actuator Line Simulation of Wake of Wind Turbine Operating in Turbulent Inflow. *Journal of Physics: Conference Series*, 75(1):012063, 2007.

[78] C. van Dam, T. Yen, and P. M. H. W. Vijgen. Gurney flap experiments on airfoil and wings. *J. Aircraft*, 36(2):484–486, 1999. Anglais.

[79] C. P. van Dam et al. Computational investigations of small deploying tabs and flaps for aerodynamic load control. *Journal of Physics: Conference Series*, 75(1):012027, 2007.

[80] J. W. van Wingerden et al. On the proof of concept of a 'Smart' wind turbine rotor blade for load alleviation. *Wind Energ.*, 11(3):265–280, 2008.

[81] J.-W. van Wingerden et al. Two-Degree-of-Freedom Active Vibration Control of a Prototyped Smart Rotor. *Control Systems Technology, IEEE Transactions on*, PP(99):1 –13, 2010.

[82] H. Wagner. Über die Entstehung des dynamischen Auftriebes von Tragflügeln. *Zeitschrift für angewandte Mathematik und Mechanik*, 1925.

[83] F. White. *Viscous fluid flow*. McGraw-Hill, 3 edition, 1991.

[84] D. C. Wilcox and R. J. Becker. Turbulence Modeling for CFD. *Applied mechanics reviews*, 47(11):–, 1994.

[85] J. Yang and E. Balaras. An embedded-boundary formulation for large-eddy simulation of turbulent flows interacting with moving boundaries. *Journal of Computational Physics*, 215(1):12 – 40, 2006.

[86] J. Zayas. Active aerodynamic load control for wind turbine blades. In *EWEC2006, Athens, Greece*, 2006.

[87] W. J. Zhu. *Aero-Acoustic Computations of Wind Turbines*. PhD thesis, Technical University of Denmark, Department of Mechnical Engineering, 2007.

List of Figures

List of Tables